Nanoscale Self-Assembly: Energetic Irradiation Triggering and In Situ Monitoring

A THESIS SUBMITTED TO THE FACULTY OF THE UNIVERSITY OF MINNESOTA

BY

Chunhui Dai

IN PARTIAL FULFILLMENT OF THE REQUIREMENTS FOR THE DEGREE OF DOCTOR OF PHILOSOPHY

Advisor: Prof. Jeong-Hyun Cho

April 2020

Copyright

Acknowledgement

My sincere gratitude goes to my advisor Prof. Jeong-Hyun Cho for supporting my PhD study and research. He is always passionate, kind, patient and willing to help. Without his guidance, support, and encouragement, I can not go through all the difficulties during my PhD and continue to chase for my goal. I always feel honored and fortunate to be a member of his group and have the chance to work with him.

I would also like to acknowledge my committee members: Prof. Bethanie Stadler, Prof. Joey Talghader, Prof. Michael McAlpine for their encouragement and insightful suggestions.

I am grateful to all the collaborators, Prof. Tony Low, Prof. Kalpna Gupta, Prof. Steven Koester, Prof. Daeha Joung, Prof. Lianbi Li, Dr. Chao Liu, Dr. Andrei Nemilentsau, Dr. Jing Li, Kriti Argarwal, Qun Su, Daniel Wratkowski, Seokhyeong Lee, for their help and support through my PhD research. Without their help, I am not able to finish all the projects for this thesis.

I also appreciate the opportunity to meet and work with all the previous and current members in Prof. Joeng-Hyun Cho's group: Prof. Daeha Joung, Prof. Lianbi Li, Dr. Chao Liu, Kriti Agarwal, Jiaxuan Wen, Daniel Wratkowski, Emily Zhou, Nick Buchele, Joseph Schauff, Saran Kumar Chaganti, Neel Chatterjee, Seokhyeong Lee, Seung Yeon Lee, Yijia Liu, and Zihao Lin.

Finally, I would like to express my love and thank to my wife, Yuwei Wang, and my parents, Zhiyuan Dai and Yuemei Li, for their continuous support and encouragement.

Dedication

To my parents,

for their trust, support, and encouragement in whatever I am doing.

To my wife ,

for her endless love and faith through the darkness

Abstract

Origami inspired assembly of three-dimensional (3D) micro and nano-structures arise to be a broad topic in the past two decades due to their ability of property engineering, 3D space utilization, and controlled motion, which have been widely used in the applications of metamaterial and plasmonic devices, electronics, and biomedical devices. However, the present techniques for the assembly of 3D nanostructures, such as by using DNA technology, reactive ion etching, atomic layer deposition, and metal-assisted etching, do not allow real-time visualization, which bring great challenges in controlling the shape with nanoscale precision, resulting in an extremely low yield and significant geometric and topological constrains.

To address the issues of the traditional nanoscale self-assembly, my Ph.D. work involves developing novel *in situ* monitored self-assembly techniques triggered by energetic irradiation, such as ion and electron beam. The energetic irradiations offer two functions in the self-assembly: 1) on one hand, an excited ion or electron beam is able to deliver energy to the specific irradiated material, triggering localized material phase change, such as Sn grain coalescence, crystallization of amorphous material, or polymer reflow and shrinkage. Associated with the material phase changes, stress is induced in the thin film, folding the suspended 2D thin film up to 3D nanostructures; 2) on the other hand, the imaging capability of ion or electron beam enables real-time monitoring of the self-assembly process, making it possible to precise tune the energy delivery to reach the desired assembly status. Because of the localized energy delivery and real-time imaging,

ultra-high self-assembly process with sub-10 nm scale precision is achieved. With further understanding of the material-irradiation interaction and careful design of the 2D patterns and material layout, more advanced functions have been achieved, leading to programmable, sequential, multidirectional, and reversible self-assembly in nanoscale.

Further, the energetic irradiation triggered self-assembly processes have been used to build functional materials with advanced properties. I develop a strategy to build 3D graphene based nanostructures (*i.e.* nanocube and nanotube) *via* self-assembly process, which is one of the pioneer works in this field. By transforming graphene into 3D format, its amazing properties could be modified by the extra dimensionality, achieving enhanced or novel behaviors that does not exist in 2D. For instance, the plasmonic near-field enhancement of planar graphene undergoes severe exponential decay in the vertical direction away from the surface of the graphene, resulting in a relatively small spatial overlap between the specimens and the volume of high field confinement. I find that 3D graphene nanostructures exhibit novel plasmon hybridizations, which result in a near-field enhancement across the entire surface of these 3D structures as well as within their spatial volume. As the sensitivity is directly related to the field intensity in the vicinity of the analyte, the strong volumetric electric field confinement in these 3D nanostructures are proposed to be candidates for high sensitivity detection of proteins and other biological specimens. In addition, self-assembled nanocylinders with automatically formed plasmonic nanogaps have been developed into a nanofluidic based plasmonic sensor. The sequential and reversible self-assembly processes enable the realization of nano-machine and nano-robotics. Overall, this in situ monitored self-assembly technique provides a solid

foundation to build 3D nanostructures with various advanced functions, which push the limit for further exploration of the next generation devices.

Table of Contents

List of Figures

Figure 6.6. Schematics, and simulation results of the field enhancement in the graphene-based 2D ribbon, half-way curved cylinder, 1% gap cylinder, and completely curved nanocylinder at the frequencies of their geometric resonance. (a-d) 3D and cross-sectional schematics illustrating the coupling directions in 2D ribbons and 3D partially and completely curved cylinders. (e-h) The near-field enhancement plotted on the surface of a a) 2D ribbon, b, c) partially curved cylinders, and d) completely curved cylinders. i-l) The cross-section images show the field enhancement in the ZX plane when an imaginary cut plane is placed at the edge of the structures at 6000 nm. m) The field enhancement in ZX plane along the circumference at the ends of the structures (see the black arrow in e-h)). n) The field enhancements at the center of the gap in the halfway and 1% gap curved cylinders, at the surface of the completely curved cylinder along an imaginary edge, and on the surface of the ribbon. The corresponding values of field enhancement are plotted for the entire length of the structure along structural edges overlapping with cut plane as shown by the black arrow in Supporting Information Figure S5e-h. A strong propagating mode is seen along the edge of the cylindrical structure with 1% gap. o) The volumetric field enhancements along the length of the 3D structures are analyzed based on their ratio to the volumetric field in a 2D graphene ribbon. Volumetric enhancement is calculated by volume integrals of the field inside the 3D structures and for an imaginary rectangular box of thickness 119 nm placed on the 2D ribbon with lengths increasing from 100 nm to 6 μm. For all the cases m-o), the 3D cylindrical structures show stronger field enhancement compared to the 2D ribbon. The primary geometric resonant frequencies for the ribbon,

List of Abbreviations

2D: two-dimensional

3D: three-dimensional

RIE: reactive ion etching

FIB: focused ion beam

SEM: scanning electron microscope

TEM: transmission electron microscope

EDS: energy dispersive spectroscopy

AFM: atomic force microscope

DNA: deoxyribonucleic acid

PMMA: polymethyl methacrylate

Si: silicon

Ni: nickel

Al_2O_3: aluminum oxide

Au: gold

Sn: tin

Pt: platinum

W: tungsten

CF_4: tetrafluoromethane

O_2: oxygen

Ga: gallium

Cr: chromium

Hb: hemoglobin

IR: infrared

SRR: split-ring resonator

SERS: surface enhanced Raman spectroscopy

SCD: sickle cell disease

CVD: chemical vapor deposition

CO_2: carbon dioxide

CH_4: methane

Chapter1

Overview of Nanoscale Origami Like Self-Assembly

In this chapter, I introduce the origin, concept, and development of nanoscale origami like self-assembly process. I present the current self-assembly techniques based on reactive ion etching, meta-assisted chemical etching, thin film strain, and DNA technology. Some of the major applications in surface modification, advanced optical devices, and nanomachines are discussed. In addition, I address the limitation of current techniques and propose the strategy to use in situ monitored self-assembly for further improving the controllability and yield.

1.1 Evolution of Origami

Origami, referring to "paper folding", is an ancient oriental art, which can transform a piece of flat paper into fancy sculptures through several basic folds, such as valley and mountain folds, pleats, reverse folds, squash folds, and sinks [1]. The artists can use their bare hands and papers to create a wide variety of models including crane, fish, bird, frog, etc. [1, 2]. Only in some extreme cases, a paper clip or tweezer will be used to assist folding. Because of the limited usage of tools, the design plays an important role in origami works. In 1900s, the innovation of Yoshizawa-Randlett diagraming system provided an efficient method for designing and recording origami artworks, which triggers the renaissance of this ancient art [3]. The diagram for a lover's knot is shown in Figure 1. Later in the 1980s, a group of origami masters started to use mathematical methods to systematically

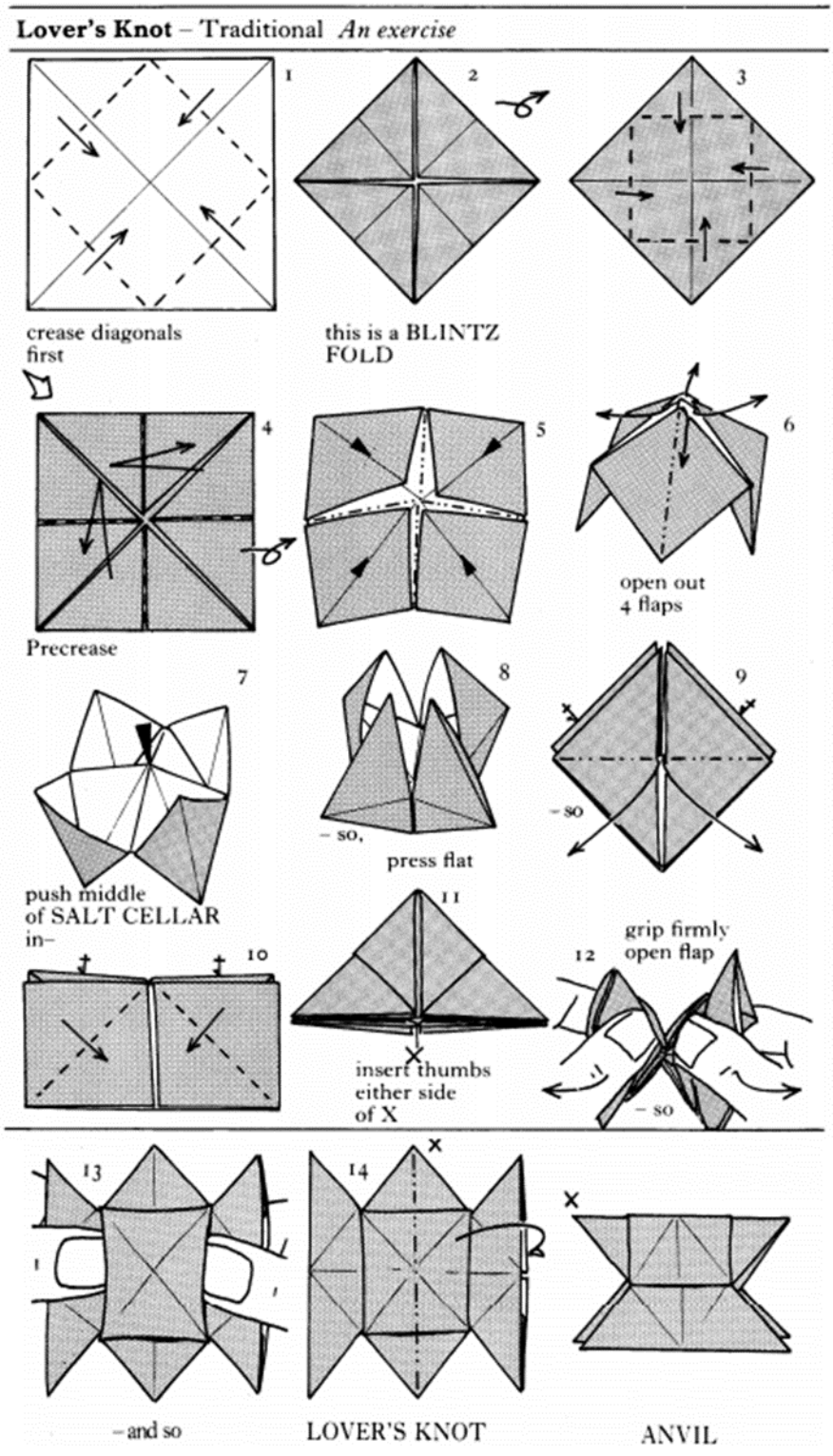

Figure 1.1 Yoshizawa-Randlett diagraming system of a Lover's Knot [4]

investigate the design of origami, leading to a rapid increases in the complexity of the origami models [5]. Because of these innovations, the content of origami has been significantly enriched, branching into a variety of new origami forms, such as action origami, modular origami, wet-folding, pureland origami, kirigami, and strip folding.

In the same time period of origami renaissance, the material science and engineering also steps into a rapid development era. Remarkable achievements have been achieved in material synthesis, device fabrication, and characterization, which vastly extend the boarder of material science. Especially, the inspiring lecture "There is plenty of room at the bottom, an invitation to enter a new field of physics" given by Nobel Prize Laureate Richard Feynman [6] encouraged the scientists and researchers to discover new phenomenon in the micro and nano world. Plenty of advanced discoveries are found in this new dimension, where it has quantum effects [7], higher surface to volume ratio [8], and Brownian motion [9]. In this dimension, the size and structure play critical roles in determining the material and further device properties. For instance, the nanostructured surface [10, 11, 12], nanogap [13, 14, 15, 16], or nanoparticle [17,18, 19] can demonstrate plasmonic properties, leading to higher energy conversion [17], better sensing [10, 12, 16, 18, 19], and even new characterization instrument [20]. Therefore, lots of effort has been put into pushing the development of synthesis or fabrication of well-controlled nanostructured materials.

With enormous demand of new fabrication techniques to better control the material structures, it is not surprising that the scientists have great interests in origami process, which can build complex architectures from simple two dimensional thin films. This magic

origami like self-assembly process perfectly matches the scope of micro and nanofabrication. Therefore, vast amount of effort has been put into adapting strategies of origami to material synthesis and fabrication. The first round innovation arose in the millimeter scale and microscale assembly [21]. Among these methods, various driving forces are used to trigger the origami like self-assembly, such as pneumatic force [22-24], magnetic force [25-28], volumetric expansion [29-32], differential thermal expansion [33-35], surface tension [20, 36,37], shape memory [38-40], thin film stress [41-43], shrinkage [44], and cell traction [45-47]. With further development of nanoscience and nanotechnology, it is possible to bring this magic origami process down to nanoscale. Several attempts have already been demonstrated, which will be briefly summarized in the following section.

1.2 Summary of Current Nanoscale Origami Like Self-Assembly Techniques

Though nanotechnology has been used for centuries, its name, “nanotechnology”, is not formally confirmed till 1974 by Japanese scientists Norio Taniguchi [48]. Since the field is defined, many breakthroughs happen in last few decades, which significant push the limits of nanotechnology, achieving better understanding and control of material in nanoscale. For instance, the invention of scanning tunneling microscopy by IBM Zurich scientist in 1983 [49] and later the AFM and TEM equipped scientist with the capability to see the materials in atomic level, which accelerate the advances in all aspects of nanotechnology. With the rapid development of nanotechnology, more and more advanced

instruments are available, making it possible to further scale the origami process down to nanoscale. Some of the widely used process are: reactive ion etching-based self-assembly [50-54], metal assisted chemical etching-based self-assembly [55], thin film stress-based self-assembly [56-61], and DNA-based self-assembly [62-67],

1.2.1 Reactive Ion Etching-based Self-Assembly

Plasma etching of Si in a RIE system is an exothermic process, which can generate sufficient energy to melt the low melting point materials such as Sn and further trigger grain coalescence (Figure 1.2) [50-54]. As a result of grain coalescence, surface tension force can be induced into the Sn thin film. When this thin film is deposited on a supporting frame, the surface tension force can curve or rotate the underlying panels out of plane, forming 3D nanostructures.

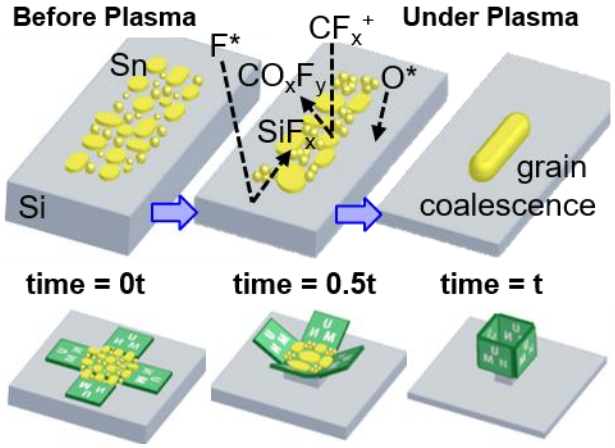

Figure 1.2 Schematic showing the reaction ion etching based self-assembly of nano-cubic structures [53].

1.2.2 Metal-Assisted Chemical Etching-based Self-Assembly

Metal-assisted chemical etching is a process of wet etching of Si by using metal as a catalysis. By patterning metal catalysts into 2D nanoscale templates, the enhanced etching can be confined to small area surrounding the template. Further, by designing the layouts and patterns of the metal catalysts template, difference etching speed can be assigned to different sections of the template. The difference in etching speed allows each parts of the template etching down in to the Si at a different time, achieving a folding behavior. Because of the folding process, the 2D template can finally be transformed into a 3D nanostructure [55].

1.2.3 Thin Film Strain -based Self-Assembly

The thin film strain-based self-assembly are based on the epitaxially grown heterojunction thin films [56-61]. The bilayer consists of two different materials with different lattice constants. Normally, the top layer material (GaAs) should originally have a smaller lattice constant while the bottom layer (InAs) should have a larger lattice constant

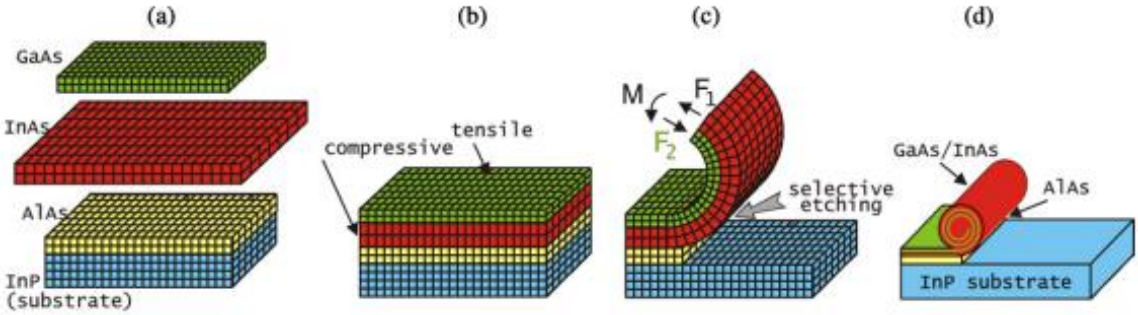

Figure 1.3 Schematics showing the mechanism of thin film strain induced self-assembly of nanotube [56, 61].

as shown in Figure 1.3a. When the bilayer is grown on the substrate, they will try to maintain the same lattice size. Therefore, the top layer will experience compressive strain and the bottom layer will experience tensile strain in the grown bilayer. Once this bilayer is detached from the substrate, the bilayer will deform so that each layer can reach to its intrinsic constant. Therefore, the top layer will shrink and the bottom layer will expand, leading to the upward curving into a nanotube (Figure 1.3d).

1.2.4 DNA-based Self-Assembly

Deoxyribonucleic Acid (DNA) is a double helix structure, which has unique interactions between complementary base pairs. This specific interaction makes it possible to control the shape and motion of DNA through carefully designing its base sequence [62-66]. The initial work of DNA origami is based on using short DNA strands as the "staples" to bind specific spots in long strands and further guide the folding of long strands [62]. By designing the location of binding spots, the long strands can be folded into intricate 2D or 3D structures [63]. Further, additional functional materials, such as Au nanoparticles, can be attached to the DNA strands, forming more complex 3D networks with advanced mechanical or optical properties [66-68].

1.3 Application of Self-Assembled 3D Nanostructures

The development of origami like self-assembly techniques significantly enrich the library of 3D nanostructures. Various 3D nanostructures, including cubes, tubes, and wrinkles, have been demonstrated through folding or curving processes [50-67]. These

self-assembled 3D nanostructures show great potential in achieving novel phenomena due to their ability of property engineering [69], 3D space utilization [70], and controlled motion [71], which can trigger vast amount of advanced applications in different fields. Some of the major innovations are focused on surface wettability modification [72-76], 3D optical devices [19, 77-84], and nanorobotics [85-89].

1.3.1 Surface Wettability Modification

Wettability of a solid surface is a common phenomenon in nature and has inspired enormous applications, ranging from coatings, heat transfer, and liquid modification, to chemical and biological screening [90-92]. A surface with self-assembled 3D nanostructure is one of the major strategies to tune the surface wettability [72-76]. The topology of the 3D nanostructure directly affects the surface energy, which determines the wettability [76]. For instance, 3D nanoscale wrinkles generated *via* strain relief of the substrate has shown the capability to program surface wettability [72-75]. By modifying the topology of wrinkles, the surface can achieve all the wetting states from superhydrophobic to superhydrophilic [74]. With precise design of the 3D nanostructures, the interaction between the liquid and surface can be further controlled, leading to programmable liquid film thickness and final wetted liquid shape [76]. One example is the surface with curving pillars fabricated *via* residual stress [76]. The curving pillars enable precise modification of the surface energy, assigning different surface energy to specific spots within a small area. This differential surface energy results in uni-directional liquid spreading on a surface [76].

1.3.2 Advanced Optical Devices

The 3D nanostructures can also serve as unique platforms for exploring novel optical behaviors that can hardly be achieved in 2D flat thin films. The self-assembly of 3D nanostructures features several advantages including unique 3D coupling [77-79], enhanced interaction [19,81], and tunable response [82]. First, the 3D nanostructures can form unique 3D artificial architectures, which can achieve enhanced or even inexistent optical behaviors compared to 2D. For example, the self-assembled 3D twisting nanostructures are desirable platforms to achieve intrinsic optical chirality, which only exist in 3D [79]. Second, the 3D configurations enable the enhanced interaction with incident light due to the full utilization of 3D focal volume [19, 81], which can improve the behavior of the device. A 3D plasmonic sensor with higher sensitivity [19] and a 3D metamaterial with higher quality factor [81] have been demonstrated through this strategy. Third, some of the self-assembly process with reversible functions can be used to build optical devices with tunable responses. A resonator that can be reversible folded demonstrate a switchable resonance from long wave to mid-IR regime [82].

1.3.3 Nanomachine

The origami like self-assembly is a powerful tool for building nanomachines. On one hand, the motion of nanoscale materials involved in self-assembly aligns well with the fundamental requirement of nanomachine or nanorobotics. A controllable self-assembly process actually demonstrates the basic function of a nanomachine. DNA molecular nanomachine has been achieved based on DNA origami process, which can perform linear, rotational and reciprocating movement [85, 86]. On the other hand, the 3D configuration

of self-assembled nanostructures makes it possible to be used as the frame of a nanomachine. Additional functional modules, such as sensing and power components, can be integrated onto the self-assembled 3D nanostructures, forming a powerful nanomachine [87-89]. Self-assembled tubular nanostructure becomes a widely used nanomachine model due to its asymmetric inner and outer surface [87]. The inner surface is normally decorated with catalyst or reactive materials, working as the power system of the nanomachine. While, functional components are incorporated on the outer surface to conduct specific tasks.

1.4 Motivation: Current Issue of Nanoscale Self-Assembly

Self-assembly of three-dimensional (3D) nano-structures arises to be a broad topic due to their ability of property engineering, 3D space utilization, and controlled motion, which have been widely used in the applications of surface modification, nano-optics, and nano-machines. Recently, great development has been achieved in nanoscale origami like self-assembly techniques. However, it remains challenging to precisely control the process as it involves intricate transformation of two-dimensional (2D) thin film into 3D architectures. Since the structural transformations are dynamic, they are easily affected by variations during reactions. Small differences in temperature, pressure, and dimensions before or during self-assembly, which are inevitable, will result in unexpected movements of nanostructures [50]. Moreover, the structures are in nanoscale so that they are not able to be visualized during self-assembly, making it impossible to apply instant adjustment of reaction conditions to compensate the disturbance induced by the small variations. Thus,

these self- assembly techniques suffer limited control of the assembly morphology, which bring great challenge for fully exploring their advantages and diverse applications.

To address this issue, ion and electron irradiations in scanning microscopes stand out as two promising candidates due to their capability of inducing localized programmable stimuli and providing real-time observation. The ion or electron beam in a focused ion beam (FIB) system or a scanning electron microscope (SEM) enable precise delivery of irradiated particles (ie. ions or electrons) to a specific nanoscale area and generate localized stress to drive self-assembly process through various irradiation-matter reactions. In addition, the imaging ion or electron beam empowers the visualization of this process, which can instantly guide the localized stress to realize assembly with nanoscale precision. Because of the combined advantages, the yield and complexity of the self-folding processes are significantly improved. This strategy provides the possibility to create intricate 3D architectures with advanced physical and chemical properties, leading to innovation of functional applications in diverse fields.

In this thesis, I first report the study of RIE-based self assembly process in Chapter 2, where I investiagte the mechanism of energetic irradiation (plasma) induced material phase change (grain coalescence) and propose a strategy to quickly achieve successful assembly. In Chapter 3, I apply the stress generation mechanism based on ion-material interaction to a FIB-based self-assembly process, which enables real-time monitoring of assembly, resulting in ultra-high yield. Next, I report an electron irradiation triggered self-assembly process in Chapter 4, which demonstrates sequential and reversible assembly, paving the path to create intricate 3D functional nanostructure, such as tertiary structures.

Based on these assemble processes, two applications, gap-based plasmonic cylindrical nanosensor and functional graphene-based 3D nanostructures, are demonstrated, which are described in Chapter 5 and Chapter 6 respectively. The gap-based plasmonic cylindrical nanosensor utilize the self-curving process to automatically form a plasmonic nanogap in a nanochannel, which can achieve both the light and liquid confinement, improving the sensing behaviors. In Chapter 6, we introduce self-assembly of graphene-based nanostructures, which is one of the first work to fabricate 3D nanostructures with 3D materials in the field. This achievement adds an additional dimension to 2D materials and provides a new concept to further explore the advantages of 2D materials. We theoretically study the plasmonic behaviors of 3D graphene nanostructures and proposal a strategy to achieve higher sensitivity using graphene-based cylindrical structures.

Chapter2

Plasma Triggered Self-Assembly

In this chapter, I introduce the fundamentals of plasma triggered self-assembly. The self-assembly process is based on surface tension force generated by plasma triggered grain coalescence. Therefore, the mechanism of plasma triggered grain coalescence is first discussed in detail. Further, I will cover the effect of grain coalescence and etching profile on self-assembly. Finally, a strategy is proposed to guide successful assembly of 3D nanostructures utilizing surface tension force driven by nanoscale grain coalescence.

2.1 Introduction to Plasma Triggered Self-Assembly

2.1.1 Nanoscale Grain Coalescence

Nanoscale metal grain coalescence in thin-films after deposition is a process which accompanies sintering and densification of nanoparticles [93]. Phase and morphology changes resulting from grain coalescence induce advanced properties, which have been utilized in changing thin-film dielectric properties [94, 95], nano-welding [96 -98], and self-assembly of 3D nanostructures [37, 50, 51, 52, 77, 99, 100]. In particular, the use of grain coalescence for the self-assembly of 3D nanostructures attracts great attention due to the ability of these structures to explore new physical and chemical phenomena for building next generation nanodevices.

Plasma surface reaction, which enables controllable heat generation, is one of the approaches for triggering grain coalescence and controlling the coalescence performance

[101-103]. Specifically, numerous plasma etching systems exhibit localized heat generation in the area of plasma/surface interaction [104-109]. The plasmochemical reactions in these plasma etching systems are exothermic and able to thermally stimulate a wide range of physical processes and chemical reactions [108, 109]. In addition, ion bombardment also happens in plasma etching systems, which contributes to heat generation by transferring kinetic energy [110-113]. As a result, the extreme heat generated on the surface of the reaction area is able to melt the grains and trigger grain coalescence in metal thin-films [37, 50, 51, 52, 77, 99, 100]. The heat generation is determined by the reaction rate of the plasma etching, which can be controlled by plasma power and ratio of gas flow rates. Therefore, the performance of grain coalescence can be thermally controlled by tuning the reaction parameters.

2.1.2 Theory of Plasma Triggered Self-Assembly

The self-assembly processes normally require a continuous bilayer or hinged networks, which consists of a frame layer and a responsive hinge layer. To trigger self-assembly process, grain coalescence should be induced in the hinge layer. A s a result of grain coalescence, a surface tension force is induced in metal thin-films, when nanoscale grains liquefy. The surface tension force curves or rotates the underlying panels out of plane forming the 3D nanostructures[37, 50, 51, 52, 77, 99, 100].

2.1.3 Current Issues of Plasma Triggered Self-Assembly

Although grain coalescence in tin (Sn) metal films was previously demonstrated in a reactive ion etching (RIE) system, which utilized the principle of plasma etching, and surface tension force generated by grain coalescence was used for assembly of both curved

and polyhedron nanostructures [37, 50, 51, 52, 77, 99, 100], the effect of different conditions in the plasma etching system on grain coalescence has not been systematically studied. This brings great challenges in controlling the performance of grain coalescence, making the assembly of 3D nanostructures difficult to be reproduced on different structures.

Therefore, I take advantage of the controllable heat generation of plasma etching to achieve the desired grain coalescence for a self-assembly process. The grain coalescence in Sn thin-films induced by RIE of silicon substrates with the gases tetrafluoromethane (CF_4) and oxygen (O_2) has been explored, and it is found that the power and ratio of gas flow rates (CF_4/O_2) in a RIE process show great effects on the morphologies of the grain coalescence as well as the self-assembled 3D structures. In addition, the effects of the different grain coalescence performances and Si substrate etching profiles on the self-assembly process have been studied. Finally, an approach to control the self-assembly of 3D nanostructures has been developed.

2.2 Plasma Interaction with Sn

2.2.1 Fabrication and Analysis of Sn Strips

To study the grain coalescence induced under plasma, 1 μm wide strips were patterned by a lift-off process on a silicon (Si) wafer and then a 30 nm thick Sn film was directly deposited using an electron beam evaporator (Figure 2.1a,df). The RIE of Si with CF4/O2 was used to generate heat energy and trigger grain coalescence in the sample placed on the chuck, which is a powered RF electrode. Various parameters, such as the plasma power and ratio of gas flow rates (CF_4/O_2), were changed to investigate and control the morphology of the grain coalescence. The status of grain coalescence (γg) was

quantified by calculating the exposed area of the Si substrate between the grains within the Sn strip divided by the original area of the Sn strip by using computer software (Polygonal Lasso Tool in Photoshop) analysis of SEM images (γg = exposed Si substrate after a RIE process/original area of Sn strip before a RIE process).

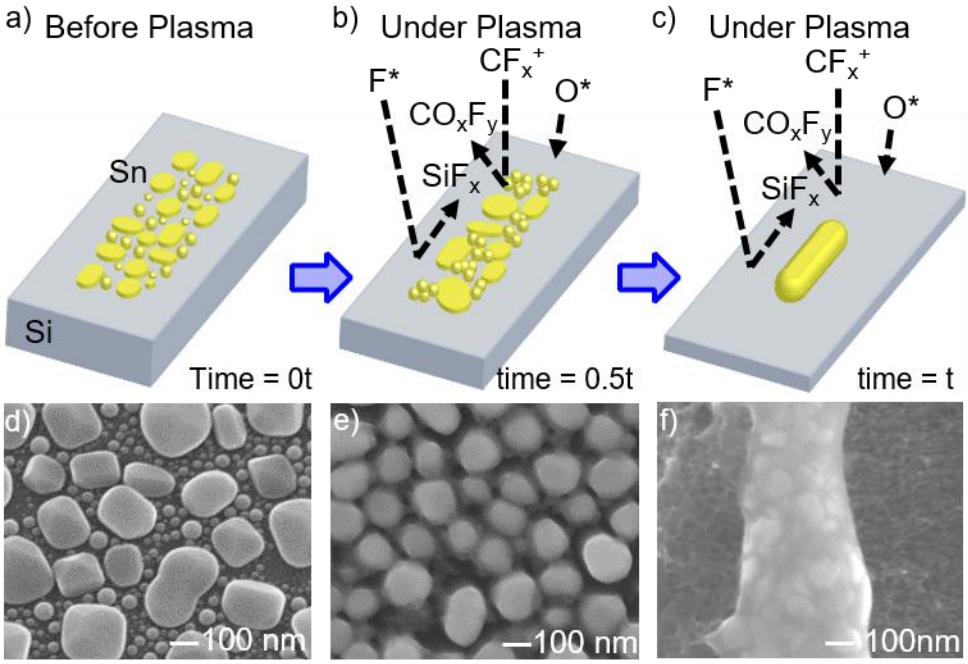

Figure 2.1 Conceptual schematics and scanning electron microscopy (SEM) images showing the grain coalescence process of Sn thin film during RIE process [53].

2.2.2 Mechanism of Plasma Triggered Sn Grain Coalescence

The Sn film shows grainy morphology on the Si, Ni, and Al_2O_3 substrate because the surface tension of the Sn film exceeds that of the substrate, [52] (Figure 2.1a, d). To generate heat energy and trigger grain coalescence, the RIE of Si with CF_4/O_2 was used. In the plasma etching process, the chemical reaction between fluorine radicals and Si atoms produces the volatile products difluorosilicon (SiF_2) and silicon tetrafluoride (SiF_4) and is

able to remove Si atoms from the surface [110,114]. Additionally, as a feature of RIE, the ion bombardment (physical interaction) of active ion species like CF_x^+ also contributes to the etching (Figure 2.1b, c) [115]. Both the chemical and physical reactions in the RIE process are exothermic and can generate localized extreme heat energy at the interface of the plasma and the Si substrate. As a result of the localized heat, the small Sn grains deposited on the Si substrate will start to melt and merge into large grains (Figure 2.1b, e). With further etching of Si, the large grains will melt and coalesce with each other, forming one unit (Figure 2.1c, f).

2.2.3 The Effect of RIE Parameters on Grain Coalescence

To understand and control the grain coalescence triggered by RIE, the effects of plasma power, ratio of gas flow rates, and etching rate of the Si substrate were systematically explored. In the experiment, the pressure and etching time were kept constant at 100 mTorr and 4 min 30 sec, and a series of plasma powers of 40, 120, and 200 W were applied in a RIE system (STS Etcher 320). A fixed CF_4 flow rate of 12 sccm combined with varying O_2 flow rates of 5, 15, and 30 sccm was used in the RIE process, resulting in ratios (O_2/CF_4) of 0.42, 1.25, and 2.50. The various morphologies of grain coalescence caused by different combinations of power and ratio of gas flow rates were clearly observed (Figure 2.2). As shown in the figure, while a higher ratio of O_2/CF_4 shows an inhibition on the coalescence, an increased power contributes to greater grain coalescence. The observation was rationalized by noting the plasma power and ratio of flow rates are essential for the etch rate, thereby affecting heat generation, resulting in different morphologies of grain coalescence (Figure 2.2). On one hand, plasma power of a

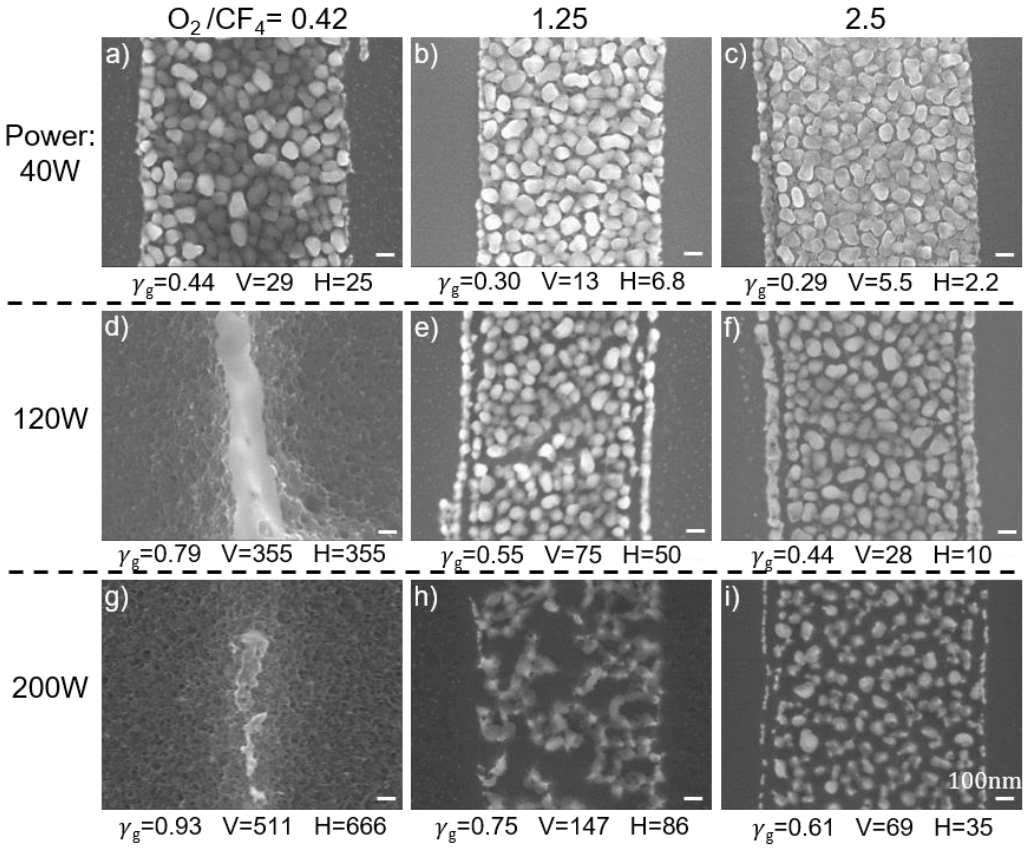

Figure 2.2 SEM images of the grain coalescence after a 4min 30sec RIE process with varying power (40, 120, and 200 W) and ratio of O_2 over CF_4 (O2 /CF4 = 0.42, 1.25, and 2.50). The pressure and CF_4 flow rate are fixed to be 100 mTorr and 12 sccm, respectively. A series of oxygen flow rates of 5, 15, and 30 sccm was applied to change the ratio of O2 over CF4. The value of quantified grain coalescence, vertical etch rate, and horizontal etch rate of each sample was labeled as γg (a.u.), V (nm/min), and H (nm/min), respectively, under each figure. The scale bars are 100 nm [53].

RIE process influences the fluorine concentration [116]. At higher plasma power, more CF4 gas molecules can be dissociated due to the sufficient high electron energy [116].

More fluorine atoms in the gas molecules can be released by the dissociational collisions and lead to a higher fluorine concentration than at low plasma power, which enhances the chemical etch rate of the Si substrate [116]. On the other hand, the kinetic energy of the ions, such as CF_x^+, will also be enhanced due to high bias voltages (plasma power). As a result, the ion bombardment would be more significant and contribute to a higher physical etch rate. Associated with the enhanced etch rate due to both chemical and physical etching, more heat is generated on the substrate, which induces a more significant morphological change in the Sn grains meaning greater grain coalescence (Figure 2.2). Moreover, additional O2 in the RIE chamber can initially enhance the etching due to the additional

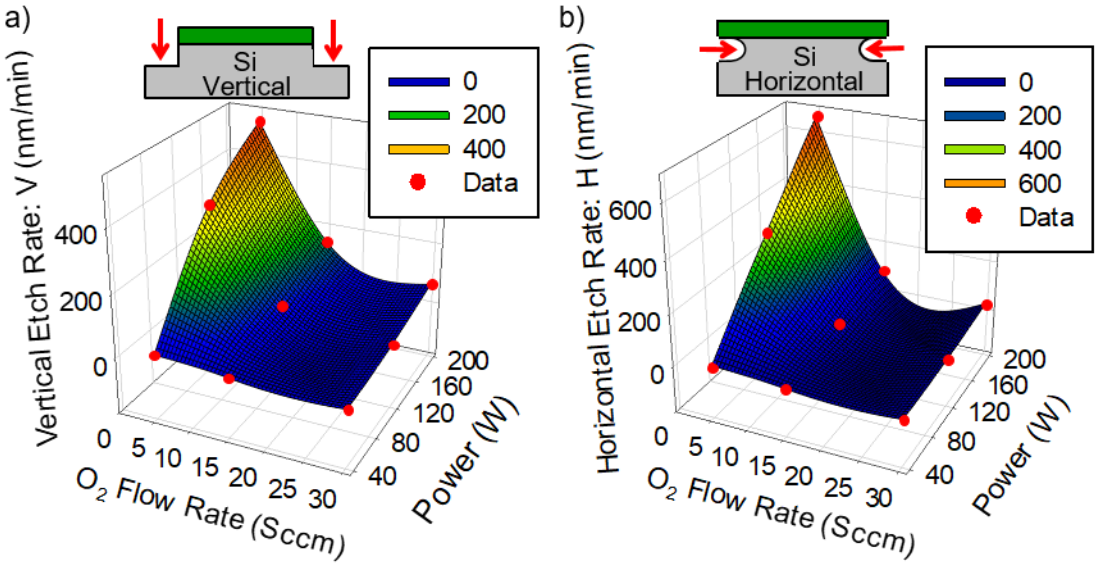

Figure 2.3 Experimental results of the variation of a) vertical etch rate, and b) horizontal etch rate in the RIE process with varying power (40, 120, and 200 W) and varying ratio of O_2 over CF_4 (0.42, 1.25, 2.50). The pressure and CF_4 flow rate are fixed to be 100 mTorr and 12 sccm respectively. Oxygen flow rates of 5, 15, and 30 sccm are utilized to control the ratio of oxygen over CF_4 [53].

atomic fluorine created by the reaction between O2 and radicals like CF3 [117, 118]. Previous work has observed greater grain coalescence caused by increasing the O_2 flow rate in this regime, where the percentage of O_2 in the mixture gas is low [51]. When the percentage of O_2 exceeds 5% in the gas mixture, which is the case discussed in this paper, a significant passivation film of SiF_xO_y can be formed on the surface due to the high O_2 flow rate [119]. The passivation layer cannot be removed by fluorine atoms and it prevents the sputtering of Si by the CF_x^+ ion bombardment. Hence, the etch rate was greatly reduced (Figure 2.3). This low etch rate of Si resulted in less heat generation and no obvious grain coalescence. Therefore, the clear effect of the etch rate, as a function of gas flow rate and plasma power, on grain coalescence demonstrates that localized heat generated in plasma etching triggers the grain coalescence.

During the grain coalescence, the small grains merge into each other to form large grains to reduce surface area for minimizing surface energy. Therefore, the surface area of the grains can be used as a parameter to evaluate the grain coalescence. To quantitatively study the effect of the plasma parameters (i.e., gas flow rate, plasma power, and etch rate) on the grain coalescence, the status of grain coalescence (γg) was quantified by calculating the exposed area of Si substrate between the grains, within the Sn strip, divided by the original area of the Sn strip by using computer software (Polygonal Lasso Tool in Photoshop) (γg = exposed Si substrate after RIE/original area of Sn strip before RIE). As the Sn is directly deposited on the Si substrate, even though the Sn grain flow after melting, it will still stay on Si surface and can be measured. In addition, the data is collected based on average value of grains, which can minimize the error. Higher values of γg indicate

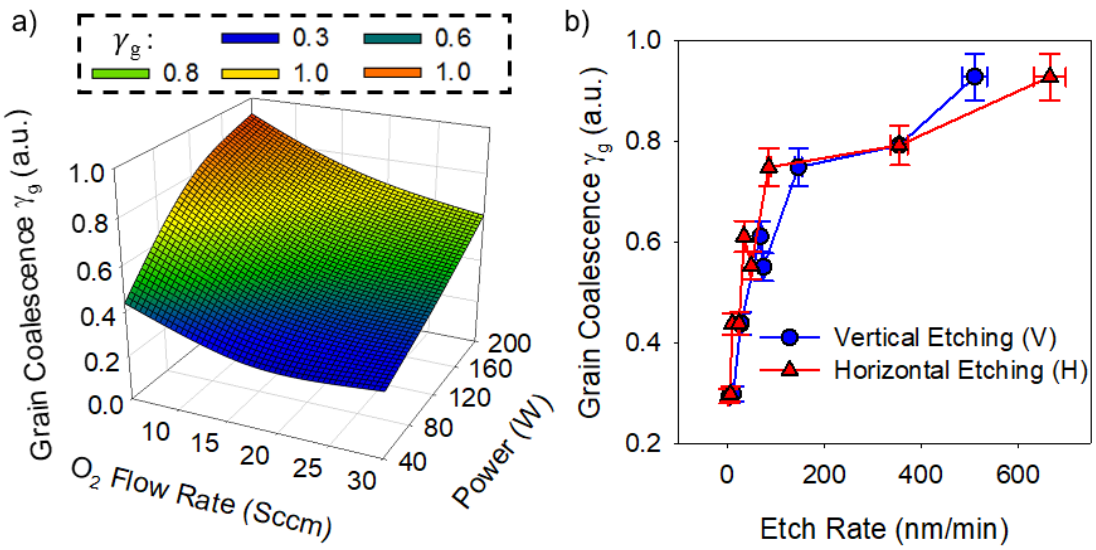

Figure 2.4 a) Quantified grain coalescence in a RIE process with varying power (40, 120, and 200 W) and varying ratio of O_2 over CF_4 (0.42, 1.25, 2.50). The pressure and CF_4 flow rate are fixed to be 100 mTorr and 12 sccm, respectively. Oxygen flow rates of 5, 15, and 30 sccm are utilized to control the ratio of oxygen over CF4. b) The relationship between the grain coalescence and both the vertical and the horizontal etch rates [53].

more significant grain coalescence (Figure 2.2 and 2.4a). The data shown in Figure 2.4 were generated from Figure 2.2. It is clear the grain coalescence (γg) was more significant with lower oxygen flow rate and higher plasma power (Figure 2.4a), which was consistent with both the changing trend of horizontal and vertical etching rates according to the oxygen flow rate and plasma power shown in Figure 2.3. The oxygen flow rate affects the etching rate, which affects grain coalescence; with high flow rates of O_2, a passivation layer of SiF_xO_y forms on the surface of the Si substrate, resulting in a low Si etch rate and less heat generation. Therefore, morphology of weak grain coalescence (low γg) was observed

for trials with higher oxygen flow rates (Figure 2.4a). Increasing the plasma power leads to an increase in the atomic fluorine concentration, enhancing the chemical reaction for etching Si. Additionally, the high plasma power intensifies ion bombardment, increasing thermal energy transferred to the Sn grains [110, 111]. Since both the chemical and physical reactions are exothermic, a high etching rate contributes to greater heat generation, resulting in more significant grain coalescence.

To further investigate the mechanism of grain coalescence, the direct relationship between grain coalescence and both the vertical and the horizontal etching rate are plotted (Figure 2.4b). As shown in the figure, the grain coalescence shows an overall increasing behavior with both increasing vertical and horizontal etching rate until the etch rate of 100 nm/min is reached. However, as the etch rate increases further (> 100 nm/min), the amount of grain coalescence saturates. This could be caused by the limited volume of the Sn grains. Since the volumes of the Sn grains are in nanoscale, the heat generated on the Si substrate, within the high etch rate region, can easily reach the required level for triggering significant grain coalescence. Once significant grain coalescence has been triggered, further increase of the heat generation cannot significantly speed up the process due to the limited volume of the Sn grains, thereby causing the saturation region (Figure 2.4b). The results demonstrate grain coalescence can be easily controlled by adjusting the etching rate of the Si substrate; thereby indicating self-assembly of 3D nanostructures utilizing grain coalescence can be precisely controlled.

2.3 Self-Assembly Of 3D Nanostructures

With a better understanding of RIE triggered grain coalescence, I move forward to

develop a strategy for achieving successful self-assembly. Both the surface tension force generated during grain coalescence and the release of structure should be precisely controlled. The strategy has been demonstrated useful for assembly of nanocube and nanotube.

2.3.1 Fabrication of 2D Sample

Fabrication of 2D nets for self-assembly of cubic structures. To utilize grain coalescence for triggering self-assembly of 3D nanostructures, 20 nm thick nickel (Ni) 2D nets with five square nanoscale panels (with dimensions of ~ 500 × 500 nm) were first defined, with "UMN" lettered patterns on the surrounding four panels, on a Si wafer by an electron beam lithography (EBL) process. On top of the panels, a 30 nm thick Sn hinge was patterned (Figure 2.5a). After the EBL process, reactive ion etching with CF_4/O_2 was used to induce Sn grain coalescence and realize the assembly of 3D nanostructures from the 2D nets (Figure 2.5b, c).

Fabrication of 2D ribbon for self-assembly of tube structures. To demonstrate the mechanism can be applied to different structures, 2D ribbons (with dimensions of ~ 300 × 2000 nm) were defined on a Si wafer by an electron beam lithography (EBL) process. After developing, 3 nm aluminum oxide (Al2O3) and 2.5 nm Sn were deposited to form the ribbon (Figure 2.5d). After the lift-off process, reactive ion etching with CF_4/O_2 was used to induce Sn grain coalescence and realize the assembly of tube structures (Figure 2.5e, f).

2.3.2 Driving Force for Self-Assembly

As a consequence of grain coalescence, a surface tension force is induced in the Sn thin-film. Once the grain coalesce is triggered in the Sn hinges of 2D structures, the surface tension force can lift up (Figure 2.5 a-c) or curve up (Figure 2.5 d-f) the underlying layers out of the plane (Figure 2.5 b, e), transforming them into 3D nanocube (Figure 2.5 c) or nanotube (Figure 2.5f). Therefore, one of the major factor for successful self-assembly is to achieve significant grain coalescence to provide sufficient surface tension force.

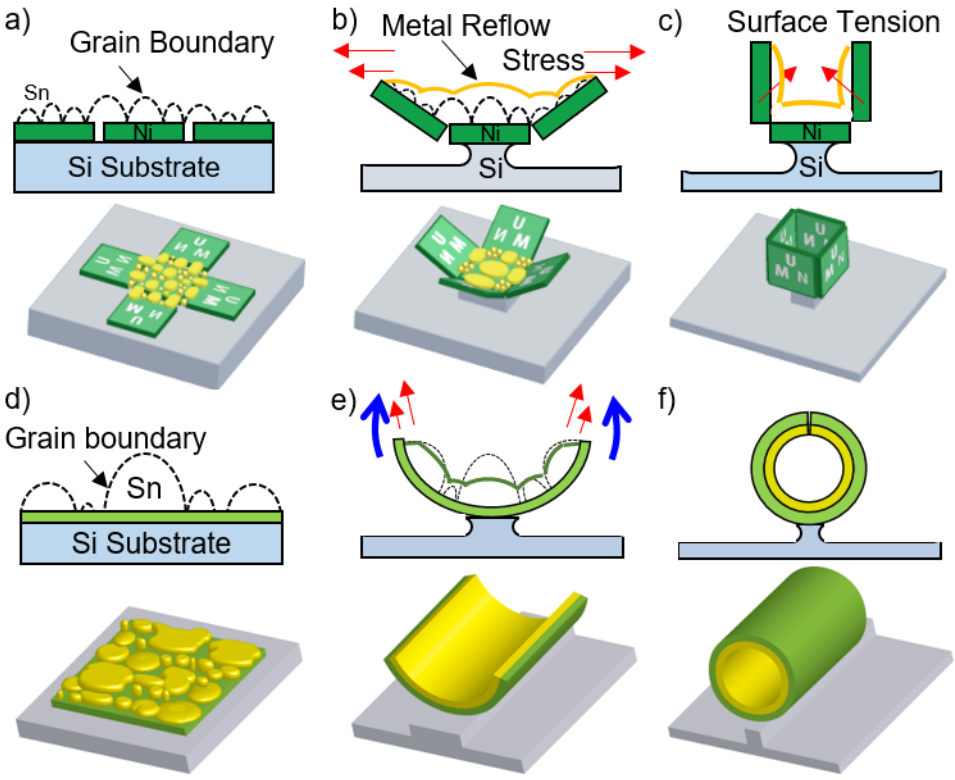

Figure 2.5 Conceptual schematics showing the origin of the extrinsic stress and surface tension force observed within the Sn film that causes the a-c) discontinuous frame to fold up or d-f) the continuous film to curve up [53].

The importance of grain coalescence on nanoscale self-assembly is shown in Figure 2.6. The pressure and etching time of the RIE process for self-assembly were fixed at 100 mTorr and 4 min 30 sec, respectively, which are the same values as used in Figure 2.2. The plasma power of 120 W and varied ratio of gas flow rates (O_2/CF_4) of 1.25 and 2.50 were selected because these conditions showed dramatically different grain coalescence (γ_g = 0.552, and 0.437, respectively) (Figure 2.2 e-f). With the gas flow ratio of 2.50, no significant grain coalescence (γ_g = 0.437) was observed. This indicates the surface tension forces generated in the hinges are not sufficient to fold the panels and transform the 2D nets into 3D nanostructures even though the panels were completely released from the substrate (Figure 2.6a). With a lower gas flow rate ratio (1.25), the grain coalescence with some portion of large grains was triggered in the Sn hinges, which induces surface tension forces in the hinges and transforms the 2D nets into uniform 3D nanostructures with a folding angle of 45° (Figure 2.6b) (time for applying RIE was ~ 4 min 30 sec).

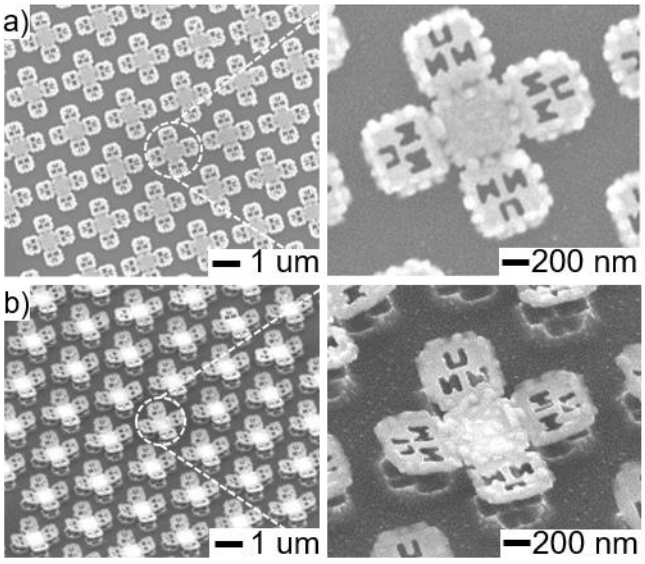

Figure 2.6. SEM images of self-assembly result with different surface tension force [53].

2.3.3 Importance of Etching Profile

It is still insufficient to only control the surface tension force for achieving the uniformly assembled (homogeneous) 3D nanostructures. For example, a RIE recipe that can trigger considerable grain coalescence (Figure 2.2d) is used for self-assembly (Figure 2.7). However, only parts of the panels were folded to an angle of 90° and no successfully folded 3D nanostructures were observed for this recipe (Figure 2.7). This is because the central panel is released from the substrate before the grain coalescence if fully activated. Without a stable connection between the Si substrate and the nanostructures, it is difficult to uniformly transfer the localized heat to the structures; hence, no uniform 3D structure can be achieved. Therefore, the release of the panels, which is determined by the etching profiles, should also be precisely controlled to achieve completely folded, homogeneous, 3D nanostructures.

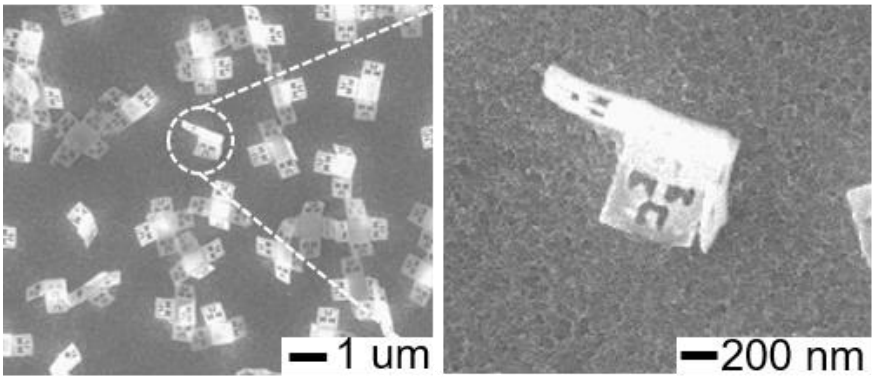

Figure 2.7 Considerable heat generation and grain coalescence does not contribute to fully folded structures. Only parts of the panels get folded more than 90° [53].

2.3.4 Strategy for Successful Self-Assembly

For a successful assembly of the3D nanostructures, the grain coalescence and release of the panels from the substrate should be balanced. The RIE process should be

well controlled to achieve desired vertical and horizontal etching rate, which is responsible for not only triggering grain coalescence but also releasing the surrounding panels from the substrate. A desired ratio makes it possible to generate enough heat energy while only the surrounding panels are completely released, forming uniform 3D nanostructures. Otherwise, if the horizontal etching much more actively occurs, the structures will be released before sufficient grain coalescence is triggered, causing the structures to not be fully folded. On the other hand, if the horizontal etching rate is much lower than the vertical etching rate, the surrounding panels will not be released during the Sn grain coalescence, resulting in unfolded structures. Therefore, for self-assembly of 3D nanostructures.

2.3.5 Control of Vertical/Horizontal Etching Ratio

For controlling the etch rate ratio (vertical/horizontal), the ratio of O_2 flow rate over CF_4 is the dominant factor. At low gas flow rate ratios (O2/CF4), chemical reactions between fluorine and silicon atoms dominate the etching process. As the chemical reaction has no directionality, the etching profile is isotropic, which means the etch rate ratio (vertical/horizontal) is around 1 (Fig. 6(a)). With an increasing gas flow rate ratio, a passivation layer of SiFxOy, induced by high oxygen flow rate, forms on the surface of the silicon substrate. The passivation layer can only be removed by ion bombardment rather than the chemical reaction. As the ion bombardments are in the vertical direction, the vertical etch rate (V) becomes more significant compared to horizontal etch rate (H) (Figure 2.8). Therefore, increasing gas flow rate ratio (O_2/CF_4) could monotonically increase the ratio (V/H) of vertical etch rate over horizontal etch rate (Figure 2.8).

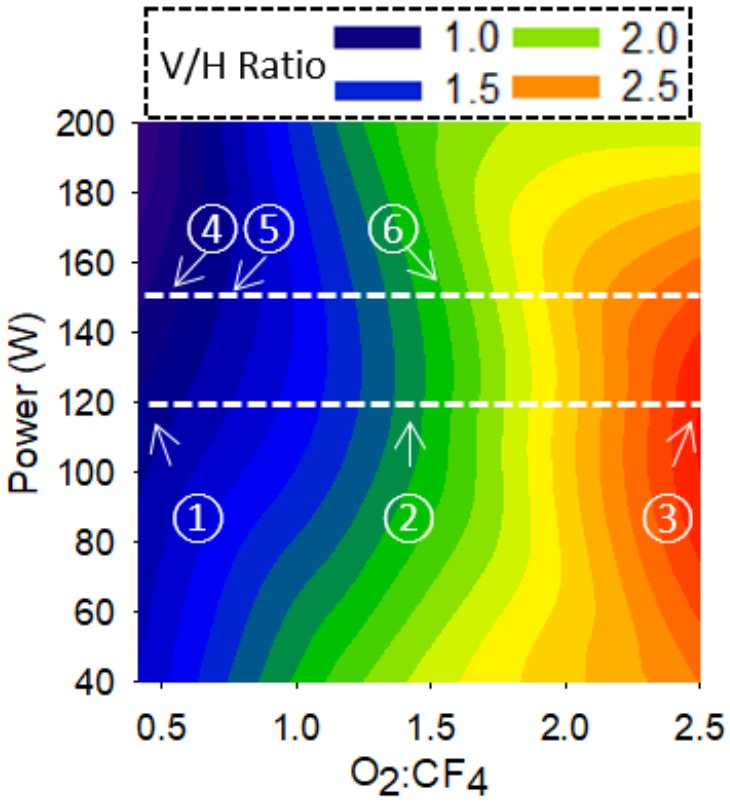

Figure 2.8 The ratio of vertical etch rate over horizontal etch rate in a RIE system with fixed pressure of 100 mTorr and various power and gas flow rate ratio [53].

2.3.6 Self-Assembly of 3D Nanocubes

The strategy and map of etch rate ratio (Figure 2.8) has been used to guide the assemble of nanotube. At a low oxygen flow rate of 5 sccm (O_2/CF_4=0.42), the ratio of vertical etch rate over horizontal etch rate (V/H) is low. At the point in time when the nanostructure is fully released from the substrate, a relatively low amount of Si is vertically etched, which results in insufficient heat generation, leading to insignificant grain coalescence. Hence, there is not enough surface tension force generated in the Sn hinge films to fold all surrounding panels up to 90° until right after the central panel has already been released from the Si substrate (Figure 2.9 a, the left inset SEM image pointing ①,

the RIE conditions highlighted with a dash line in Figure 2.8 corresponds to the RIE conditions and results shown with a solid line in Figure 2.9a). Once the structure is released from the substrate, there is no stable connection between the nanostructures and the substrate, making it difficult to uniformly transfer heat to the nanostructures. Even though significant heat has been generated by further application of RIE after the central panel is released, there is still no sufficient grain coalescence in some of the Sn hinges due to the difficulty of heat transfer. As a result, no uniformly folded 3D nanostructures can be achieved. In addition, significantly increasing the etch rate ratio to 2.80 by applying a high oxygen flow rate of 30 sccm (O_2/CF_4 = 2.50), which relatively increases vertical etching and decreases horizontal etching, is also not able to achieve successful self-assembly. The low horizontal etch rate contributes to a long etching time to release the surrounding panels. During this process, a large amount of Si can be etched because of the long etching time and relatively high vertical etching rate, making the Sn hinge completely melt and disperse away from the panels before the surrounding panels are released. Since the Sn hinges on and between the panels were already removed prior to the release of the outer panels from the substrate, the 2D nets can no longer be folded (Figure 2.9a, the right inset SEM image pointing ③). Therefore, by considering both the grain coalescence and etching profile, an oxygen flow rate of 15 sccm (O_2/CF_4 = 1.25), which leads to an etch rate ratio of 1.50, was used. With this recipe, the assembly of completely folded 3D structures is successfully performed because sufficient surface tension force is induced in the thin-films in proper timing with the release of the surrounding panels, while the central panel is still connected (Figure 2.9a, the middle inset SEM image pointing ②). Therefore, a recipe with a pressure

of 100 mTorr, power of 120W, CF_4 flow rate of 12 sccm, O_2 flow rate of 15 sccm, and RIE time of 5 min 30 sec shows the ability to assemble the 3D polyhedral nanostructures.

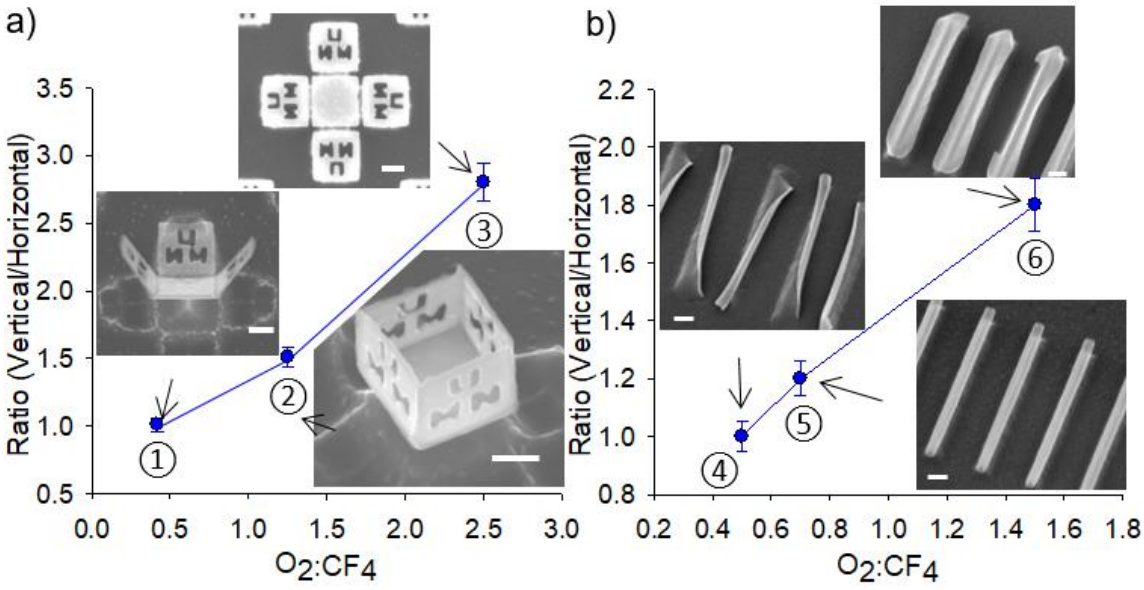

Figure 2.9 The effect of etch rate ratio on self-assembly of a) cubic structures with a fixed power of 120 W and b) tube structures with a fixed power of 150 W. The six data points in a) and b) correspond to the labeled points ① - ⑥ in Figure 2.8 [53].

2.3.7 Self-Assembly of 3D Nanotubes

Although the structures with different size and shape require different heat generation and structure release process, this strategy can be used as guidance for self-assembly, which will greatly reduce the time for optimizing the recipe. For new structures, different power should be first tried to achieve initial folding or curving performance even though it is not completely or uniformly self-assembled. Then the gas flow rate ratio should be tuned to optimize the process for successful self-assembly.

To demonstrate that the strategy's universality, it is directly be used to guide the self-assembly of tube structures (Figure 2.9b). After figuring out the power of 150 W, the gas flow rate ratio was optimized to achieve the successful self-assembly process. At the O_2/CF_4 ratio of 0.5, the vertical to horizontal etching rate ratio is 1, which cannot accumulate enough energy to self-assembly of the tube before releasing it form the substrate, resulting in ununiformed partially folded tube structure (Figure 2.9 b, the left inset SEM image pointing ④). By slight increasing the O_2 to CF_4 gas flow rate ratio, the vertical to horizontal etching rate ratio can be increased to 1.2, which can generate more energy for folding the structures before releasing, resulting in totally folded tube structure (Figure 2.9 b, the left inset SEM image pointing ⑤). Similar to the trend of cubic structures, further increase of the O_2 to CF_4 flow rate ratio will lead to higher vertical to horizontal etch rate ratio (1.8), which make the Sn melted and flowed away from surface before the structure can be folded, leading to the failure of self-assembly (Figure 2.9 b, the left inset SEM image pointing ⑥).

2.4 Quick Summary

I have characterized nanoscale grain coalescence induced by heat generated by a Si etching process in a plasma etching system. Plasma power and gas flow rate ratio in the RIE process have been shown to have effects on the etching rate, which affects heat generation, impacting grain coalescence. This study highlights how the performance of grain coalescence can be controlled by tuning the power and gas flow rate ratio between O_2 and CF_4. In addition, substrate etching rates and etching profiles have been demonstrated to be the dominant factors affecting the self-assembly of 3D nanostructures

because they are responsible for inducing enough surface tension force and releasing the structures from the substrate, respectively. Also, the strategy has been demonstrated to be able to be used for various structures rather than only polyhedral structures. This study can serve as a guideline for self-assembly of 3D nanostructures utilizing nanoscale grain coalescence.

Chapter3

Ion Irradiation Triggered In Situ Monitored Self-Assembly

In this chapter, I address the limitation of invisible nanoscale assembly process and introduce the ion irradiation triggered in situ monitored self-assembly. The fundamentals of ion induced grain coalescence and polymer reflow are presented. The folding process are analyzed based on the measurement and modelling results. Further, the effect of metal hinge and polymer hinge on optical devices are discussed and compared.

3.1 Limitation of Invisible Self-Assembly

Multi-dimensional (i.e. 3D) nanostructures provide more possibilities to further alter the properties of the nanomaterials [120-124], leading to state-of-the-art applications in diverse fields. Therefore, great effort has been put into the development of 3D nanofabrication process, resulting in various advanced techniques. Reactive ion etching (RIE) [120], atomic layer deposition (ALD) [125], and metal-assisted chemical etching (MaCE) [55] based self-assembly processes have been developed to build 3D nanostructures. All of these assembly processes are dynamic, meaning they are achieved by inducing a force to move 2D pieces out of a plane and transform them into 3D structures. For example, heat generation in an RIE system is able to trigger metal reflow in thin films

to generate surface tension forces for self-assembly of 3D nanostructures [120]; deposition of material in an ALD process can induce an intrinsic stress gradient in the film to curl nanostructures [25]; and uneven etching in MaCE processes enable gravity to fold hinged 2D structures downward, leading to 3D structures [55]. Since the structures are in nanoscale, these dynamic assembly processes are easily affected by small variations. Even though a strategy for successful self-assembly has been developed in aforementioned Chapter 2, it still requires vast amount of effort to optimize the RIE parameters. Small differences in temperature, pressure, and dimensions before or during self-assembly, which are inevitable, require new self-assembly conditions, i.e. modified force and time. If new assembly conditions, i.e. optimized force and adjusted time, are not instantly applied, the new environment will lead to a deficit or surplus in the energy supplied to the structures, resulting in the failure of the self-assembly. Thus, in order to apply the right amount of force and time under varying environmental conditions to realize 3D metal-based nanostructures with nanoscale precision, an in situ monitored self-assembly process, which enables real-time observation of the self-assembly process, is required.

3.2 Self-Assembly based on Metal Hinge

3.2.1 Concept of the In Situ Self-Assembly Process with a FIB

The concept of the insitu self-assembly process with a focused ion beam (FIB) microscopy system is illustrated in Figure 3.1. In the FIB system, the accelerated Ga+ ions can cause both the ejection of sputtered particles and Ga+ ion implantation in the target sample (Figure 3.1a) [126]. As a result of sputtering, the oxide layer causing a high melting point

is removed, exposing pure Sn material under the ion stream. During ion implantation, the kinetic energy of the ion stream can be transferred into thermal energy through collision into the thin film [112, 113]. The temperature of the hinge material exposed under the ion stream reaches several hundred degrees Celsius [112, 113]. Such high temperature easily melts hinge and triggers metal reflow (Figure 3.1b-d). As a result of metal reflow, surface tension force is generated in the Sn thin film (Figure 3.1e-g), inducing a self-assembly process transforming 2D nets into 3D structures (Figure 3.1h-j). The metal reflow induced by the kinetic energy of the Ga^+ ions was clearly observed (Figure 3.1b-d) under a SEM. Before Ga^+ ion implantation, the Sn thin film shows grainy morphology due to the intermediate wetting tendency of Sn on Si (Figure 3.1b). However, after being treated by Ga^+ ions, the Sn grains melt and merge into nearby grains because of the heat transformed from the kinetic energy of the ions (Figure 3.1c, d). The kinetic energy of the ion stream, supplying energy for self-assembly, can be precisely controlled by adjusting the accelerating voltage, beam current, and irradiation time during the assembly process. By forming a Sn hinge between two planar panels, the force can be used for assembling the planar structures (2D nets) into 3D structures (Figure 3.1h-j). The grainy Sn film acting as the hinge material triggers folding performance rather than bending, which provides better control over the shapes formed. During the self-assembly process, in the FIB microscopy system, the secondary electrons and ions sputtered from the sample can be detected and used to generate real time images of the target sample [126], which makes in situ monitoring of the process possible. Though Ga implantation in the self-assembly process affects the performance of electronic or optical devices, it is possible to make a protection layer on the area that is sensitive to Ga implantation. As long as the thickness of the

protection layer is thicker than the ion implantation range, the Ga^+ ions will only be implanted in the protection layer and not cause damage to the electrical or optical devices defined under the protection layer. Also, the patterning properties of the FIB can be used to reduce the effect of Ga implantation. In the FIB system, the size, shape, and location of the ion projection area can be designed to only allow the hinge area to be exposed to the gallium ions rather than the whole sample. These two methods can greatly reduce the Ga implantation into the device and maintain the desired electronic or optical performance.

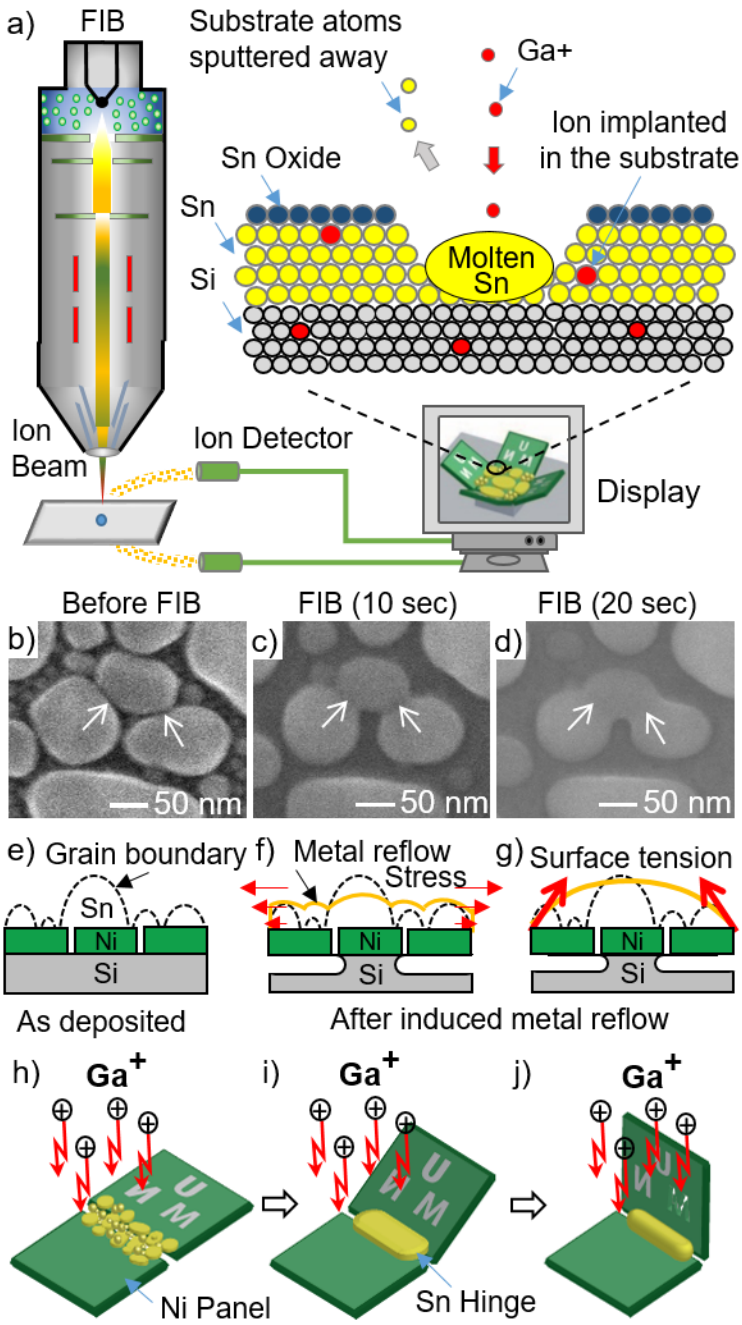

Figure 3.1 Conceptual schematics and SEM images showing the in situ self-assembly of 3D nanostructures by FIB. a) The instrument setup for an in situ self-assembly process. b-d) SEM images of the grain coalescence b) before and after ion irradiation for c) 10 and d) 20 sec. e-j) Sketches showing the origin of the extrinsic stress and surface tension observed within the Sn film that causes Ni to fold-up into 3D structures [111].

3.2.2 Fabrication of 2D Sample

To fabricate 3D polyhedral nanostructures, 2D nets, containing five square nanoscale panels patterned with the letters "UMN," were first defined on a Si wafer by an electron beam lithography (EBL) system. Nickel was used as the panel material due to its intermediate wetting property with Sn. The width and thickness of the panels were 500 nm and 30 nm respectively. The gaps between the panels were each 50 nm. A 35 nm thick Sn hinge was deposited over each gap by the EBL process to connect the panels. After the fabrication of the 2D nets, reactive ion etching (RIE, STS 320) with CF_4/O_2 was used to remove the Si underneath the structures. The gas flow rates of CF_4 and O_2 were kept at 40 sccm and 9 sccm, respectively. The chamber pressure was maintained at 100 mtoor during reaction. The RIE time was controlled to release the surrounding four panels from the Si substrate while keeping the central panel connected to the substrate. To minimize the effect of ion bombardment during the RIE process, a low power of 20W was used. The sample was placed facing the bottom of the RIE chamber, which significantly reduces the chances of the ions hitting the 2D nets, leading to flat, free-standing 2D nets, with the exception of the central panel of each net which was still supported by the substrate material.

3.2.3 Real-Time Monitored Assembly Process in FIB

After releasing the surrounding panels from the Si substrate (Figure 3.2a), a FIB system was used for the in situ self-assembly of 3D nanostructures. Once the Ga+ ions were applied to the sample, the temperature rose and melted the Sn hinges. Surface tension forces generated by the metal reflow lifted up and rotated each panel out of plane. Though

FIB is a line-of-site process, leading to a limited 3D structure, this problem could be partially solved by applying the incident beam with multiple angles. By tilting and rotating

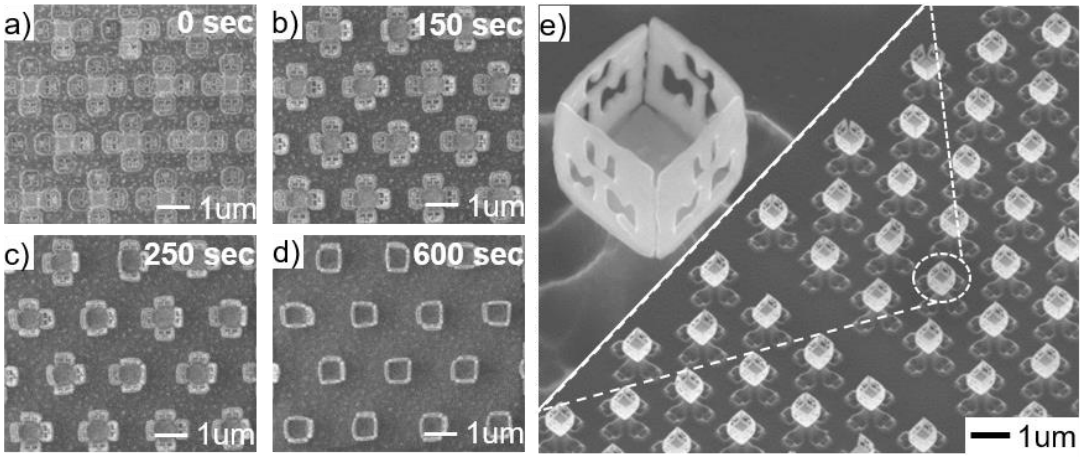

Figure 3.2 a-d) The real-time images of self-assembly captured by FIB a) at 0, b) 150, c) 250, and d) 600 seconds. e) SEM images of the large scale array of completed 3D cubic nanostructures with 35 nm Sn hinges. A "UMN" pattern is defined on each panel of the cubic structures. FIB enables real-time monitoring of self-assembly. The in situ self-assembly process can achieve the fabrication of a large scale array of 3D nanostructures with a yield of almost 100% [111].

a sample holder, various incident beam angles can be applied to the samples, reducing the shadow regions formed by the line-of-site process. Since the voltage and current of the Ga+ ion beam, which determine the ion projection power, can be precisely adjusted according to the real-time monitored status of the assembly process, it is easy to control the folding angle of the panels (Figure 3.2 a-d); therefore, various folding angles can be achieved. Also, the location of assembly is easily selectable by focusing the ion beam on a specific area of the sample. In addition, the magnification of the FIB can be easily tuned by zooming in

and out. The maximum and minimum possible assembly areas depend on the capabilities of a given FIB system. With high magnification, the FIB system (FEI Quanta 200 3D) used for this work enables the assembly of nanostructures defined on an area of sub-100 × 100 nm^2 size. Low magnification makes it possible for assembly over a large area. Because of the advantages of the in situ assembly process by FIB, a large-scale 3D nanostructure array was made with a high yield of almost 100% (Figure 3.2e).

3.2.4 Investigation of the Driving Force for Self-Assembly

A better understanding of the mechanism for triggering assembly by ion irradiation is required to achieve precise control of the self-assembly process and build diverse 3D nanostructures. Therefore, the mechanism of the self-assembly process under ion irradiation was systematically explored. It is known that curving nanostructures can be realized by applying a thermal gradient [127, 128], volumetric expansion [129], and void-induced stress generation [130, 131] under ion irradiation. However, all these mechanisms are not applicable for the case studied in this paper. A high aspect ratio is required for a nanostructure, like nanowire, to generate a thermal gradient inducing volume expansion for assembly. In the Sn hinges, there are no significant thermal gradients due to the small aspect ratio (height over width) of Sn grains. Also, the sizes of Sn grains showed a linearly decreasing trend under ion irradiation (Figure 3.3), meaning the etching performance is the dominant factor and the possibility of volumetric expansion is excluded. In order to test void-induced stress generation, Ga^+ ions with the same ion projection power (20 nW) but generated by different voltage and current combinations (3 pA at 10 kV and 1 pA at 30 kV) were injected into a 60 nm thick Sn film, and projection ranges of the Ga^+ ions were

simulated with a simulator (SRIM, v2008-04). The results of the simulation indicate the different voltage and current combinations result in different projection ranges (Figure 3.4), which should cause different void formation in the material and lead to different folding performance. However, the observed self-assembly processes under these two ion irradiations (3 pA at 10 kV and 1 pA at 30 kV) showed almost identical folding behavior during the overall assembly process from the beginning to when they completely folded up to 90° (Figure 3.5a). In addition, great similarity in the folding time (Figure 3.5b), angular speed of a folding panel (Figure 3.5c), and overall consumed energy (Figure 3.5d) for folding up to 90° was observed in the samples under these two irradiation conditions. This

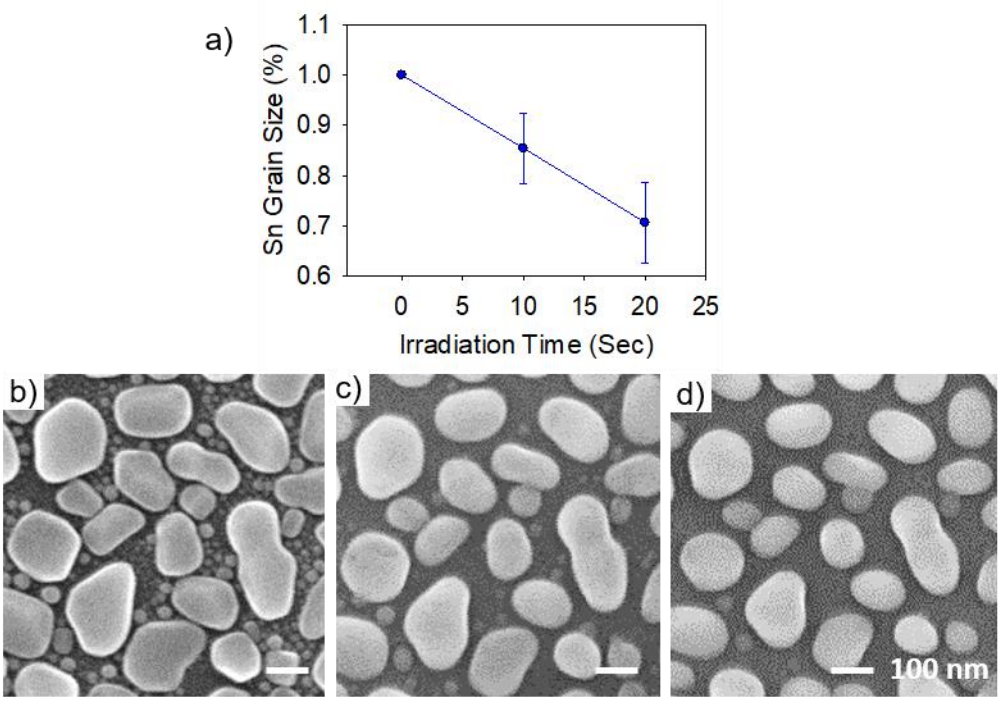

Figure 3.3 a) The measurement of Sn grain size before and after Ga+ irradiation. SEM images of the Sn grains captured b) before after irradiation at c) 10 and d) 20 seconds [111].

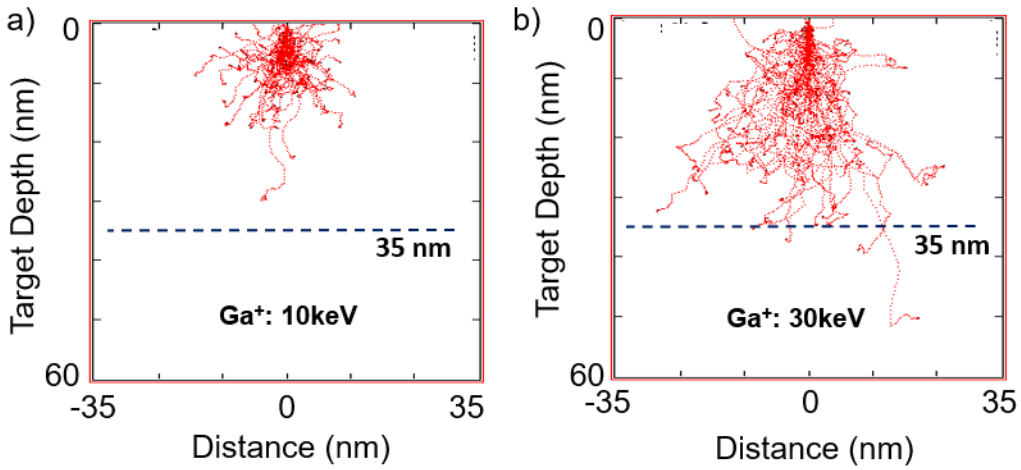

Figure 3.4. The simulation of implantation ranges of Ga^+ ions into Sn hinge materials. a) The gallium ions with energy of 10 keV have an implantation range of about 20 nm and most of the kinetic energy of the ions are transferred within this range. b) The gallium ions with a higher energy of 30 keV result in a higher implantation range of 30 nm and the energy is transferred into the deeper areas of the Sn hinge [111].

adequately justifies the mechanism of the self-assembly process as being induced by the metal reflow described in this paper. The similarity in self-assembly under the two different combinations of voltage and current is due to the same power of the ion bombardment. Even though Ga+ ions with 30 keV have a larger projection range than Ga^+ ions with 10 keV, the projection ranges of most ions are smaller than 35 nm (the thickness of the Sn hinge materials) as shown in Figure 3.4 in supporting information. Therefore, the two Ga^+ ion streams with the same amount of kinetic energy (ion projection power) contribute the same amount of heat energy, inducing metal reflow while the Ga^+ ions are embedding in the Sn film. The molten Sn hinges generate surface tension force for self-assembly,

resulting in the transformation of the 2D nets into 3D nanostructures (Figure 3.1e-g). It is also observed that ion irradiation with higher ion projection power results in a shorter time required for assembly to a 90^{o} folding angle (Figure 3.5b), which results from a higher angular speed (Figure 3.5c). The difference in folding time and angular speed are caused by the fact that a sample under an ion stream with low projection power requires a longer time to reach the energy required to induce metal reflow than a sample under an ion stream with high projection power. As shown in Figure 3.5b, the time for assembly to a 90^{o} folding angle is 600sec under the ion stream with 30 nW of power, which is much longer than 25sec, i.e. the time required for samples under the ion stream with high projection power (900 nW). To further analyze the process, the total ion energy required for a folding angle of 90° was obtained from the measurement shown in Figure 3.5a. As shown in Figure 3.5d, although the ion projection power varies from 30 nW to 900 nW (3000% change), the variation in the ion energy required for completed self-assembly is only ± 25% (Figure 3.5d), which is the expected result as addressed earlier. The slightly difference of the total required ion energy could be caused by energy loss via sputtering,, as well as variation of the structures' dimensions, such as Sn hinge thickness, induced in the fabrication processes.

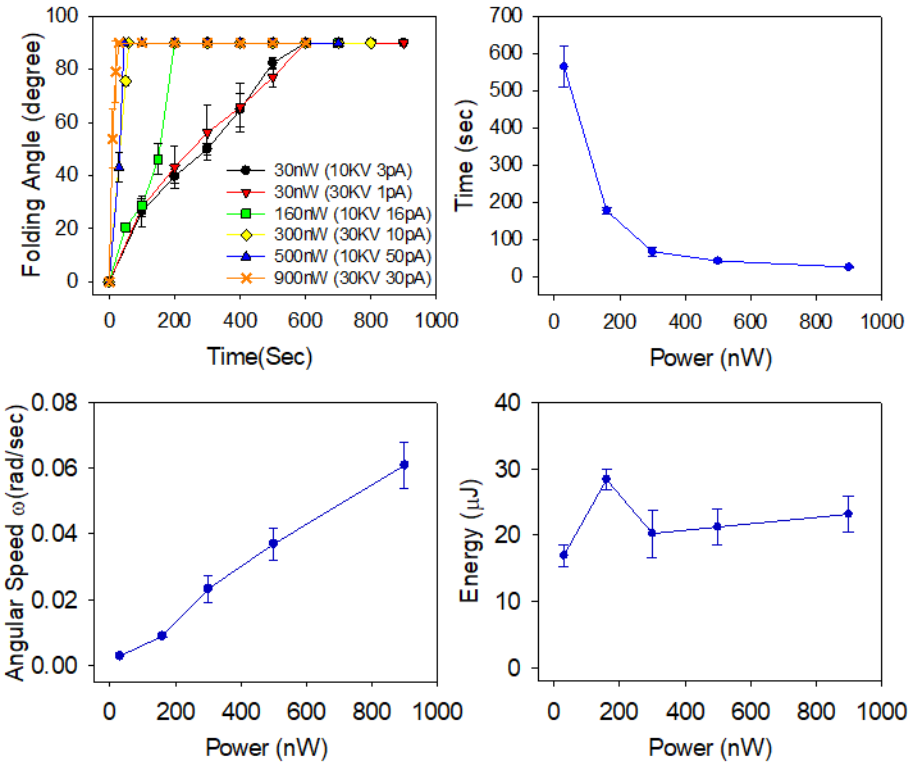

Figure 3.5 Various measurements showing the effect of current, voltage, and ion projection power on self-assembly. a) The folding angles of the nanostructure under ion irradiation with different current and voltage combinations. Same power but different current and voltage combinations result in the similar folding performance. b) c) The effect of power on b) folding time and c) angular speed. Ion irradiation with higher power requires a shorter folding time, resulting in higher angular speed. d) The total energy required for self-assembly with respect to the ion projection power varied from 30 to 900 nW. [111]

3.2.5 Effect of Hinge Thickness on Self-Assembly

To achieve further control of the self-assembly process, the effect of Sn hinge thickness on the self-assembly process was investigated (Figure 3.6). Sn hinges with

different thicknesses of 25, 35, and 45 nm were applied for the self-assembly of 500 nm sized cubic structures. Even though the largest projection range of Ga^+ ions with 30keV is larger than 25 nm, most ions stop within 25 nm. Therefore, most of the kinetic energy is converted into heat energy and is transferred into the Sn hinge. As shown in the in situ secondary ion beam microscopy images (Figure 3.6), a different folding time, meaning different energy, is required for a different hinge thickness to completely self-assemble with 90° folding angles. The different behaviors of the self-assembly process with respect to the 25, 35, and 45 nm Sn thicknesses were characterized and quantized (Figure 3.7). As shown in Figure 3.6, the thicker Sn hinges require a longer time than thinner hinges for self-assembly to fold up to the same angle (Figure 3.7a) because more energy should be applied to Sn hinges of greater mass in order to induce metal reflow. This result means that different folding angles could be achieved on a nanostructure under a one-time ion irradiation by designing hinges with different thicknesses. This makes it possible to fabricate 3D nanostructures with desired asymmetric parts, which can be used for developing applications in more advanced areas. In addition, the energy required for the structures to fold up from 30° to 60° is much less than that required to fold the structures from 60° to 90° (Figure 3.7b), leading to a decreasing trend in the angular speeds of each panel as the folding angle on the same sample increases (Figure 3.7c). This is due to the exposed area decreasing with a higher folding angle. With less of the Sn hinge being

exposed to ion irradiation, the energy transferred from ions to the hinge decreases, which causes the lower angular speed at higher folding angles.

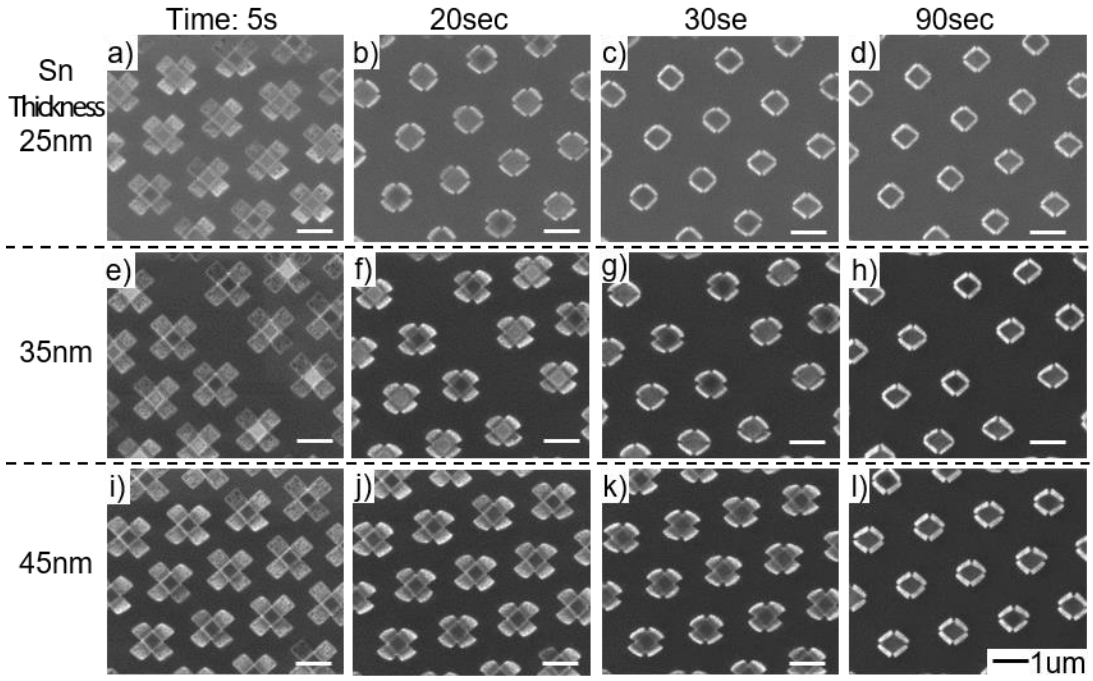

Figure 3.6 The effect of Sn hinge thickness on self-assembly process. The real-time ion beam microscopy images of samples with hinge of a-d) 25 nm, e-h) 35 nm, and i-l) 45 nm were captured after 5, 20, 30, and 90 seconds. The self-assembled process results in a 500 nm sized five-faced hollow cubic structure and the yield of the assembly is nearly 100 %. [111]

3.2.6 Modelling of the Self-Assembly Process

In order to achieve a better understanding of the self-folding process, a numerical modeling analysis was developed. During the self-assembly process, various forces, such as gravity, surface tension, and van der Waals forces, are applied on the nanostructures and need to be taken into consideration. Here, we use energy to show the combined effects of

all the applied forces rather than analyzing their effect separately. In the model, it is set that the same amount of energy, ΔE, is required for a hinge with unit mass, d_m, to fold up to unit angle, $d\theta$. The mass of the hinge is $\rho \cdot A_h \cdot L$, where ρ is the density of the hinge material, A_h is the area of the hinge, and L is the thickness of the hinge. Therefore, the total energy, E_{tot}, required for a hinge with mass m to fold up to a unit angle is $\Delta E \cdot \rho \cdot A_h \cdot L \cdot d\theta$ (Eq. 3.1). The energy (E_{tot}) is provided by the ion irradiation with ion projection power P in a unit time, dt. However, only the energy projected on the hinge area, $A_h \cdot cos\theta$ where θ is the folding angle, contributes to the folding performance, rather than the ions projected on the whole working area A_w. Thus, the total energy, E_{tot}, transferred to the hinge material in unit time is $\frac{k*P*dt*A_h*cos(\theta)}{A_w}$, where the constant k indicates the energy loss in the process (Eq. 1). By integrating time and angle during the whole process, a relationship between folding angle (θ) and time (t) can be achieved as shown in Eq.3.2. This equation describes the folding performance of the polyhedral nanostructures with respect to hinge thickness (L), and the modeling results from the equation show a very good agreement with experiment data (Figure 3.7a). Based on the modeling results shown in Fig. 4m, the required energy (Figure 3.7b) and the angular speed (Figure 3.7v) of each panel with different Sn hinge thicknesses were modeled as well. As shown in Figure 3.7, the model shows the same trend as the real folding process, which obviously supports the mechanism that the ion energy inducing heat energy is the key factor resulting in a self-assembly process in a focused ion beam microscopy system.

$$E_{tot} = \Delta \mathrm{E} \cdot \rho \cdot A_h \cdot L \cdot \mathrm{d}\theta = \frac{\mathrm{k} \cdot \mathrm{P} \cdot dt \cdot A_h \cdot \cos(\theta)}{A_w} \tag{3.1}$$

$$\mathrm{t} = \frac{A_w \cdot \Delta \mathrm{E} \cdot \rho \cdot L}{\mathrm{P} \cdot \mathrm{k}} \log(\tan(\theta) + \frac{1}{\cos(\theta)}) \tag{3.2}$$

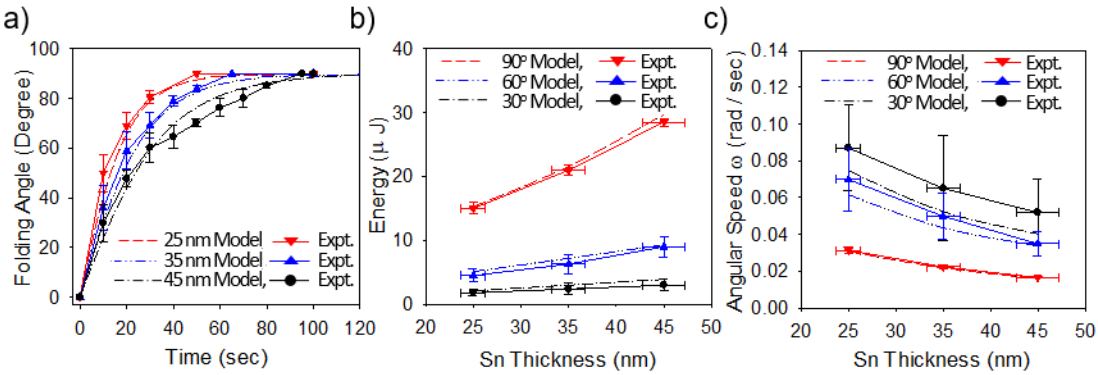

Figure 3.7 Analysis of the self-assembly process with different hinge thickness using measured and modelled data. a) The folding angles, b) applied energy, and c) angular speeds of each panel with different hinge thickness were measured and modeled. b) The energy and c) angular speed of the panels from beginning to 30°, 60°, and 90° folding angles are plotted based on the experimental and modeling results. [111]

3.2.7 Quick Summary

In Section 3.2, I introduced a precisely controllable in situ self-assembly technology using FIB, which can assemble 2D Sn hinged networks up into 3D nanostructures. The FIB is able to supply precisely controlled energy for triggering self-assembly as well as simultaneously offer visualization that can monitor the status of the nanoscale 3D self-assembly process. By monitoring the status of the self-assembly, the process time, along with the energy generated from the ion beam that feeds the self-assembly, can be dynamically controlled, which could significantly enhance the yield of the assembly process. With the help of the in situ self-assembly, a large-scale array (15 x 15 μm^2) of 500

nm sized 3D cubic structures was achieved with a yield of almost 100% with sub-10 nm scale precision.

3.3 Self-Assembly Using Polymer Hinges

3.3.1 Limitation of Metal Hinges

The aforementioned in situ monitored assembly demonstrates fabrication of 3D nanostructures with high yield, which significant push the limit of current techniques. However, it still remains challenging to explore the advance electronic or optical function of 3D nanostructures due to the disturbance induced by Sn hinge. For example, in the 3D micro-cube with resonator pattern, the metal hinge will also response to the electromagnetic wave and has it own resonance, which will couple with the resonators and disturb the resonant behavior of the entire devices [132]. Therefore, an alternative material, which does not disturb the performance of the devices, is required to be used as hinge. Polymer material stands out as a promising candidate due to its insulating properties and inert response to a wide frequency range of light [133].

3.3.2 Introduction to Polymer Reflow

Thermal reflow of polymers is a well-established process in microfabrication, which involves state change and mass transport [134-139]. Once the polymers are heated to their glass transition temperature, they experience a reduction in viscosity and an enhancement in fluidity, causing their structure to reshape to a state with minimum surface energy [140]. Even though thermal reflow can also be achieved in metals, normally metals

require more thermal energy, due to their higher melting point compared to polymers' glass transition temperature. In addition, oxide layers are easily formed on the surfaces of metal structures, which further increases the input energy needed to induce metal reflow, making it difficult to estimate the total thermal energy required for the process. Moreover, compared to metals, polymers exhibit numerous advantages in electronic and optical applications because of their insulating properties and inert response over a wide frequency range of electromagnetic waves [133], thereby causing less interference in the intended optical and electronic behaviors [132]. Due to these advantages, thermal reflow of polymers has been utilized for building diverse microstructures such as spherical or cylindrical optical lenses [136-139], optical ring resonators [134], and fluidic channels [135]. However, there is a substantial challenge in precisely controlling the extent of polymer reflow and achieving localized reflow, especially at nanoscale, using currently available heat sources such as hotplates [134-137], microwaves [141], and hot liquid baths [142], which supply thermal energy to the entire substrate (sample). Since the mass and volume of the substrate are usually much greater than that of the polymer-based nanostructure, the thermal energy stored in the substrate is much higher than the energy required for triggering nanoscale polymer reflow. As a result, it is difficult to achieve desired nanoscale polymer reflow by tuning the parameters of these macroscale heat sources, such as heating time, power, and temperature. Furthermore, the macroscale global heat sources apply the same amount of thermal energy to all the structures defined on the substrate rather than a specific amount of energy to desired locations. This results in uniform extents of polymer reflow, instead of diverse extents of reflow throughout the substrate according to different requirements. Moreover, the globally supplied thermal

energy can damage heat sensitive materials in the devices, leading to device failures, such as cracks in thin films induced by thermal expansion [143], and temperature denaturation or degradation of immobilized bio-components [144]. These limitations of macroscale global heat sources bring critical difficulties in utilizing diverse functions realized by precisely controlled, localized polymer reflow. In order to overcome the present challenges, localized rapid heating processes which can induce exact desired amounts of thermal energy in specific areas and locations with nanoscale precision are required.

3.3.3 The Concept of FIB Triggered Polymer Reflow

The concept behind polymer reflow is illustrated in Figure 3.8. In the FIB system (FEI Quanta 200 3D), liquid gallium (Ga) is in contact with a tungsten (W) needle, which wets the W tip and works as an ion source. Once a high extraction electric field is applied, Ga ions are emitted away from the tip due to the field ionization and post-ionization [126]. Because of the electric field in the FIB column, the emitted ions can be accelerated to a high kinetic energy and focused on polymer nanopillars consisting of PMMA defined on a Si substrate (N-type with phosphorous dopant, thickness of 525 ± 25 μm, and resistivity of 560 – 840 Ω·cm). The irradiated ions are bombarded onto the polymer nanopillars, imbedding into the polymer (Figure 3.8a). As a result of ion implantation, the kinetic energy of the ions is transformed into thermal energy and increases the temperature of the polymer (Figure 3.8a). With the accumulation of thermal energy, the temperature of the polymer exceeds its glass transition temperature and changes the phase of the polymer from solid to liquid, triggering a reflow process to minimize the surface area (Figure 3.8b-g).

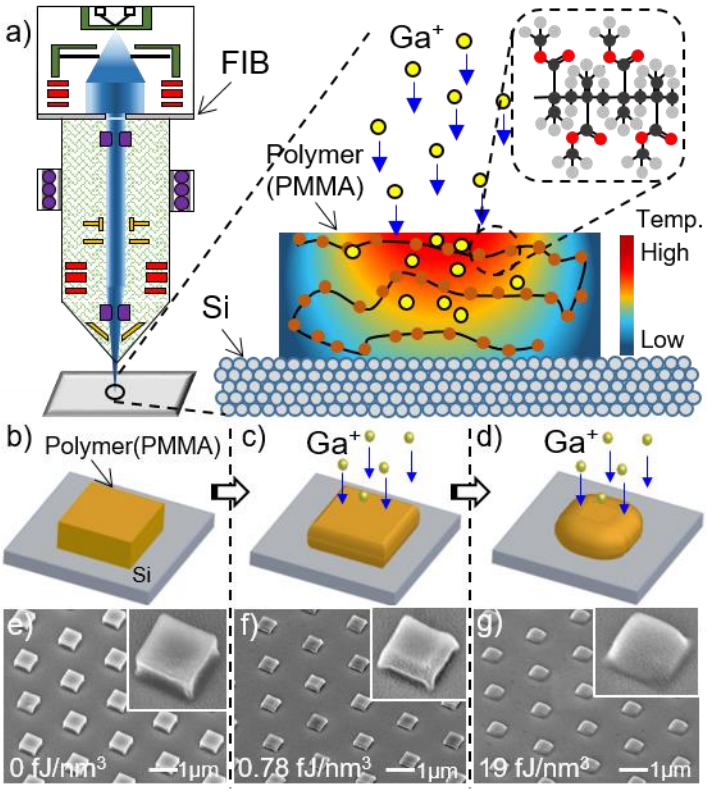

Figure 3.8 a) Conceptual schematics of localized heat generation and polymer reflow triggered in a focused ion beam (FIB) system. Once the Ga ions irradiate the surface of the polymer, kinetic energy is transformed into heat energy. b-d) schematics and e-g) SEM images showing the process of polymer (PMMA) reflow due to implantation of the Ga ions. The heat generated in PMMA melts the material and triggers reflow of the polymer. During this process, the square pillars with sharp boundaries become rounded to minimize the surface energy. [145]

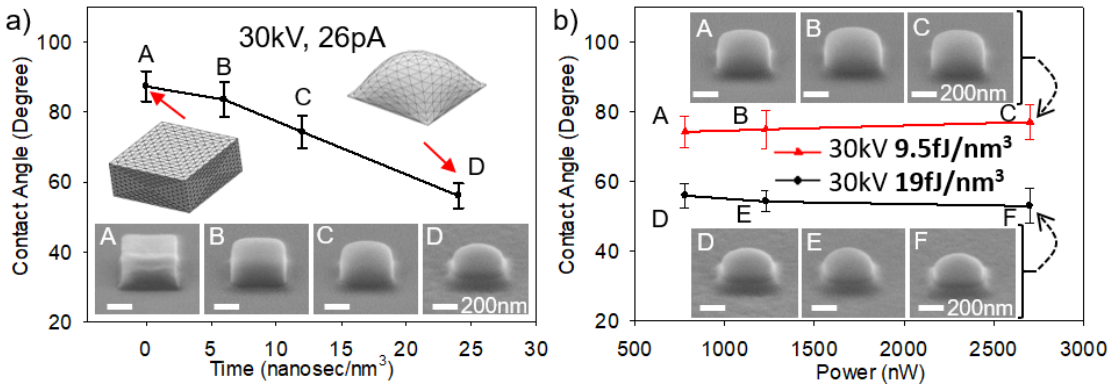

Figure 3.9 The measurement and simulation of contact angles with different ion irradiation parameters. a) The change in contact angle of a single PMMA pillar (500 nm × 500 nm × 300 nm) under ion irradiation at 30 kV and 26 pA for 0, 6, 12, and 24 nanosec/nm^3. The bottom insets show the cross-sectional view of the PMMA pillar at the data points. The upper insets show the simulation results for PMMA pillar before and after ion irradiation. b) The relationship between polymer reflow and ion irradiation power with a constant voltage (30 kV) and varying energy density (A-C: 9.5 fJ/nm^3; D-F: 19 fJ/nm^3), which shows that energy is the key factor in determining polymer reflow. The insets show the cross-sectional view of the PMMA pillar at the data points. [145]

To further understand the ion-polymer interaction, 500 nm × 500 nm × 300 nm PMMA nanopillars were formed on top of a Si wafer by an electron beam lithography (EBL) process (Figure 3.9). After applying ion irradiations with 30 kV bias voltages, 26 pA beam currents, and different irradiation times (0, 6, 12, and 24 nanosec/nm^3), the side views of the polymer nanopillars were captured for quantified characterization of contact angles. Because of the tilt angle limitations in scanning electron microscopes (SEM), the side images were captured at 60° tilt angle. Therefore, post data analysis, as described

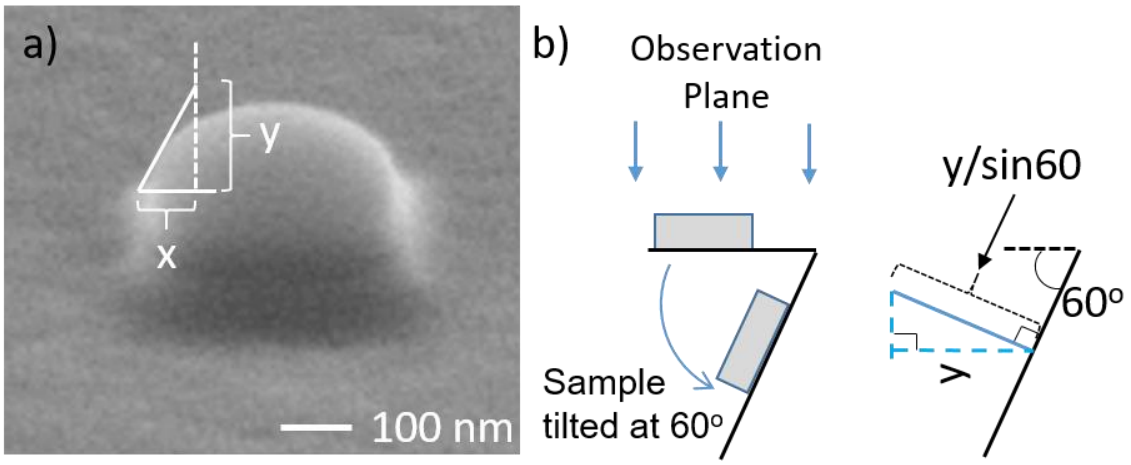

Figure 3.10, Illustration showing the measurement method of the contact angle. a) an outline for the angle is drawn based on the rare end of the pillar in the image capture with a 60° tilted angle. b) The height value was corrected based on the imaging setup. [145]

Figure 3.10, was required to get the contact angle. The contact angle decreases from 87° to 56° (Figure 3.9a), which shows the effect of irradiation time (energy) on the polymer reflow process. In addition, the contact angles of the reflowed nanopillars are similar to the results of the reflow process modeled by SurfaceEvolver (Version 2.70) (Figure 3.9a), which confirms the change in shape is mainly due to the reflow process. In order to investigate morphology changes in the nanopillars with respect to the irradiation power, ion streams with a 30 kV bias voltage and different currents (26, 41, and 90 pA), resulting in different irradiation power (780, 1230, and 2700 nW), were applied to the polymer nanopillars. For these tests, the irradiation times were tuned accordingly to maintain the same total ion energy dose (9.5 fJ/nm^3 or 19 fJ/nm^3 depending on the trial set) (Figure 3.9b). As shown in Figure 3.9b, similar reflow behaviors were observed based on the morphology of PMMA nanopillars under different powers of the incident ion beam. This result indicates the input

energy from the ion irradiation is much more significant than the heat dissipated from the nanopillars into the substrate and surrounding ambient environment. The heat dissipation

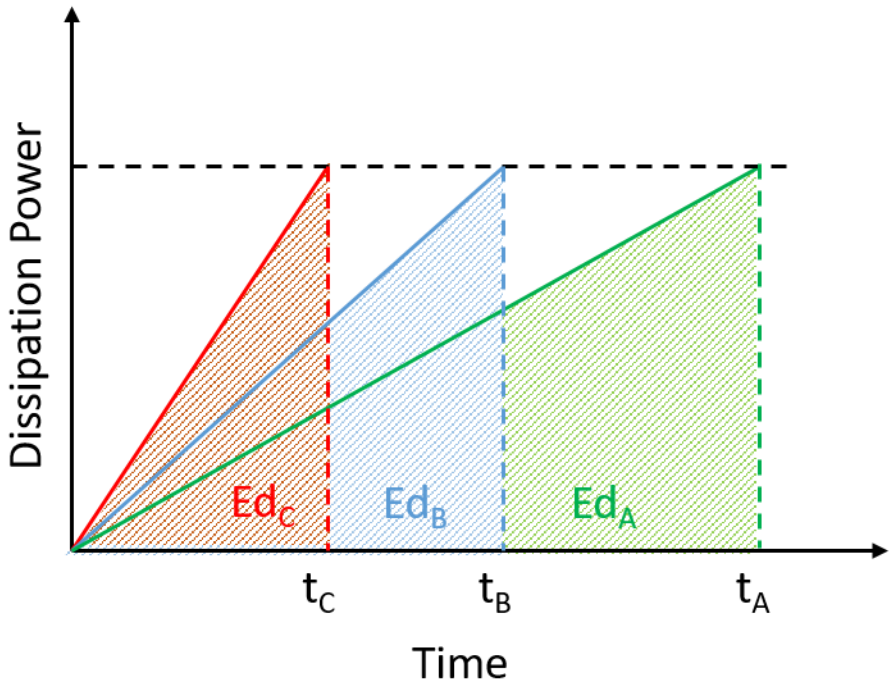

Figure 3.11. Qualitative plot of the heat dissipation power under ion irradiation of constant total energy but different powers. The enclosed areas are the total dissipation energies, which shows different input powers result in different total heat dissipation. [145]

power (P_D) is directly proportional to the ion irradiation power (P_I) based on an equation (3.5) derived in **Section 3.3.4**. When the irradiation power (P_I) increases with fixed irradiation energy input, the dissipation power (P_D) increases to a final constant value (proportional to the constant input energy from ion irradiation) at a higher rate, *i.e.* a shorter treatment time. Because of the same final constant value of dissipation power, shorter

treatment times are required at higher P_I; thus, the total energy dissipation (the enclosed area in Figure 3.11) decreases proportionally according to the increase of irradiation power. However, the fourfold difference in applied power for the control experiment (Figure 3.9b), leading to a fourfold difference in heat energy dissipation (Figure 3.11), is not sufficient to cause major changes in the morphology of the nanopillars.

3.3.4 Heat Dissipation Analysis

During the localized heating process under ion irradiation, heat dissipation is an inevitable process. The heat dissipation power (P_D) is determined by the temperature difference (ΔT) between the polymer nanopillar and substrate (T_P-T_S) and the thermal resistance θ, as shown in Equation (3.3).

$$P_D = \frac{T_P - T_S}{\theta} \tag{3.3}$$

The thermal resistance is a constant value for this system with unit of °C/W. In this system, the input heat (Q) is mainly from ion irradiation, which is expressed as $P_I \cdot t$, where P_I is the input power from ion irradiation and t is the irradiation time. Thus, the basic heat equation, $Q = c \cdot m \cdot \Delta T$, is rewritten as equation (3.4).

$$T_p - T_S = \frac{P_I \cdot t}{c \cdot m} \tag{3.4}$$

In this equation, c is the specific heat capacity of polmer with unit of J/g°C and m is the mass of the nanopillars with unit of g. Both of these two factors (c and m) are constant in this system. Then, from the (1) and (2), the power dissipation is expressed as equation (3.5), which is determined by the input power and time.

$$P_D = \frac{P_I \cdot t}{\theta \cdot c \cdot m} \tag{3.5}$$

As we applied different irradiation powers but the same total irradiation energy in the experiment shown in Figure 3.9b, the power dissipation in each case has different increasing rate but ends up with the constant final value. The relationship between heat dissipation power and irradiation time is qualitatively plotted in Figure 3.11. The enclosed area shown in Figure 3.11 is the total energy dissipation, which shows that variation in input power results in different total heat energy dissipation.

3.3.5 Thermal Reflow vs. Etching

In FIB systems, the irradiated ions bombarding the targeted material (polymer) cause reflow as well as inevitable etching of the material, resulting in a change to its morphology. The reflow is a thermal response to the ion induced localized heating while the etching is caused by the direct sputtering of PMMA chain fragment by the ion bombardment [146, 147]. To further understand the mechanism of the change in polymer morphology under ion irradiation, it is necessary to clarify the role of reflow and etching (sputtering). An array of smaller PMMA nanopillars (200 nm × 200 nm × 300 nm) was patterned and irradiated under an ion stream of 30 kV and 26 pA (Figure 3.12). Once the ion stream was applied to the nanopillars with a low energy density of 0.78 fJ/nm^3 (1.5 nanosec/nm^3), the kinetic energy was transformed into heat energy thereby raising the temperature of the polymer pillar above its glass transition temperature, which caused the sharp nanopillar edges (Figure 3.12a to become rounded (Figure 3.12b). Further irradiation (7.8 fJ/nm^3, 15 nanosec/nm^3) led to a higher level of reflow (Figure 3.12c). Due to the higher aspect ratio (height over width, r=1.5) (Figure 3.12) of these nanopillars *versus* that of the larger pillars (500 nm × 500 nm × 300 nm, r = 0.6) (Figure 3.9), the nanopillars

could not sustain their initial square shapes. The material started to flow away from the pillars and became a half hemisphere with larger base area (Figure 3.12c, d). Even though

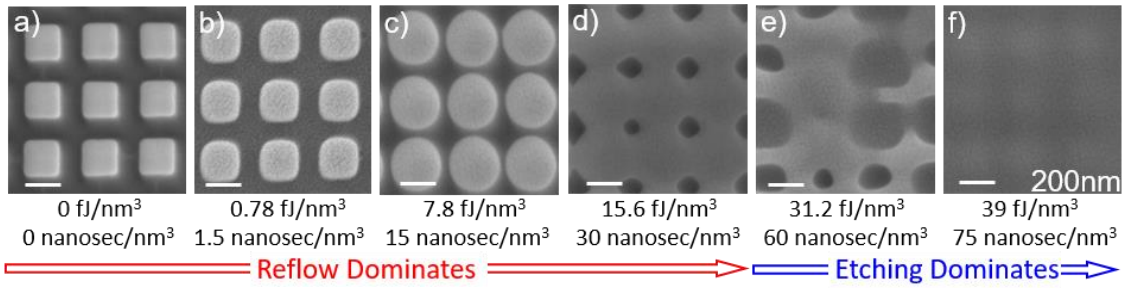

Figure 3.12 SEM images showing the change in shape in an array of PMMA pillars (200 nm × 200 nm × 300 nm) with 100 nm gaps under an ion irradiation of 30 kV and 26 pA. The shape transfromation demonstrate that both the reflow and etching process exist under ion irradiation. The scale bar is 200 nm. [145]

both reflow and sputtering existed during this process, the expansion of the pillar base areas could only be achieved by polymer reflow, which demonstrates reflow to be the dominant factor determining morphology during this period. When the pillars were completely reflowed and merged into one unit, becoming a thinner continuous layer (Figure 3.12d), application of a greater ion energy dose (> 31.2 fJ/nm^3) resulted in sputtering becoming the dominant effect influencing the morphology (Figure 3.12e). Further increasing the ion energy dose caused all the targeted polymer materials to be etched away (Figure 3.12f).

3.3.6 Localized Heating in FIB

Heat transfer under ion irradiation is a key component that needs to be characterized during this heating process, which is of great importance for evaluating the properties of localized heating and further achieving localized polymer reflow. First, polymer nanopillar (700 nm × 700 nm × 300 nm) arrays with different densities, 0.35 pillars/μm^2 (surface coverage: 17.3%) (Figure 3.13a, b) and 1.58 pillars/μm2 (surface coverage: 77.5%) (Figure 3.13c, d), were defined on Si substrates. The samples, including both nanopillars and substrates, were exposed to ion irradiation with the same energy (3×10-5 J) and exposed area (15 μm × 15 μm). Even though the polymer nanopillar arrays had around a fivefold difference in density, similar reflow performances were observed after ion irradiation (Figure 3.13b, d), which showed the thermal energy induced to the pillars was the main heat source for polymer reflow rather than the heat transferred from the surrounding Si substrate, implying the material reflow is a consequence of localized heating of the polymers exposed to the ions. The reason behind the localized heating is the heat generated inside the polymer nanopillars is mostly absorbed by the polymer material, indicated by H1 in Figure 3.14, contributing to polymer reflow. Only a small portion of the heat is dissipated to the substrate as indicated by H2 in Figure 3.14. In contrast, the heat generated near the surface of the surrounding Si substrate is mostly dissipated into the thick Si substrate, indicated by H3 in Figure 3.14, instead of transferring to the polymer pillars. This is because the temperature of the substrate is maintained constant at room temperature which is muchlower than the temperature of the nanopillars under ion irradiation. Therefore, the heat transferred from the surrounding substrate, indicated by H4 in Figure 3.14, can be

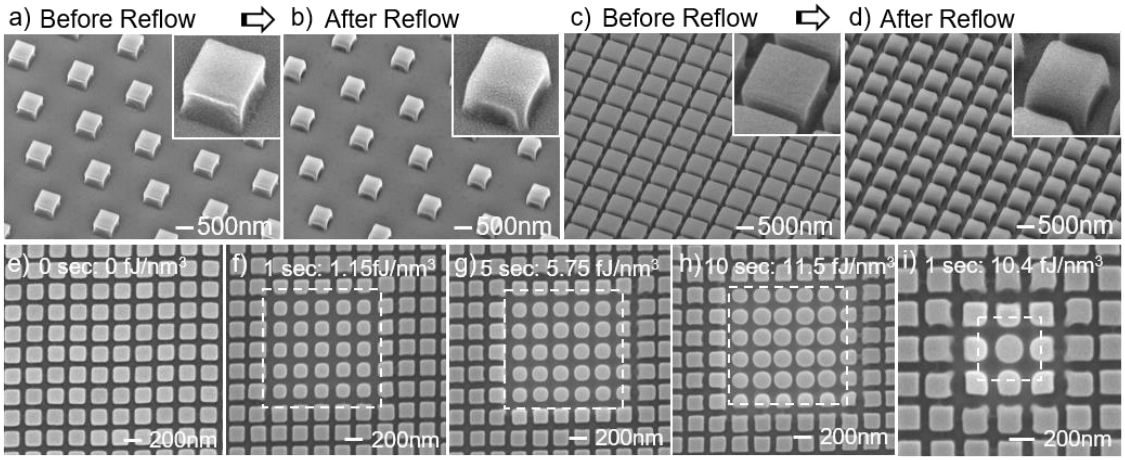

Figure 3.13 Analysis of the effect of heat transfer in the ion triggered polymer reflow process. a-d) The relationship between the heat transfer from the substrate and polymer reflow. a-b) shows the low density polymer pillar arrays a) before, and b) after ion irradiation. c-d) shows the high density polymer pillar arrays c) before, and d) after ion irradiation. Similar reflow levels are observed for the PMMA pillar arrays with different densities, which shows the heat transferred from the substrate is not a dominant factor. e-h) Characterization of the heat transfer distance. 1.5 μm × 1.5 μm PMMA pillar arrays are irradiated by an ion stream at 30 kV and 26 pA for e) 0 sec, f) 1 sec, g) 5 sec, and h) 10 sec. Even though significant polymer reflows are achieved under ion irradiation, only slight reflow performances can be observed on the surrounding unexposed pillars within nanometer scale distances, showing highly localized heating. i) With a reduced exposed area of 0.5 μm × 0.5 μm, single polymer pillar reflow is achieved under ion irradiation with 30 kV and 26 pA for 1 sec. [145]

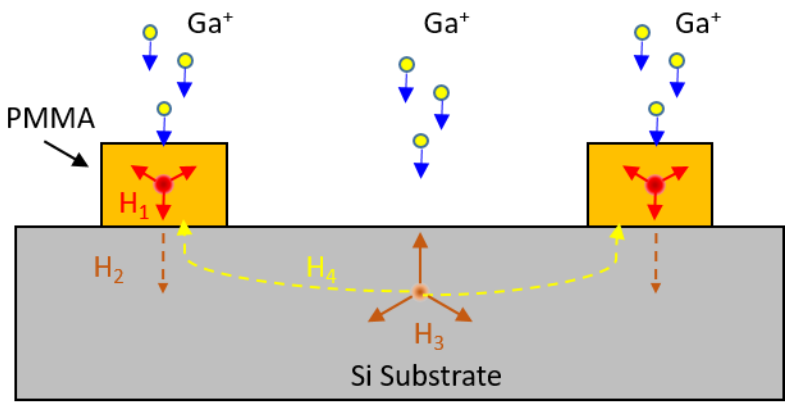

Figure 3.14. Conceptual schematic showing the heat generation, heat transfer, and heat dissipation in the PMMA nanopillars and Si substrate under ion irradiation. Once heat is generated in the PMMA pillars, most of the energy is absorbed by the polymer pillar (H_1) with minor dissipation to the Si substrate (H_2). For the heat generated in the Si substrate, most of the energy is dissipated to other areas of the Si (H_3) with a small portion delivered to the polymer pillars (H_4). [145]

ignored compared to the heat generated inside the polymer nanopillars (H_1). To further analyze the heat transfer performance under ion irradiation and demonstrate localized heating, densely packed polymer pillar arrays were selectively irradiated with three different total irradiation energies (Figure 3.13e-h). The exposed area was defined to be a 1.5 μm × 1.5 μm square using the patterning function in the FIB system. The morphology of the surrounding unexposed pillars was used to investigate the effect of heat transfer on polymer reflow. When a minor reflow was triggered with an ion energy dose of 1.15 fJ/nm^3 in the irradiated region as indicated by a dashed box in Figure 3.13f, insignificant morphology changes were observed in unexposed pillars within tens of nanometers from

the exposed region. Even when significant polymer reflow was triggered with an irradiation energy dose of 11.5 fJ/nm^3, which is ten times higher than the case shown in Figure 3.13f, the transferred heat energy induces polymer reflow only within a few hundreds of nanometers (Figure 3.13h) outside the exposed region. Ion irradiation with a smaller exposed area (500 nm × 500 nm) was also tested, which confirmed the localized heating of the polymer pillars. With the smaller exposed area, the polymer reflow behavior is confined to a single polymer pillar (Figure 3i), confirming the highly localized heating under ion irradiation.

3.3.7 Localized Polymer Reflow

The localized heating behavior of ion irradiation further enables the possibility to accurately deliver required heat energy to specific targets, achieving nanoscale localized polymer reflow. By tuning the ion irradiation energy and exposed location/area, diverse extents of polymer reflow of discrete and continuous designed patterns can be achieved. To demonstrate this ability, 300 nm thick PMMA nanostructures with different shapes such as square pillars, triangular pillars, ribbons, and rings were formed on top of a Si substrate using an EBL process (Figure 3.15). By controlling the exposed location/area, organized reflow patterns showing a periodic pattern (Figure 3.15a) and a non-periodic reflow forming a “UMN” pattern (Figure 3.15b) were realized on an array of discrete PMMA pillars. Because of the advantages of localized heating, morphologies representing reflow and no reflow could be achieved next to each other on a single substrate. Further control over the localized polymer reflow was investigated by varying the irradiation energy. A set of ion irradiations with energy densities of 0, 3.17, 6.34, and 9.5 fJ/nm^3 were applied to the

square pillars and different morphologies were observed in the pillars based on the incident energy density (Figure 3.15c). The sputtering under the low energy ion irradiation was not intense; thus, the polymer pillars remained similar in volume. Another set of ion irradiations with higher energies of 0, 4.7, 9.5, and 19 fJ/nm^3 were applied to the triangular pillars, resulting in more obvious differences in the polymer reflow (Figure 3.15d, e). Also, extreme sputtering was triggered under ion irradiation due to higher energy density, resulting in reduction in the volume of pillars. In both the cases, significantly different levels of reflow were realized among neighboring discrete pillars by tuning the applied ion irradiation energy, achieving multi-level reflow performance within a micro- or nanoscale area. In addition, due to the significantly localized heating behavior, multi-level localized polymer reflow could be achieved not only in discrete pillars (Figure 3.15c-e) but also in continuous structures (Figure 3.15f-h). To demonstrate this, nanoribbon and nanoring structures were partially exposed to ion irradiation with different energies (0Er, 1Er, and 2Er for ribbon and 0Ering, 1Ering, and 2Ering for ring) (Figure 3.15f-h). An obvious phase boundary between reflowed and non-reflowed polymer existed, showing a different degree of reflow was observed at the interface of exposed and unexposed areas, which clearly showed localized polymer reflow even in a continuous structure. After ion irradiation, a volume reduction was also observed in the polymer structures inevitably caused by the sputtering process. However, as we discussed earlier, the change in shape, such as rounded edges, is mainly induced by polymer reflow rather than sputtering.

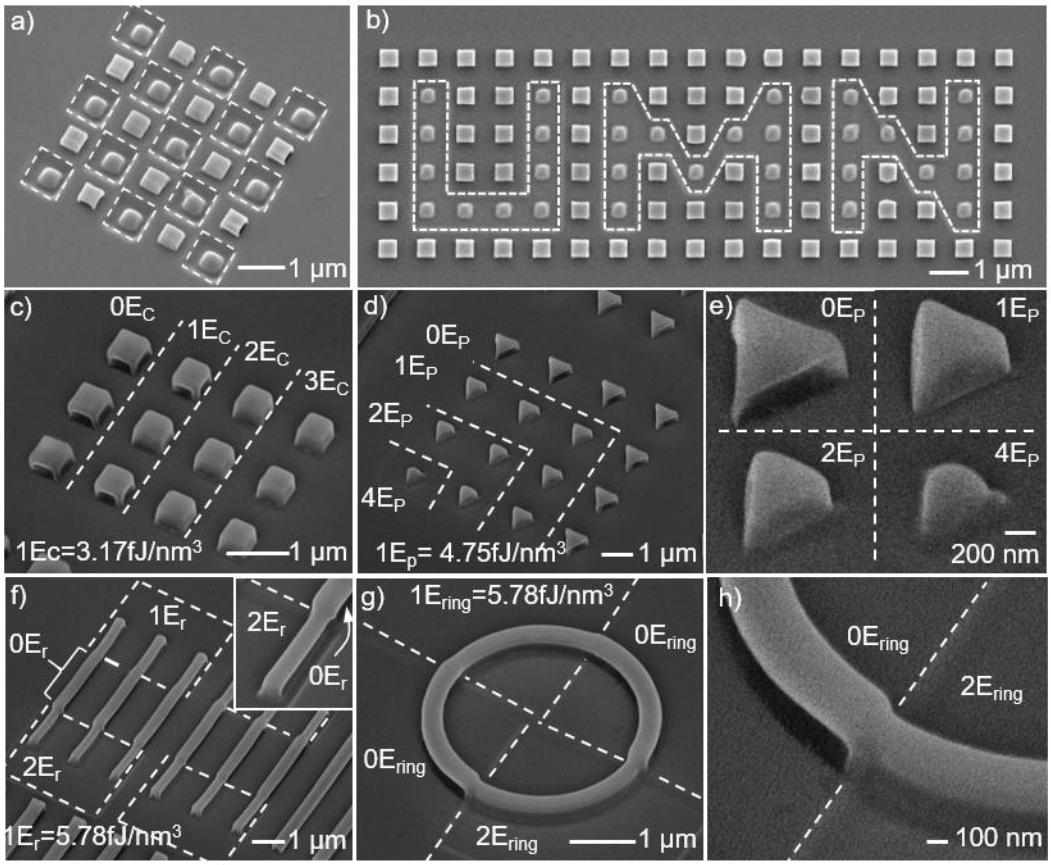

Figure 3.15 SEM images showing the localized polymer reflow achieved by the patterning function of a FIB system. Ordered reflow with the a) periodic pattern and b) "UMN" pattern is realized on an array of PMMA pillars. c-e) By controlling the irradiation energy, different reflow degrees can be defined in a densely patterned array. c) Lower and d) higher energy density are applied to the square, and triangular pillars, respectively. e) Zoomed-in image of the completely reflowed triangle pillars shown in d). f-h) The localized reflow process is also demonstrated in continuous structures such as PMMA f) ribbons and g) rings. The clear boundary between the exposed and unexposed regions confirms the ability to achieve localized heating. h) Zoomed-in image of the boundary achieved in the ring structure shown in g). [145]

3.3.8 Self-Assembly of 3D Nanostructure with Polymer Hinge

Besides the morphology of the polymer structures, surface energy also changes during the polymer reflow process, generating a surface tension force. This force is sufficient to lift nanoscale structures out of plane and achieve 3D self-assembly. 3D nanoscale cubic resonators were fabricated (Figure 3.16) to demonstrate this mechanism. The detailed fabrication process for the 2D nets (Figure 3.16a) is shown in Figure 3.17. Then, ion irradiation in the FIB microscope was used to trigger the self-assembly for 3D structures from the 2D nets (Figure 3.16a-c). When the hinge was exposed to ion irradiation (Figure 3.16b), the thermal energy transferred from the kinetic energy of the ions raised the temperature of the polymer hinges above its glass transition temperature and triggered polymer reflow (Figure 3.16d-f) and generated a surface tension force towards the center of the polymer hinges. The force folded the surrounding panels out of plane and achieved the desired 3D nanostructures (Figure 3.16a-c and g-i). Simultaneously, the scattered ions were captured for imaging, which made it possible for real-time monitoring of the status of self-assembly (Figure 3.16 g-i). By comparing the SEM images of the 2D panels before folding (Figure 3.16j, inset) and the 3D cubic structure after folding (Figure 3.16j), clear changes in the morphology of polymer hinges were observed, confirming polymer reflow as the mechanism for self-folding. In addition, the ability to perform real-time imaging made it possible to tune the irradiation energy and location according to the folding status, which leads to a highly controllable assembly process, resulting in an increased assembly yield. An array of 500 nm sized cubic SRRs with almost 100% yield were captured using a back scattered electron (BSE) microscope (JEOL 6500) (Figure 3.16k). The clear SRR

patterns demonstrated the successful protection of the sample during self-assembly (Figure 3.16).

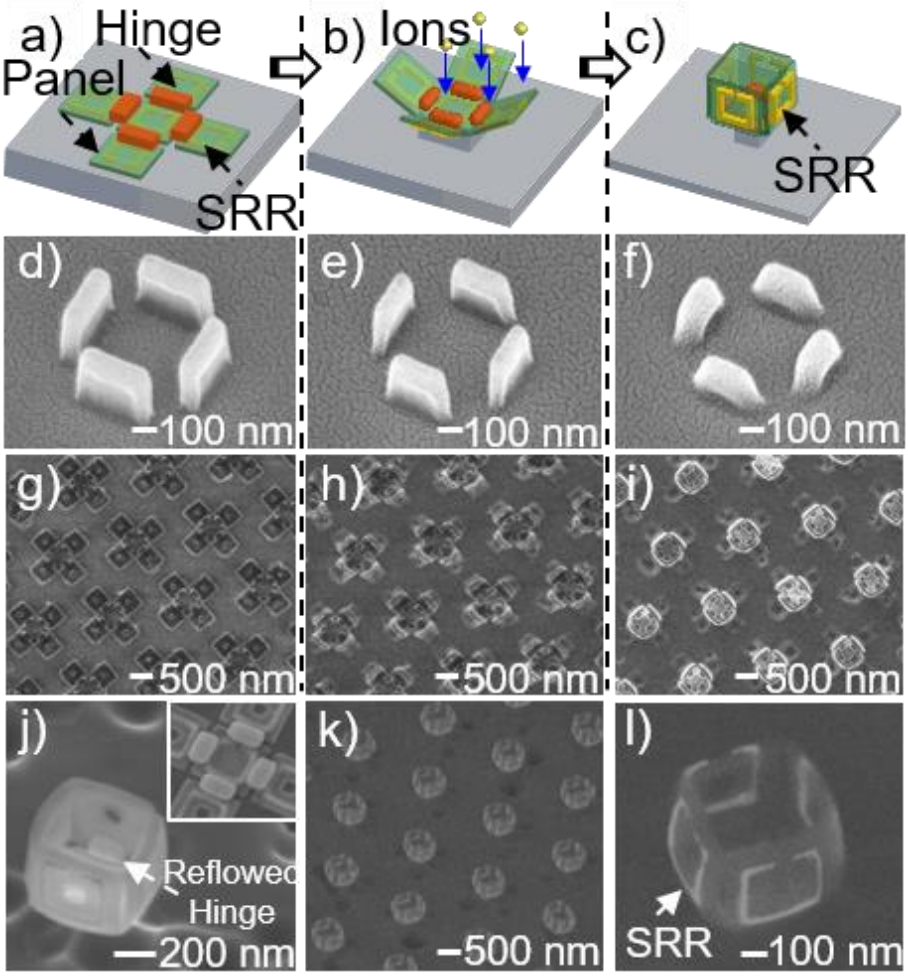

Figure 3.16. The self-assembly process for a 3D cubic resonator. a-c) Schematics of the self-assembly for a 3D cubic resonator. d-f) The morphology changes in the PMMA hinges under Ga ions at 30 kV and 10 pA. g-i) Images captured during the in situ monitored self-assembly process for 3D nanostructures in the FIB system at irradiation times of g) 0, h) 50, and i) 200 sec. j) SEM image of a fabricated 3D cubic split-ring resonator (SRR), which shows clear evidence of reflowed polymer hinges. The inset is the hinge before reflow. k-l), BSE image of an array of 3D cubic SRRs, showing successful protection of resonators. [145]

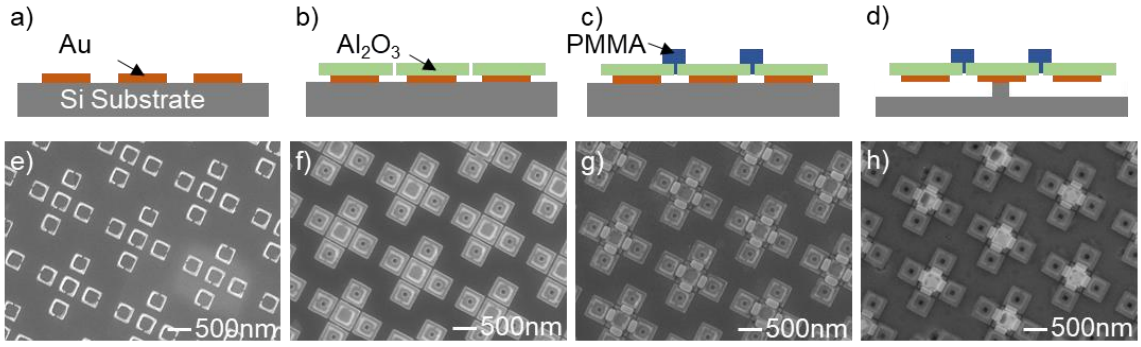

Figure 3.17 Schematics and SEM images showing the fabrication process for the 2D planar resonator structures before self-assembly. a, e), 50 nm Au resonators deposited on a Si substrate. b, f), 50 nm Al2O3 panels aligned and deposited on top of the Au resonators. c, g), 200 nm PMMA hinges defined between the panels. d, h), Release of the surrounding four panels by reactive ion etching. [145]

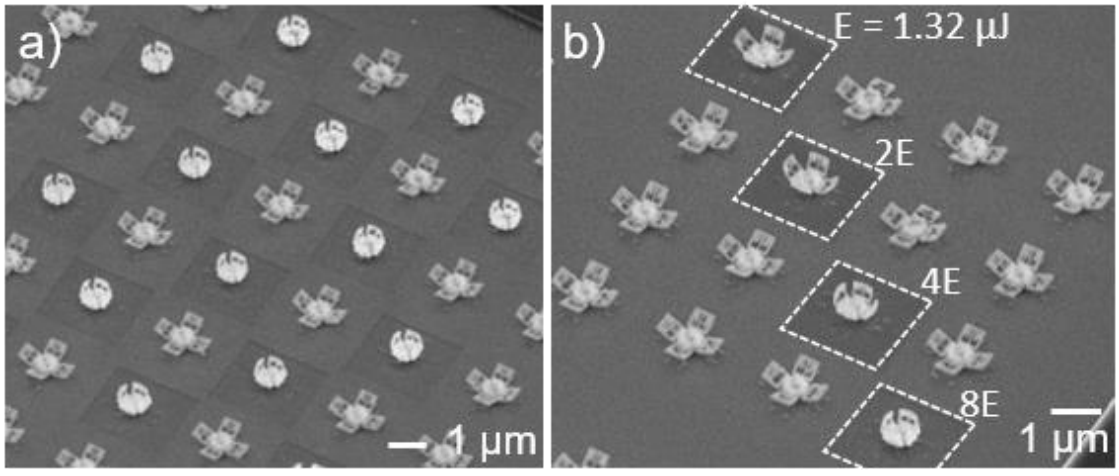

Figure 3.18 Programmable self-assembly by using the patterning function of FIB, a) achieving a periodic array of folded and unfolded structure and b) demonstrating different folding angle in the nearby structures. [145]

3.3.9 Localized Self-Assembly

The ability of FIB to deliver localized heating can be leveraged for programmable self-assembly through the patterning function in the FIB. Only the structures under ion irradiation were folded up while the unexposed structures remained their original shape. Thus, a periodic array of folded and unfolded 3D cube was obtained via selective ion irradiation (Figure 3.18a). A slight folding behavior was also observed for the unexposed structure due to inevitable ion exposure during alignment and imaging processes in the FIB system. A more advanced system with automatic alignment should be able to avoid this problem. Also, by tuning the irradiation energy (E, 2E, 4E, and 8E), different folding angles were demonstrated even in those structure with close proximity to each other (Figure 3.18b). It should be noted that programmable self-assembly process shown in the Figure 3.18 cannot be realized using traditional heat sources such as a hot plate or light supplying uniform heat energy on an entire substrate. Moreover, the real-time images captured during self-assembly offer a tool to characterize the folding process.

3.3.10 Modeling for Self-Assembly based on Polymer Hinge

The folding process was studied based on the measurement of folding angle *versus* the amount of time the hinges were exposed to Ga ions accelerated with a 30 kV bias voltage and a 10 pA beam current. As aforementioned in Section 3.2.6, we developed a theory for modeling the ion induced self-assembly using tin (Sn) metal hinges. Here, we revised the model to achieve more accurate numerical analysis by considering the hinge as two parts: one that is moving with the surrounding panels indicated by *A*, and another that is fixed on the central panel indicated by *B* in Figure 3.19a. In this model, the combined

effect of all the forces applied to the nanostructures, such as gravity, surface tension force, and van der Waals force, is shown as energy. The energy for a hinge with unit mass, *dm*, to fold the structure to a unit angle, $d\theta$, is assumed to be a constant value, ΔE. Because the mass of the hinge is calculated by the multiplication of the hinge density, ρ, and hinge volume ($A_h \cdot L$), where A_h is the area of the footprint of the hinge and L is the hinge thickness, the total energy for a hinge to fold the panel to a unit angle is $E_{tot} = \Delta E \cdot \rho \cdot A_h \cdot L \cdot d\theta$. As the ion irradiation is the only energy source for the whole system of self-assembly, the total energy required for folding is originally provided by the energy of irradiating ions, $P \cdot dt$, where P is the ion irradiation power and dt is the unit ion irradiation time. However, only the ions irradiated onto the hinge area, A_h, contribute towards polymer reflow rather than

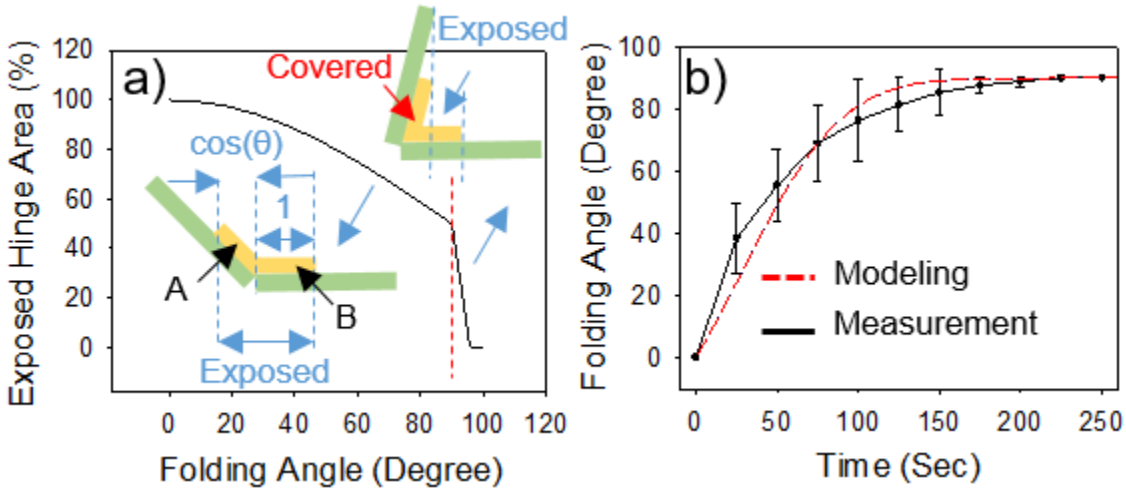

Figure 3.19 Analysis and modelling of the self-assembly process. a) Changes in the exposed hinge area with respect to different folding angles. Once folded greater than 90°, the panels will cover the hinges. b) Relationship between the folding angle and irradiation time based on measurement and simulation results, which show a strong agreement with each other. [145]

the overall ion irradiation projected onto the whole working area, A_w. Therefore, a coefficient $[A_h/2 + A_h \cdot \cos(\theta)/2]\,/A_w$ should be induced to define the effective ion irradiation energy, where $A_h/2$ is the area of the fixed hinge *B* in Figure 5o, $A_h \cdot \cos(\theta)/2$ is the exposed area of the moving hinge *A* in Figure 3.19a, and A_w is the overall working area irradiated under the ion stream. Also, a coefficient of *k* should be introduced in the equation for consideration of energy loss. Thus, the effective energy provided by ion irradiation for folding is $\frac{k \cdot P \cdot dt \cdot A_h \cdot [cos(\theta)+1]/2}{A_w}$. Based on this, the relationship between input energy from ion irradiation and required energy for folding is summarized as equation (3.6). By integrating both sides of the equation, the relationship between folding angle, θ, and ion irradiation time, *t*, is achieved as equation (3.7).

$$E_{tot} = \Delta E \cdot \rho \cdot A_h \cdot L \cdot d\theta = \frac{k \cdot P \cdot dt \cdot A_h \cdot [cos(\theta)+1]/2}{A_w} \qquad (\theta < 90°) \qquad (3.6)$$

$$t = \frac{2 \cdot A_w \cdot \Delta E \cdot \rho \cdot L}{P \cdot k} \left[\frac{1}{sin(\theta)} - \frac{1}{tan(\theta)}\right] \qquad (\theta < 90°) \qquad (3.7)$$

Equations (3.6) and (3.7) can only be used to model the folding process for angles smaller than 90°. Once the folding angle is more than 90°, the panels begin to cover the hinges and obstructing the exposure of the hinges to ion irradiation (Figure 3.19a). The moving hinge, indicated by *A* in Figure 3.19a, is immediately covered at folding angles greater than 90 degrees. Because the width of the panels is ten times that of the fixed hinge, indicated by *B* in Figure 3.19a, the fixed hinge *B* is also fully covered beyond a folding angle of 95°. When the hinges are completely covered, further ion irradiation does not induce heat in the hinge area, leading to a saturated folding angle (Figure 3.19b). The simulation result is plotted and shows the same trend as the measured folding angles (Figure 3.19b), which

supports our modeled structure with two hinges and a folding mechanism that only considers ions irradiated on the hinges as the energy source of self-folding. In addition, the saturation of the folding angle around 90° further demonstrates the localized heat generation in the PMMA hinge material rather than heat transfer from the Si substrate exposed to the ion beam as shown in Figure 3.15. The relationship between the folding behavior and structure design (material properties and structure dimension) modeled in the equations can work as a guide to predict the folding process. For example, if two polymers with similar properties but different glass transition temperature are used as hinge for folding same structures, the one with higher glass transition temperature probably requires more energy for folding, which is a larger ΔE. Thus, a longer folding time (t) is required for it to folding to the same angle.

3.3.11 Advantage of Polymer Hinge I: 3D Cubic SRR

Transforming 2D patterns into 3D nanostructures offers attractive possibilities for achieving unique optical and electrical properties, leading to the development of advanced plasmonic devices. However, metal hinges used in previous works create substantial limitations in the device performance. The conductivity and optical response of metal hinges induce a strong disturbance in the designed device functionality, leading to failure of the device. Compared to metal hinges, polymer hinges used in 3D nanoscale cubic resonators allow the possibility for building an all-dielectric 3D platform. Both the panels and hinges shown in Figure 3.16j-l are dielectric material except the split-ring resonators (SRRs) defined on each panel, which preserves the optical and electronic properties of the resonant structures built on them. A finite element modeling (FEM) simulation of the

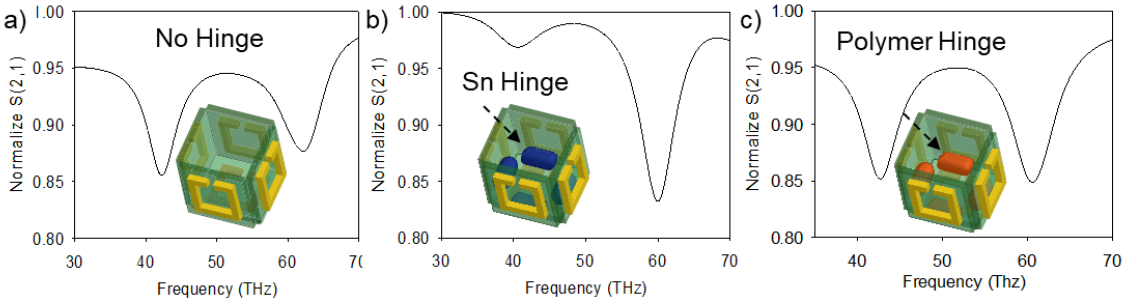

Figure 3.20. A finite element modeling (FEM) simulations showing the effect of hinge materials on the frequency spectrum of 3D cubic split-ring resonators (SRR). Transmission through a 3D resonator with a) no hinges, b) Sn hinges, and c) polymer hinges were simulated. [145].

resonance behavior of the SRRs was conducted through a high-frequency structural simulator (HFSS, version 13.0.1) to further develop an understanding of the effect of hinge materials. Transmission of THz electromagnetic waves through SRRs defined on a 3D nanocube with no hinges (Figure 3.20a), Sn hinges (Figure 3,20b), and polymer hinges (Figure 3.20c) was simulated. For cubic SRRs without any hinges, two clear resonance peaks with similar amplitude were seen at 42.2 and 62.2 THz (Figure 3.20a), corresponding to different 3D SRR resonance modes. Addition of Sn hinges between the panels induces coupling between the hinges and SRRs, which alters the characteristics of the original two peaks (Figure 3.20b). The amplitude of the first resonant peak was greatly reduced while the amplitude of the second peak was increased. In addition, as the Sn hinges experience metal reflow during the self-assembly process, it is difficult to control the overall resonance behavior of the 3D nanocubic resonator. As a result, it is not realistic to use metal hinges

for practical applications such as sensing. Unlike metal hinges, polymer hinges did not induce significant changes in the original resonance behavior of the SRRs (Figure 3.20c). The two peaks maintained a nearly constant resonant frequency and amplitude as compared to transmission response of SRRs without hinge structures, indicating the successful preservation of the optical properties of the device.

3.3.12 Advantage of Polymer Hinge II: 3D Graphene Plasmonic Cube

To further explore the advantages of self-assembly of 3D nanostructures triggered by polymer reflow, 3D graphene-based nanocubes were fabricated. Graphene has been widely investigated due to its advanced thermal, electrical, mechanical, and optical properties [148-151]. Recently, three-dimensional graphene-based structures have attracted tremendous attention due to their ability to further boost graphene's properties such as enhanced light confinement, magnetoresistance, and long wave propagation [69, 152, 153]. Various technologies have been developed to fabricate 3D graphene-based structures from a 2D planar layer [69, 154-159]. For example, 3D graphene micro-pillars and pyramids have been fabricated by directly transferring graphene onto micro-structured 3D surfaces [154-158]. Also, freestanding graphene-based microstructures have been achieved by self-folding *via* stress induced in a bilayer system or hinge material [69, 159]. However, all these graphene-based structures have dimensions in micro-scale and are difficult to be scaled down to nanoscale, which limits the advantages of 3D graphene-based structures due to the weak interaction between the graphene surfaces. Therefore, in this work the nanoscale self-assembly triggered by ion-induced polymer reflow was investigated to realize nanoscale 3D graphene-based structures.

3.3.12.1 Fabrication of the 3D Graphene-based Nanocube

To achieve self-assembly of 3D graphene-based nanocubes, a 2D nets of five face graphene-based structure is first fabricated through EBL and a graphene transfer process. A 2D net of five 10 nm thick Al_2O_3 panels was defined on top of a high resistivity Si substrate through a same EBL process as described above (Figure 3.21a, e). Each of the panels had dimensions of 500 nm × 500 nm and was separated from the central panel by a 50 nm gap. A single layer of CVD graphene was transferred on top of the Al_2O_3 panels through a wet graphene transfer process. Another layer of 50 nm thick Al_2O_3 panels, with the same dimensions as the first Al_2O_3 panels, were patterned on top of the graphene layer through an EBL process with precise alignment to the bottom Al_2O_3 layer (Figure 3.21b, f). The thickness of the second layer is designed to surpass the implantation range of the

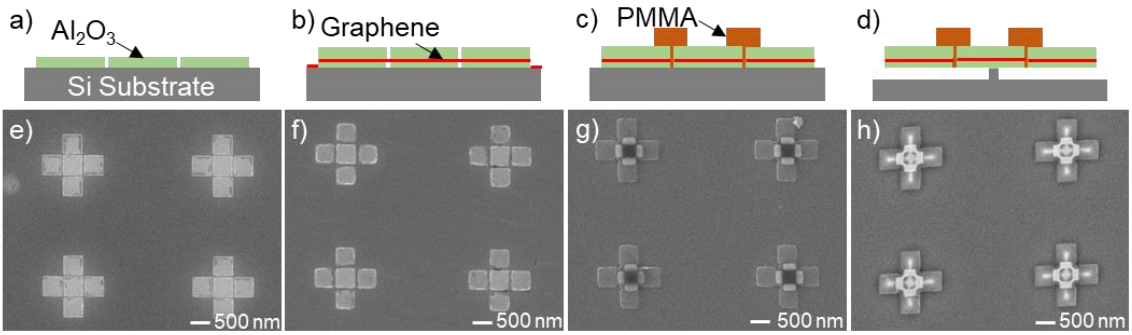

Figure 3.21. Schematics and SEM images showing the fabrication process of the 2D planar graphene-based nanostructures before self-assembly. a, e), 10 nm Al2O3 panels deposited on a Si substrate. b, f) A single layer of graphene is transferred on top of bottom Al2O3 panels followed by alignment and deposition of 50 nm Al2O3 panels. c, g), 200 nm thick PMMA hinges are defined between the panels. d, h), Release of the surrounding four panels through reactive ion etching. [145]

incident ions in Al_2O_3, ~ 30 nm for Ga ions with a 30 kV bias voltage (Figure 3.22), to protect the graphene from being damaged by the implanted ions. To remove the undesired graphene, an oxygen plasma etching process was carried out in a RIE system (Technics Micro-RIE Series 800) for 5 seconds with an oxygen (O2) flow rate of 10 sccm, pressure of 300 mTorr, and power of 30 W. Next, 200 nm thick PMMA was spun on top of the 2D panels. PMMA hinges, with dimensions of 150 nm × 350 nm, were defined through an EBL process (Figure 3.21c, g). After patterning the hinges, the sample was treated by carbon tetrafluoride/oxygen (CF_4 /O_2) plasma in a RIE system (STS 320) to remove the Si substrate underneath the four surrounding panels (Figure 3.21d,). During the 5-minute etching process, the flow rates of CF_4 and O2 are kept constant at 12 sccm and 1 sccm,

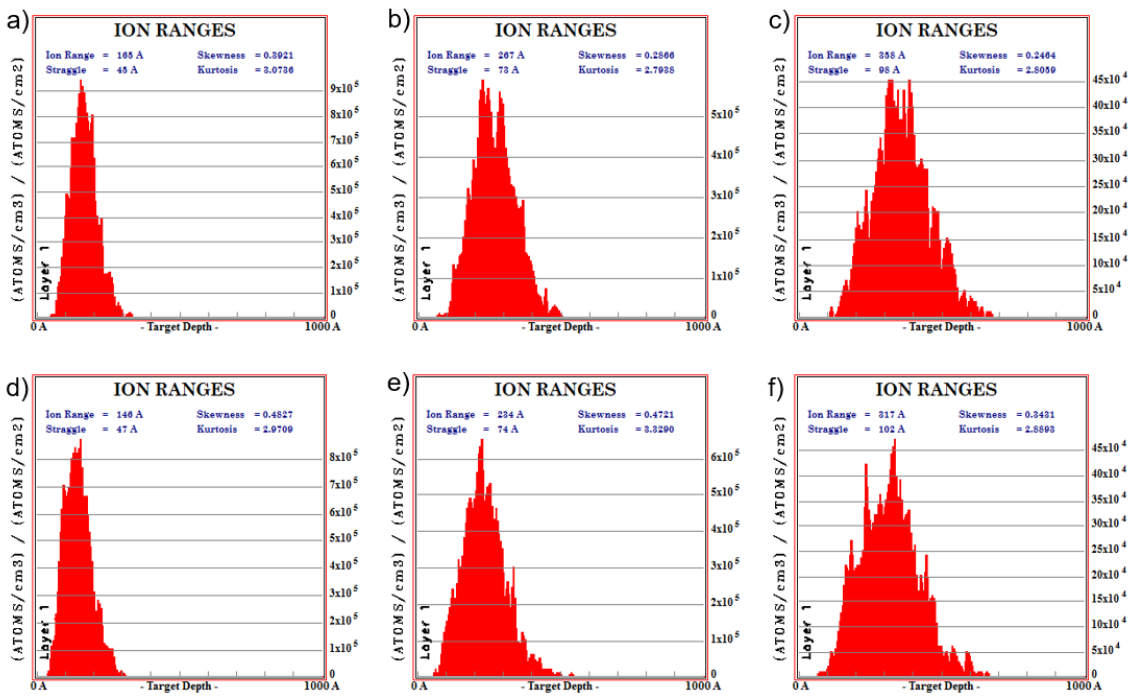

Figure 3.22, The implantation range of Ga ions with voltages of a) 10 kV, b) 20 kV, and c) 30 kV into PMMA, and the implantation range of Ga ion with voltages of d) 10 kV, e) 20 kV, and f) 30 kV into Al_2O_3. [145]

respectively, with a pressure of 100 mTorr and a power of 20 W. In order to protect the PMMA hinges from being etched away, the sample was placed facing down in the chamber, which minimizes etching from ion bombardment. To achieve the self-assembly of 3D structures, only the hinges in the sample were exposed to the ion irradiation with 30 kV bias voltage and 10 pA through the patterning function of a FIB system (FEI Quanta 200 3D) (Figure 3.23c, d).

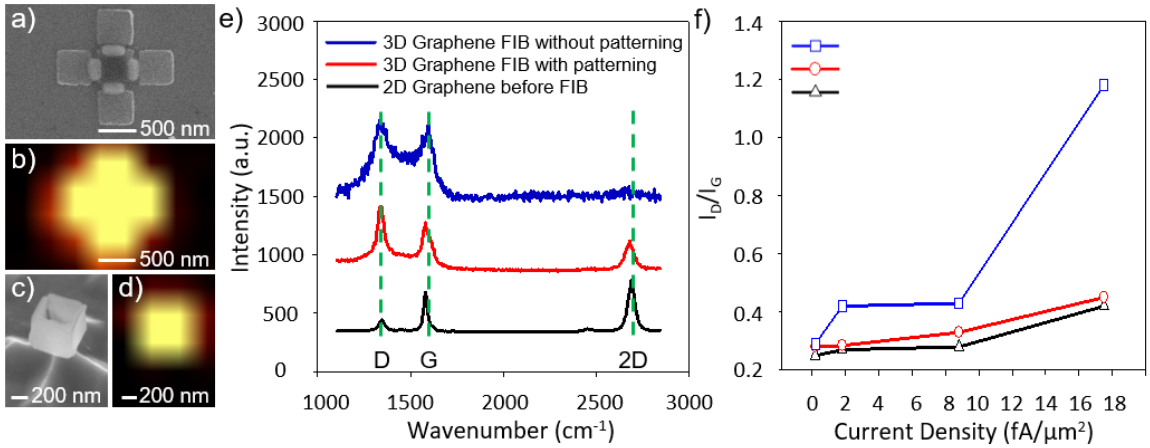

Figure 3.23 The SEM, Raman analysis, and field enhancement simulation of 3D graphene-based cubic structures. a-d) SEM, and Raman images of the nanocube a-b) before, and after c-d) assembly. e) Raman spectrum of the graphene in the nanostructures before, and after the ion-induced assembly. f) The effect of the Al_2O_3 protection layer thickness on the quality of graphene after ion irradiation at 30 kV and 3000 X magnification for 1 min in the FIB system. 145]

3.3.12.2 Protection of Graphene

A drawback of this process is the Ga ions imbedding into the panels can cause damage to the graphene layer. There exists a tremendous challenge in protecting graphene from ion irradiation. Even though most of the ions were imbedded in the 50 nm thick Al_2O_3 protection layer, a small amount of ion leakage into the graphene caused significant disorder [160,161], affecting its electrical and optical properties. To solve this problem, the programmable patterning function of the FIB system was used, which irradiates only the desired areas rather than the whole sample. Therefore, it was possible to expose only the hinge areas without any damage to the graphene panel under an ion stream for triggering polymer reflow. Through the programmable patterning function, the 2D panels (Figure 3.23a, b) were successfully folded into a 3D graphene-based nanocube (Figure 3.23c, d). The clear Raman mapping based on the 2D band (2690 cm^{-1}) graphene peak (Figure 3.23d) shows the same shape as the SEM image of the graphene cube (Figure 3.23c), demonstrating successful protection of graphene. The Raman spectrum of graphene before and after self-assembly provides more detailed information about changes in graphene during self-assembly (Figure 3.23e). Unlike the entirely exposed sample, which shows significantly broad graphene G (1580 cm^{-1}) and D (1350 cm^{-1}) bands and a missing 2D band (the blue curve in Figure 3.23e), both the G band and 2D band are preserved in the graphene cube self-assembled by the FIB patterning function (the red curve in Figure 3.23e). This result demonstrates the preservation of overall lattice structure. Even though the D band, which corresponds to disorders in graphene, shows higher amplitude after assembly, it can be attributed to the slight ion irradiation during the alignment process and

the stress induced during the self-assembly. The FIB alignment process was conducted for approximately 1 minute under a 30 kV ion beam with a 10 pA current at a magnification of 10000 X, resulting in a current density of 20 fA/μm^2. To address the effect of alignment process, graphene samples with 50, 100, and 150 nm Al_2O_3 protection layers were exposed for 1 minute under a 30 kV ion stream with different beam currents (1, 10, 50, and 100 pA) at a magnification of 3000 X, resulting in current densities of 0.18, 1.8, 8.8, and 17.5 fA/μm^2, respectively. As shown in Figure 3.23f, the ratio of the intensities of the D and G bands, I_D/I_G, which is a major factor in characterizing defects in graphene, is plotted using the data obtained from the Raman spectrum. The I_D/I_G values for all the test samples lie in the range of 0.2 to 1.2, which indicates the graphene is in the "low" defect density status [162], confirming no significant damage was induced in the graphene during the fabrication process including the self-assembly. Moreover, at a current density of 17.5 fA/μm^2, which is similar to the current density exposed during the alignment process, the I_D/I_G value of 1.2 is close to the data measured for a 3D graphene cube assembled with 50 nm thick panels and a patterning function (the red curve in Figure 3.23e), indicating the defects are mainly due to the alignment process. In addition, applying a thicker protection layer and lower ion density resulted in a reduction of the defects in the 3D graphene self-assembled with the FIB (Figure 3.23f).

3.3.12.3 Characterization of Plamsonic Behaviors

The plasmonic resonance in the 3D graphene-based nanocubes self-assembled by nanoscale polymer reflow was investigated using Comsol Multiphysics (ver. 5.2a) simulations. Graphene-based bio-chemical sensors increase photon absorption by targeted

specimens through plasmonic enhancement of the incident electric (E) field [163, 164], enabling detection and monitoring of chemical and biological species down to pM concentrations [165-167]. However, the limited surface area of the enhanced E-field presents a major drawback in the realization of single molecule sensors due to the time required for the diffusion of the targeted molecules to the regions of enhanced E-field [168]. Three-dimensional hollow graphene-based structures overcome this limitation through the creation of large area hotspots and volumetric field enhancement by 3D plasmon hybridization. For the 5-faced graphene cube without hinges, when the incident E-field is polarized along the bottom surface of the cube, a hotspot area of high field enhancement is created on the bottom face of the cube due to the uniform field interference from all four adjoining graphene faces (Figure 3.24a). On the other hand, when metallic hinges are used to build 3D graphene-based nanostructures, the coupling induced between the graphene plasmons and the conducting metallic hinges causes losses in the plasmonic behavior of graphene (Figure 3.24b). For 100 nm thick metallic aluminum (Al) hinges, the size (500 nm × 500 nm) of the large hotspot is reduced in area (300 nm ×300 nm), extending to only

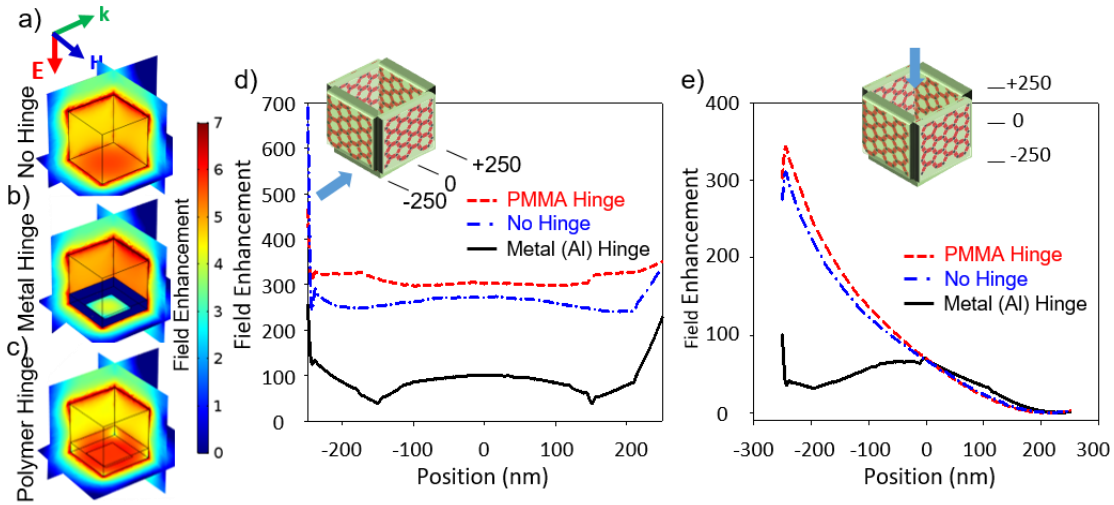

Figure 3.24 Analysis of the field enhancement in 3D graphene cubes with no hinges, metal (Al) hinges, and polymer (PMMA) hinges when the incident E-field is polarized towards the bottom surface of the cube with uniform coupling in all directions. a-c) Simulated field enhancement (log scale) on the surface of the cubic graphene containers with a) no hinges, b) metal hinges, and c) polymer hinges, which shows parasitic leeching of the hotspot surface by b) 100 nm metal hinges, while remaining undisturbed by c) 100 nm polymer hinges. d-e) Variations in the volumetric and surface enhanced fields for the cubic structures when, d) plotted along the bottom surface, and e) plotted at the center of the cubes along the direction of the incident E-field, as indicated by the blue arrow. [145]

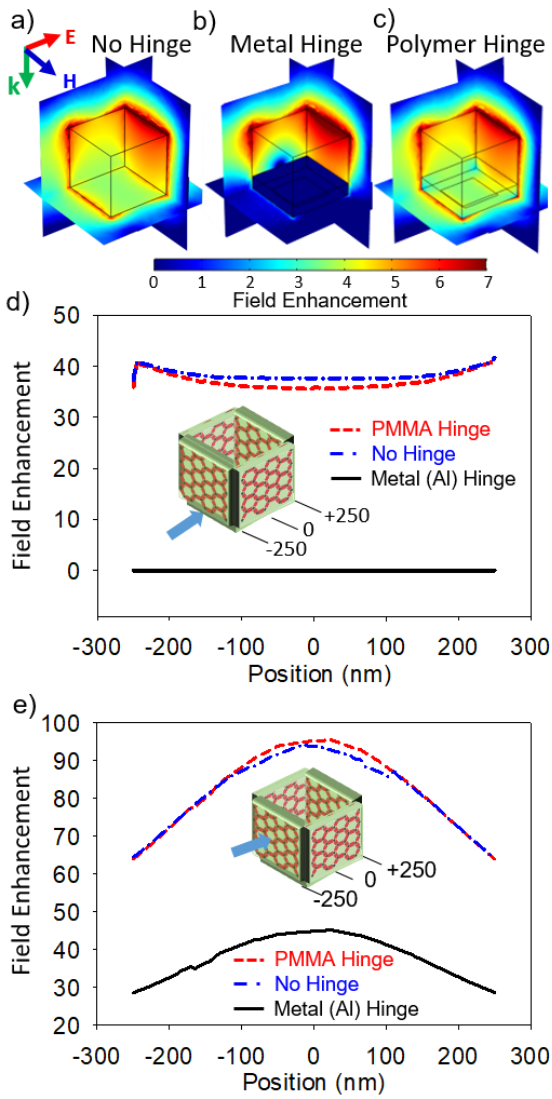

Figure 3.25. Analysis of the field enhancement in graphene cubes with no hinges, Al hinges, and PMMA hinges when the light is incident vertically from the top (open) surface of the cubes to the bottom surface. a-c) Normalized field enhancement (log scale) on the surface of the cubic graphene containers with a) no hinges, b) metal hinges, and c) polymer hinges, demonstrating the parasitic leeching by the metal hinges deposited on any graphene surface even in the absence of the hotspot. Variation in the field enhancement when, d) plotted along the bottom surface, and e) plotted along the direction of the incident E-field, as indicated by the blue arrow. [145]

those regions not covered by the metallic hinges (Figure 3.24b, as well as reduced in intensity by a factor of 3 (from 300, blue line, down to 100, black line, for a 500 nm length cube, Figure 3.24d). Thus, the bottom hotspot surface of the graphene cube with an overall near-field enhancement of 263 in the absence of hinges is reduced to 34 when metal hinges are present (Figure 3.24d). In contrast, when the nanocubes are realized using polymer hinges instead of metallic ones, the simulated results reveal the bottom surface of the cube retains the uniform circular hotspot of large near-field enhancement like the hotspot generated in the cube without hinges (Figure 3.24c). The hotspot surface on the bottom face of the polymer hinged cube demonstrates a nearly uniform enhancement of ~311 (Figure 3.24d, red line) with a minor increase as compared to a cube with no hinges (Figure 3.24d, blue line), which can be attributed to using the same mesh element size in the finite element modelling of hinges with different refractive index (air space=1, PMMA=1.5) that modifies the wavelength of the incident light in the PMMA medium. The strong fields existing on the surfaces of the graphene create a strong volumetric field within the bound volume of the cube (Figure 3.24e, blue line), allowing it to be used as a smart container for increased sensitivity. In the presence of metal hinges the lack of a hotspot reduces the field at the surfaces of the graphene cube and consequently the volumetric field is scattered from the surfaces of the cube (Figure 3.24e, a black line). Similar drawbacks due to the metal hinge are also observed under different polarizations of incident light, resulting in a reduced volumetric field enhancement (Figure 3.25). In addition, the graphene container with polymer hinges experiences a minute shift in resonant frequency as opposed to large shifts experience by structures with metal hinges (Figure 3.26). However, in the presence of polymer hinges a strong volumetric field is seen that decays when approaching the

unbound surface (top face) of the cube (Figure 3.24e, red line). The smaller shift in frequency is a major advantage for molecular sensing applications since the operating resonant frequency of the graphene containers needs to be controlled based on the vibration frequency of the targeted molecules and should be minimally affected by components constituting the plasmonic nanosensors. For a polymer hinge cube, the only factor affecting the resonant frequency is the size of the cube, thus, requiring only one parameter for the design of plasmonic nanosensors with desired operating frequency. Thus, significant design convenience and accuracy are achieved compared to metal hinged cubes where the combined effect of the cube size and hinge overlap and morphology needs to be analyzed.

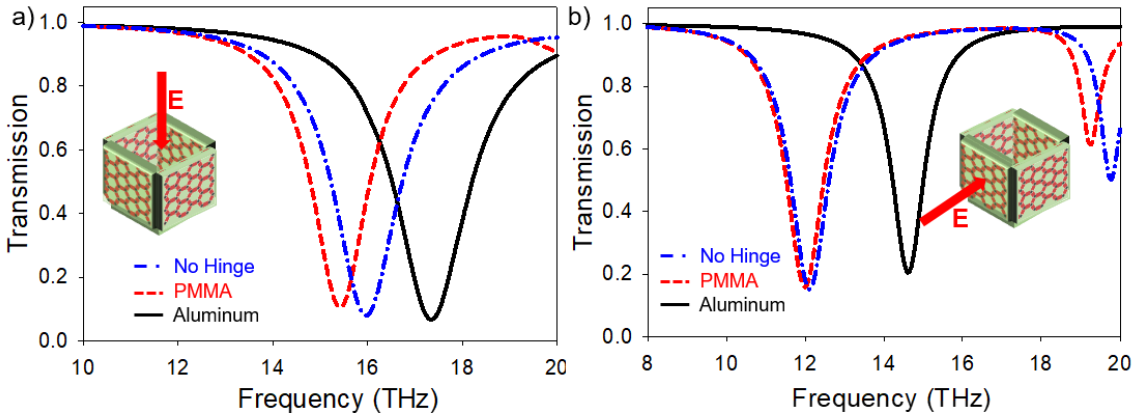

Figure 3.26. Transmission response for the 5-faced cube with no hinge, 100nm polymer (PMMA) hinge, and 100nm metallic (Aluminum) hinge with the incident E-field polarized a) from the top of graphene cube to the bottom, and b) from left side of the graphene cube to the right, as indicated by the red arrow. [145]

3.3.13 Quick Summary

In this section, I introduced a nanoscale polymer reflow process utilizing localized heat generation induced by an ion beam in a FIB microscope. The ion irradiation with nanoscale precision allows the precise control of the extent and location of heat generation, which enables programmable multi-level polymer reflow in continuous and discrete nanoscale polymer structures. Moreover, the surface tension force induced during the nanoscale polymer reflow can be utilized to trigger self-assembly of 3D nanostructures. The 3D polymer-hinged nanostructures are free from parasitic coupling that can exist between optoelectronic devices fabricated on these structures and the charge carriers in similarly formed structures with metallic hinge materials. This enables the polymer-hinged 3D nanostructures to be utilized for achieving 3D optical properties without suffering severe drawbacks from losses in frequency spectrum and decay of the superior volumetric/large surface area enhancement of the incident E-field. The enhanced properties and advantages exhibited by 3D metamaterials self-assembled using nanoscale polymer reflow can open pathways for applications in nanoscale 3D optoelectronic devices, resonator-based 3D sensors, and other 3D plasmonic devices.

Chapter4

Electron Irradiation Triggered Sequential and Reversible Self-Assembly

In this chapter, I introduce a novel electron irradiation triggered self-assembly process. The stress generation mechanisms, irradiation induced amourphous material crystallization and organic material degradation, are discussed in detail. The folding mechanics is investigated by both measurement and modelling. I also present the strategy to achieve sequential and reversible assembly using electron irradiations. Some prototypes of nanootpics and nanomechanics are demonstrated using this technique.

4.1 Electron Irradiation Triggered Sequential Self-Assembly

4.1.1 Importance of Sequence in Origami Like Self-Assembly

Origami- and kirigami-inspired assembly of 3D (three-dimensional) structures has arisen to be a broad topic in the past two decades [21, 69, 71, 77, 120, 132, 169-188]. To realize 3D structures from 2D (two-dimensional) nets, nanoscale folding and curving (spontaneous assembly) processes have been applied *via* a force generated by various stimuli. In Chapter 2 and 3, I studied the assembly process based on RIE and FIB system, which dramatically improved the fabrication yield. However, it is still a great challenge to

build complex 3D nanostructures with overlap, intersection, and asymmetry because one key factor of self-assembly is missing, namely programmable sequence. Sequence brings an additional dimension, time, to 3D self-assembly, which allows better control of the interactions, such as moving pathway and relative positions, of structures in a complex, assembled 3D system. By assigning each single assembly step in an established order (i.e., a sequential, programmable self-assembly), localized motion can be selectively triggered with precise timing, making a component accurately integrate into a complex structure without disturbing other parts of the assembly processes. Recently, several attempts to achieve sequential self-folding have been developed based on selective responsive material [189, 190] or localized stimuli such as a micro-heater [191] or laser source [192]. However, the responsive material and stimuli used in these methods are restricted to large-scale [189-192], and this size limitation makes it impossible to apply sequential self-assembly for the realization of complex 3D nanostructures.

In this section. I introduce a sequential, programmable self-assembly methodology that offers the capability to program the location, pattern, and energy of electron beam (e-beam) through the use of programmable e-beam scanning, thereby allowing control of the desired order for sequential self-assembly (Figure 1). This assembly approach also allows overlap, intersection, and asymmetry in assembly processes for building complex 3D nanostructures using the e-beam as a localized stimulus, which mimics origami and kirigami in nanoscale. Various complex 3D structures, specifically, a knot, latch, wrinkle, helix, butterfly, crane, and flower ring, are shown here as a proof of concept of sequential self-assembly in nanoscale.

4.1.2 Concept of Electron Irradiation Triggered Self-Assembly

To realize sequential self-assembly, we use an e-beam in a scanning electron microscope (SEM) as an energy source for triggering deformation of nanostructures. A SEM offers nanoscale, localized e-beam irradiation with precisely controllable beam-position and real-time images showing the current status of assembly, leading to an in situ monitored self-assembly process (Figure 4.1a) [79,82,83,111,123,145,186,193]. The combination of programmable e-beam irradiation and real-time imaging capability in a SEM mimics the functions of "hands" and "eyes" of a human being for doing paper origami, which significantly enhances the controllability of assembly. Stress is induced in released bilayers (chromium, Cr / aluminum oxide, Al2O3) as a result of volume changes in the Al2O3 layer caused by outgassing and atom rearrangement during crystallization when localized heat generated by the e-beam irradiation is applied (Figure 4.1b). The stress induced on the specific area deforms the freestanding thin films. As localized stimuli are applied to targeted areas with a desired order, sequential self-assembly is achieved while being simultaneously monitored. (Figure 4.1a). As a proof of concept, three different e-beam sequences are demonstrated constituting programmable nano-weaving processes that involve high time and space complexity (Figure 4.1c). By tuning the weaving sequence, four different knots with different internal spatial relations are demonstrated.

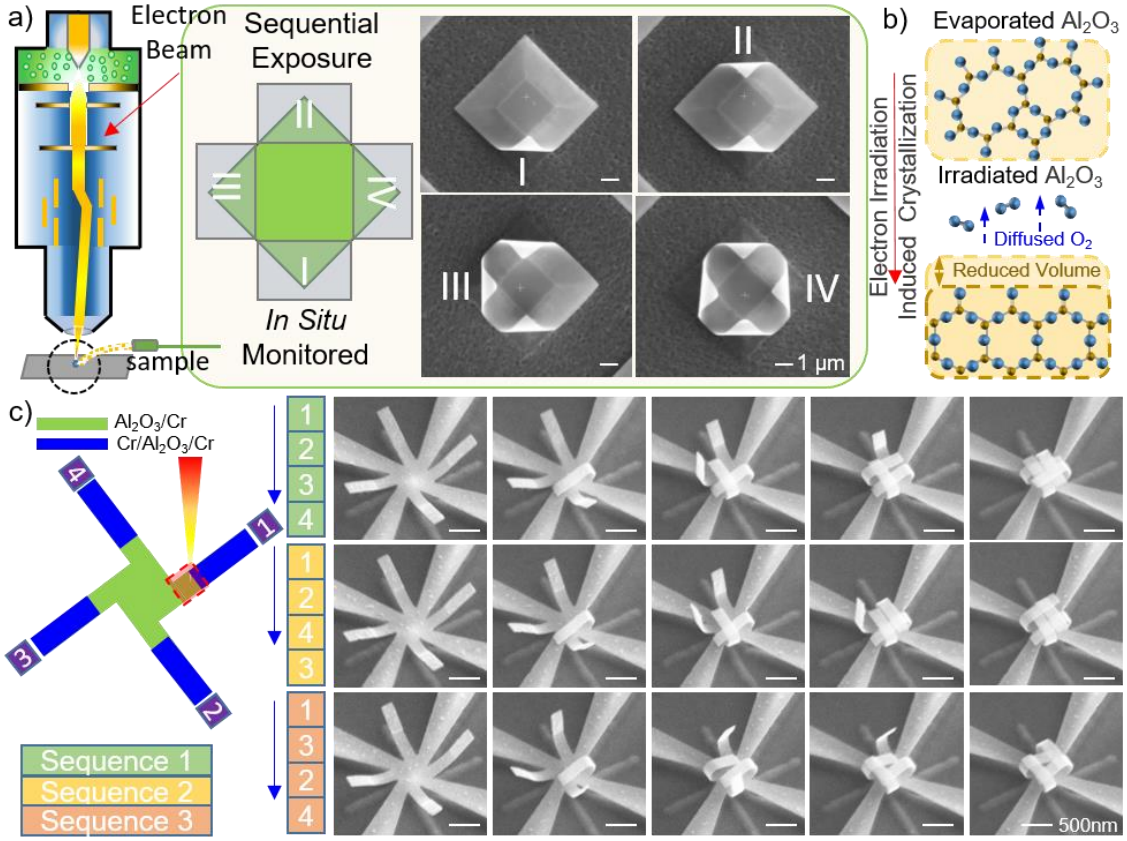

Figure 4.1 Conceptual schematics and SEM images showing the nano-weaving process triggered by electron irradiation induced crystallization. a) Instrument setup of electron irradiation induced crystallization for programmable self-assembly. b) Schematic showing the mechanism of electron induced crystallization. c) Programmable weaving of nanoknots achieved by sequentially irradiating the thin films by electron beam. The four beams of the 2D pattern (labeled as "1", "2", "3", and "4") can be irradiated in different orders for sequential self-folding. Three different irradiation sequences have been demonstrated ("1234", "1243", and "1324"), resulting in different assembly outcomes.

4.1.3 Electron Irradiation Triggered Crystallization

To induce localized stress caused by volume shrinkage of Al_2O_3 films deposited by an e-beam evaporator, phase change (crystallization) associated with extra oxygen outgassing and atomic rearrangement is triggered in the film using e-beam radiation, and the resultant stress curves the thin film. First, transmission electron microscopy (TEM) characterization is carried out on a partially curved tubular structure (30 nm Al_2O_3 and 3 nm Cr) for studying the phase change of Al_2O_3 (Figure 4.2a). The partially curved tube is embedded in platinum (Pt) and then cut out from the original sample using ion milling (Figure 4.3) to get cross-sectional TEM images and an energy dispersive spectroscopy (EDS) mapping (Figure 4.4). The pristine condition of the Al_2O_3 layer before self-curving (e-beam radiation) is amorphous; however, in the curved regime of the Al_2O_3 tube after self-curving, the contrast representing crystallization of Al_2O_3 varies significantly near the inside, especially from the surface to the depth of 10 nm (Figure 4.2b). This demonstrates the nanocrystallites (NCs) nucleate, grow in the near-surface regions of the Al2O3, and propagate into the amorphous Al2O3 layer while under e-beam exposure. The nanocrystallites are also confirmed by selected area electron diffraction (SAED) of the curved tube outlined in the dashed square in Figure 4.2a (Figure 4.2c inset). The high resolution TEM image (Figure 4.2c) and its fast Fourier transform analysis (Figure 2d,e) show irradiation results in crystallization of the amorphous-Al2O3 matrix, in which randomly oriented nanocrystallites (α-Al2O3) are formed. To confirm e-beam triggered crystallization, the amorphous-Al2O3 region is irradiated by a high voltage e-beam (300 kV) for 10s, which provides continuous driving force to form the nanocrystallites. As a result, the central area of approximately 10 nm in diameter is completely transformed from

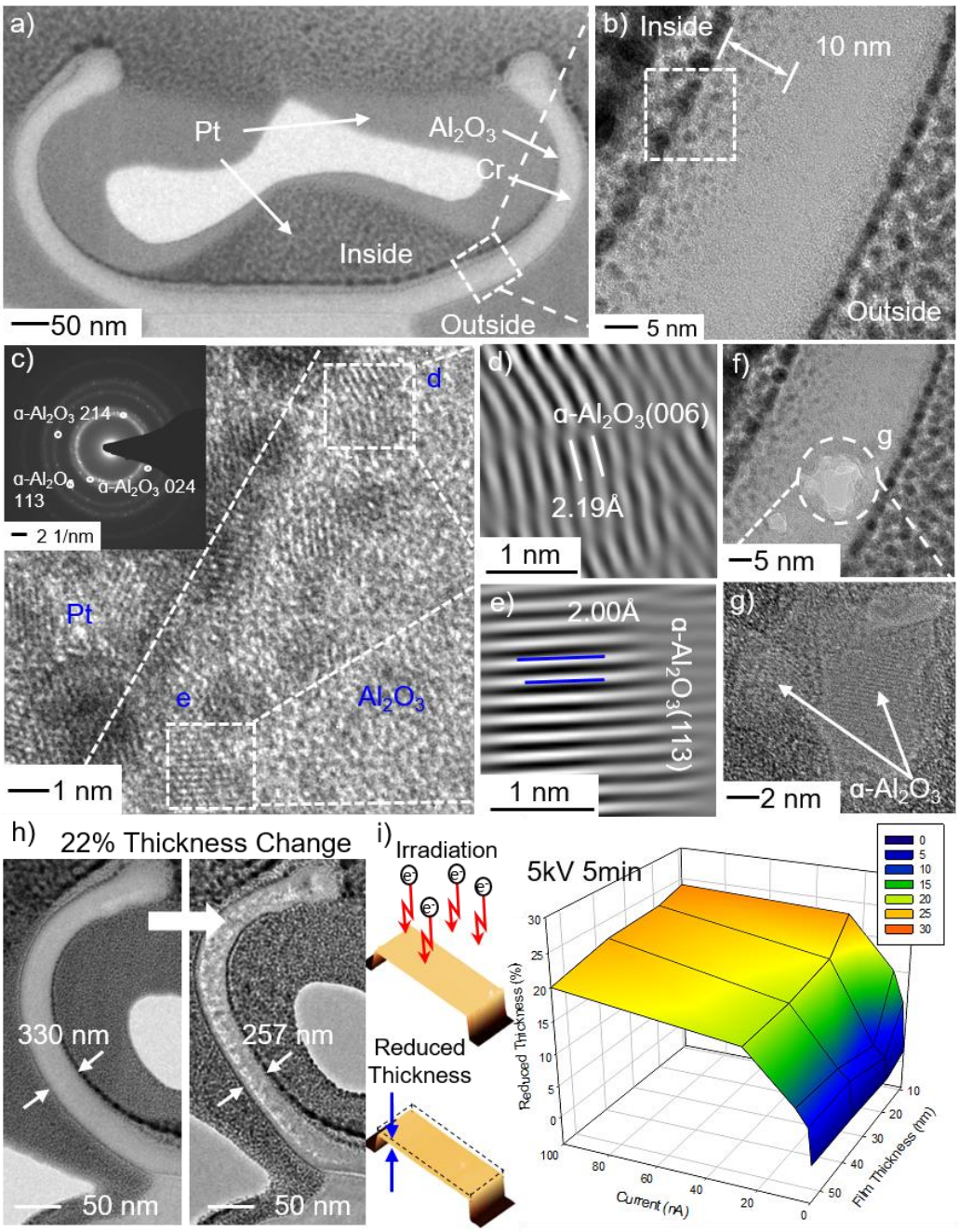

Figure 4.2 TEM and AFM analysis of the electron irradiation induced material change. a) TEM sample of a partially curved tube structures prepared by FIB. b) TEM image of the analyzed area of the tube structures. c) HRTEM image of the surface of the tube structure, indicating the electron irradiation induced Al_2O_3 nanocrystals. The inset is the selected area electron diffraction (SAED) analysis of the partially curved tube. d-e) Fourier

transformation analysis of the nucleated Al_2O_3 area. f-g) High energy electron irradiation triggered crystallization in TEM. h) TEM induced in situ volume change of the tube left arm due to crystallization. i) AFM measurement for Al_2O_3 volume change under electron irradiation (5 kV) with different beam currents and film thicknesses for 5 minutes.

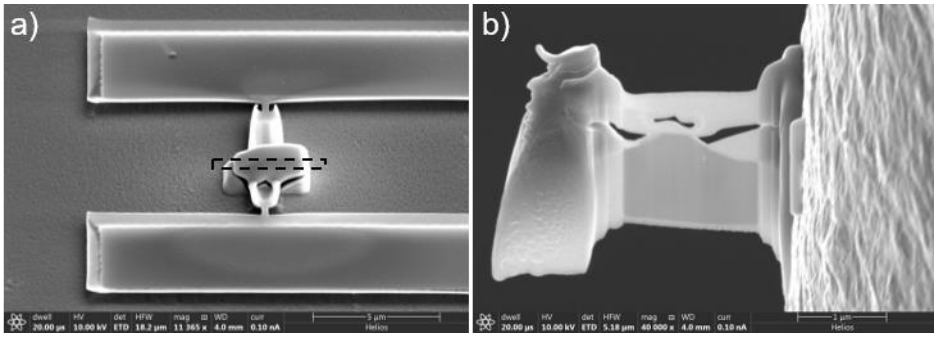

Figure 4.3 TEM preparation of the partially curved tube in a dual beam (FIB/SEM) system. a) Pt deposition by electron beam and focused ion beam. b) TEM sample prepared after ion beam thinning.

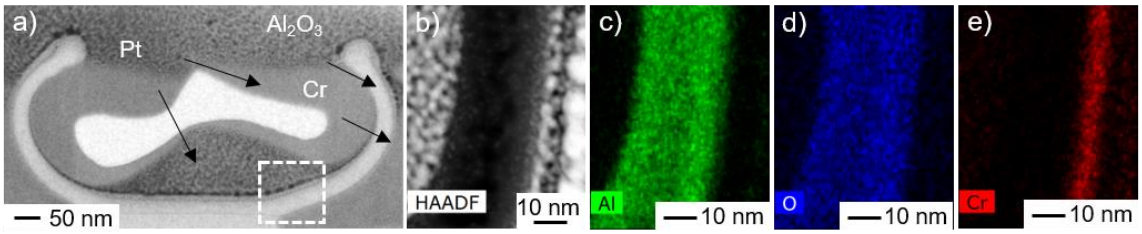

Figure 4.4. a) TEM sample of partially curved tube structures prepared by FIB. b-e) The high-angle annular dark-field scanning transmission electron microscopy (HAADF-STEM) (b) and energy dispersive spectroscopy (EDS) mapping of (c) Al in green, (d) O in blue, and (e) Cr in red.

amorphous-Al_2O_3 to α-Al_2O_3 (Figure 4.2f,g). According to the interplanar d-spacing of 0.238 nm and 0.255 nm respectively (Figure 4.5), the orientation of α-Al_2O_3 nanocrystallites are confirmed as [110] and [104]. This observation is clear evidence showing electron irradiation has the ability to trigger a crystallization process in amorphous materials. As for the mechanism of electron irradiation induced crystallization, it still remains greatly controversial. Previous studies suggested high temperature induced by e-beam irradiation is the key factor for crystallization of the amorphous thin film [194]. However, Nakamura *et al*. later found the temperature rise caused by e-beam heating is much lower than the required annealing temperature for Al_2O_3 crystallization [195]. Thus, the electronic excitation process, rather than e-beam heating induced temperature raise, is the dominant factor for the migration of atoms in the materials, triggering crystallization. Based on this theory, electron irradiation even at low acceleration voltages and currents (5 kV, 0.8 nA) directly break and rearrange thermodynamically unstable bonds in the amorphous material, resulting in crystallization without the assistance of temperature rise. The crystallization induces volume shrinkage and, in our case, a 22% thickness change has been observed after e-beam irradiation in a TEM, which results in further structural deformation even if the tube is embedded in a Pt coating (Figure 4.2h).

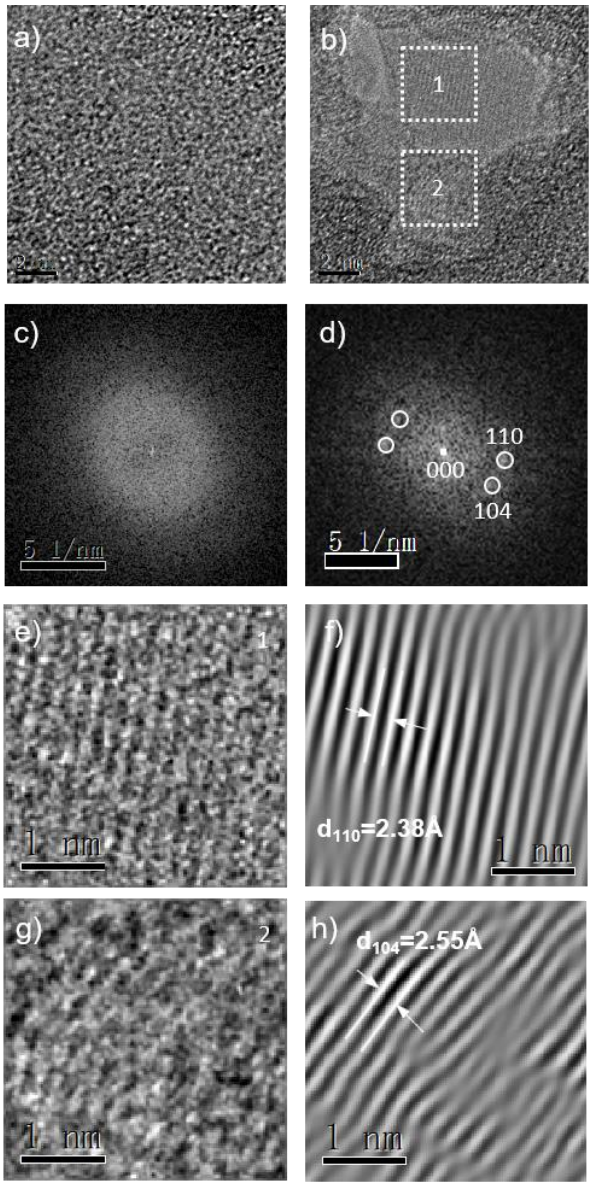

Figure 4.5. TEM images (a-b) and FFT patterns (c-d) of the Al_2O_3 layer before (a,c) and after (b,d) electron irradiation with 300 kV for 10 sec. The high energy irradiation can crystalize the amorphous Al_2O_3 (a,c) into well-defined crystalline (b,d). e,f) The zoomed in TEM image and Fourier Transform analysis of area 1 in b). The nano-crystallite has a hexagonal structure with [110] orientation and interplanar d-spacing of 2.38 Å. g,h) The zoomed in TEM image and Fourier Transform analysis of area 2 in b). The nano-crystallite has a hexagonal structure with [104] orientation and interplanar d-spacing of 2.55 Å.

To systematically quantify the e-beam irradiation inducing volume change, 6 µm × 6 µm amorphous Al_2O_3 plateaus of varied thicknesses (9, 18, 36, and 54 nm) are deposited on a Si substrate. The plateaus are irradiated for 5 minutes under an e-beam with a bias voltage of 5 kV and currents of 1.6, 6.4, 26, and 100 nA. Under electron irradiation, the oxygen in the pristine, oxygen-rich amorphous aluminum oxide layer is extracted due to the electron induced electric field [196]. In addition, the excitation process triggered by e-beam irradiation rearranges the atoms to form a more closely packed crystal structure [195]. As a result, the volume of the Al_2O_3 layer is decreased. Because the bottoms of the plateaus are confined on the substrate, the volume change occurs mainly in the z-direction, shown

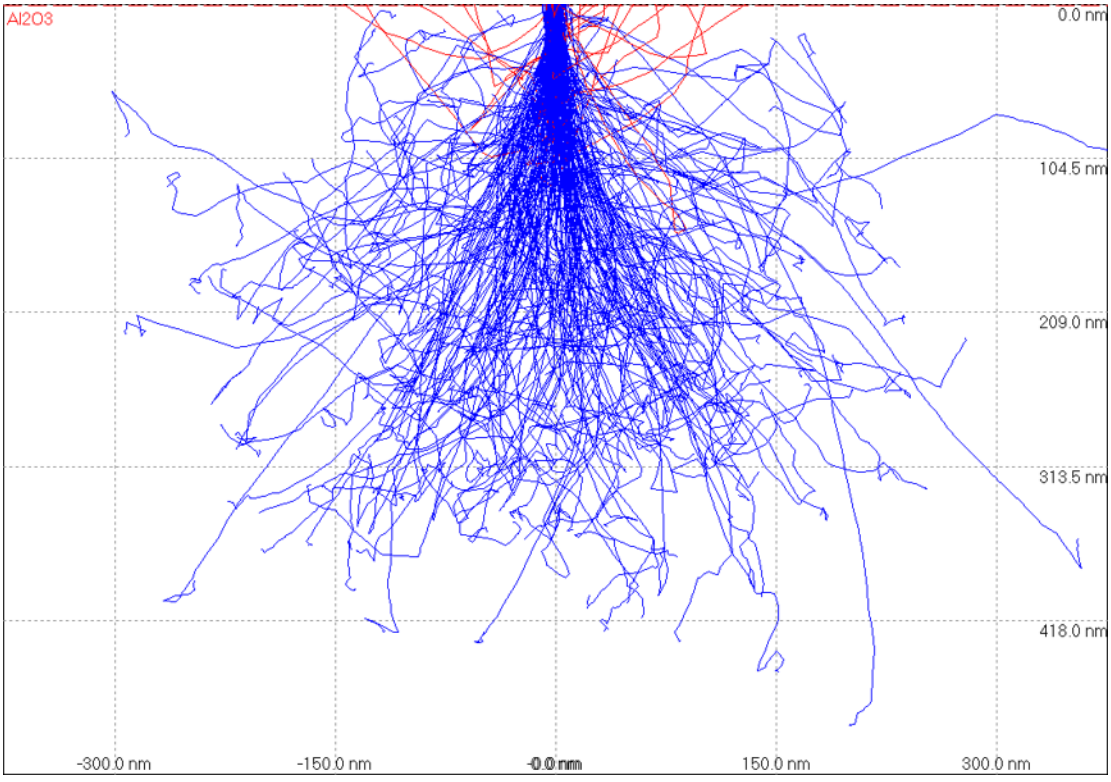

Figure 4.6 Monte Carlo simulation of 5 kV electron trajectory in 500 nm thick Al_2O_3 using Casino Simulator Version 2.51. The electron can reach to more than 400 nm inside the Al_2O_3 films.

as a thickness reduction (Figure 4.2i). Atomic force microscopy (AFM) is used to measure the plateau thickness before and after irradiation. Even though the pristine film thicknesses experience six times difference, the thickness reduction shows saturation at around 22% (Figure 4.2i), which indicates the crystallization is completed at this stage. We attribute this behavior to the long electron implantation range at the bias voltage of 5 kV, which is more than 400 nm based on Monte Carlo simulation of electron trajectory into an Al_2O_3 layer (Figure 4.6). The long implantation range enables crystallization in the entirety of a 10~50 nm thick Al_2O_3 layer, resulting in a saturated thickness reduction (22%). The understanding and quantitation of volume reduction can play a key role in designing self-assembly strategies to achieve desired 3D nanostructures.

4.1.4 Folding Analysis

Numerical analysis for achieving a quantitative understanding of curving behavior is conducted by studying the effects of film thickness and coverage length of the bilayer system. Two sets of experiments are carried out on the bilayer beams, with 100 nm width and 1 μm length. First, the thickness of the Cr layer is fixed at 10 nm and the thickness of Al_2O_3 is varied to four different quantities, 10, 20, 30, and 40 nm (Figure 4.7a-d). Then, the thickness of the Al_2O_3 layer is fixed and the thickness of the Cr is changed in the same manner as for Al_2O_3 in the first case (Figure 4.7e-h). The e-beam voltage, current, exposure time, and magnification are set to be 5 kV, 6.4 nA, 100 sec, and 5000X to maintain an identical irradiation condition. Increasing the deposited thickness of the passive curving layer (Cr) shows a more critical influence on changes to the radius curvature than increasing the initial thickness of the active curving layer (Al_2O_3) (Figure 4.7 a-i) even

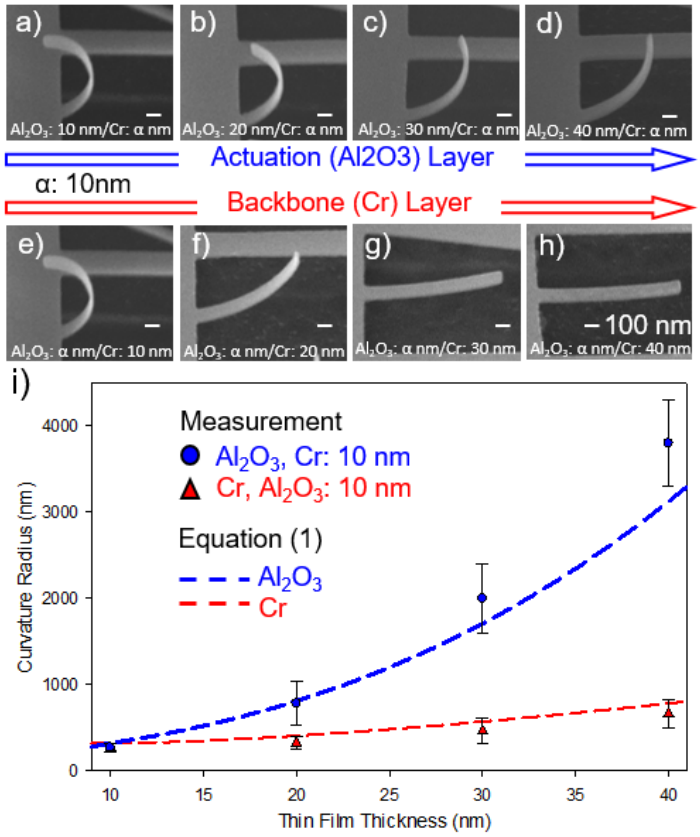

Figure 4.7 Effect of film thickness and relative coverage on self-assembly. The self-assembly result of the samples with a-d) 10 nm Cr and increasing Al_2O_3 layer thickness (10, 20, 30, and 40 nm) and e-h) 10 nm Al_2O_3 and increasing Cr layer thickness (10, 20, 30, and 40 nm). i) The curving radius of the different combinations of material thickness are measured and modeled.

though there is no significant discrepancy between the Young's modulus of Cr and Al_2O_3. This behavior is attributed to increased Cr thickness inducing additional resistance to bending, leading to a larger curving radius. In the case of varying the Al_2O_3 layer, the increased Al_2O_3 thickness causes higher resistance but also more stress generation when acting as the actuation (active) layer for curving, resulting in a smaller radius of curvature

when compared to the cases of increased Cr thickness. Based on this mechanism, a new model (Eq. 4.1) inspired by thermal expansion curving of thin films [197] has been developed. In the model, the radius of curvature, R, is described as:

$$R = h^2 \frac{3 \cdot (1+m)^2 + (1+m \cdot n)\left[m^2 + \frac{1}{m \cdot n}\right]}{6 \cdot Q_a \cdot E \cdot T_a \cdot (1+m)^2} \tag{4.1}$$

where T_a is the thickness of Al_2O_3 film, T_c is the thickness of Cr film, $h=T_a+T_c$ is the thickness of bilayer system, $m=T_a/T_c$ is the thickness ratio of the Al_2O_3 layer to the Cr layer, $n=Y_a/Y_c$ is the ratio of the Young's modulus of Al_2O_3 to that of Cr, and E stands for e-beam irradiation energy. Q_a = 15.6/J is the shrink coefficient obtained by curve fitting. The detailed derivation of the equation is shown in Section 4.15. As plotted in Figure 4.7i, the theoretical modeling result coincides with the experimental measurement, which shows the radius depends not only on the overall bilayer thickness but also on the thickness ratio of the two materials. This model offers an insight into the mechanism of electron irradiation triggered assembly and assists with structural design.

In addition, the curving behavior can be further modified via arranging the material layout and structural configuration. By applying a third Cr layer on top of the Al_2O_3/Cr bilayer system, the curving behavior (Figure 4.8a,d) is confined to the bilayer-only areas (Figure 4.8b,c,e,f). In the Cr/Al_2O_3/Cr tri-layer area, both the top and bottom interfaces of the Al_2O_3 layer are constrained by the rigid Cr layers, which induces similar stress for upward and downward curving, leading to an equilibrium system. Therefore, the tri-layers remain flat as long as the stress generated under irradiation is not sufficient to cause cracks in the Cr layers. When the length of the bilayer area is reduced to 400 nm, the curving behavior is restricted to this portion of the 1 μm long cantilever, realizing nano-weaving

(180º folding behavior, Figure 4.8b,e). Next, when the bilayer area is reduced to 100 nm, the cantilever can only be curved up to 90 degrees regardless of the irradiation time, (90º folding behavior, Figure 4.8c,f). It should be noted this approach offers a design concept that curving, weaving, and folding behaviors can be integrated together *via* changing the material layout and applying a programmable stimulus sequence to realize advanced 3D nano-architectures. Moreover, the long penetration depth of the e-beam overcomes the shadow effect that normally limits folding angles to 90 degrees [111] and allows more than 180 degree folding angles.

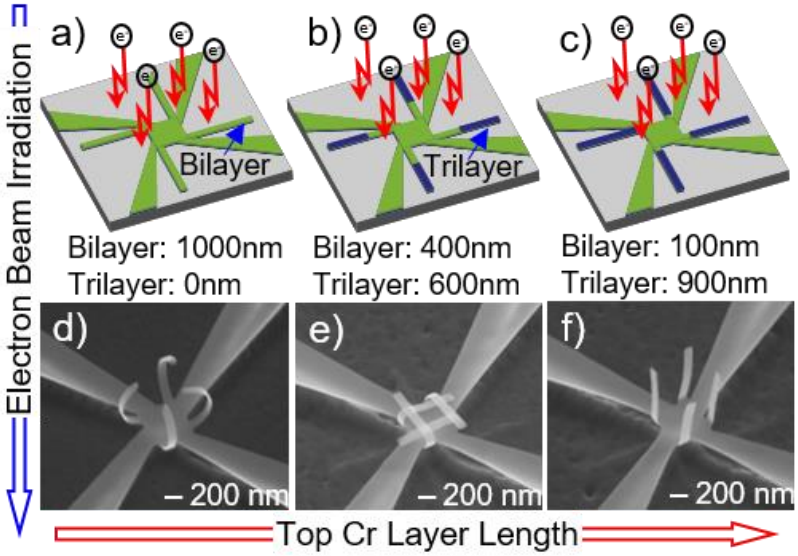

Figure 4.8 SEM images showing the effect of relative coverage of the additional Cr layer on the assembly behavior of the Cr/ Al2O3 bilayer system. a,d) The curving behavior of 1 μm long beams is transformed into b,e) weaving and c,f) folding with 600 nm and 900 nm of additional Cr layer coverage.

4.1.5 Modeling of Shrinkage Induced Assembly of a Bilayer System

Radii of curvature for initially strained bilayers can be predicted by previously developed models [54, 173]; however, few models can describe the post volume change, especially shrinkage, induced deformation of a freestanding bilayer, leading to difficulty in predicting how the radius of curvature changes with respect to modification of the thickness of the active (Al_2O_3) or the passive (Cr) layers (Figure 3a-i). To describe the folding behavior of the bilayer system in response to electron irradiation, we developed a new model based on the shrinkage mechanism. In our model, we assumed the linear shrink coefficient (Q) of each layer, Qa for Al_2O_3 and Qc for Cr, was the same across the thin film during the entire irradiation process. The irradiation induced total shrinkage, S, was decided by the shrink coefficient, Q, and irradiation energy, *E*.

$$S = Q \cdot E \tag{4.2}$$

If we assume the irradiation energy is uniformly absorbed by the bilayer system, the absorbed energy for each layer can be related to the film thickness, Ta for Al_2O_3 and Tc for Cr. Then equation (4.2) can be rewritten to be:

$$Sa = \frac{Qa \cdot E \cdot Ta}{Ta + Tc} \tag{4.3}$$

$$Sc = \frac{Qc \cdot E \cdot Tc}{Ta + Tc} \tag{4.4}$$

Based on the developed mechanism, only the Al_2O_3 layer of the bilayer system shrinks, making the structures fold to the Al_2O_3 side (Figure 4.9).

In the system, all the forces acting on the thin film are represented by an axial force, tensile force Fa for Al_2O_3 and compressive force Fc for Cr. As no external force is applied to the system, all the forces are in equilibrium.

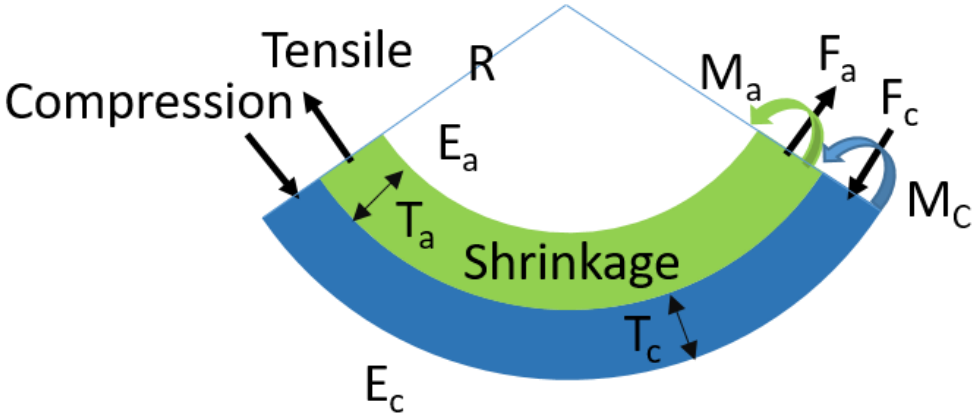

Figure 4.9. Schematic showing the deflection under electron irradiation induced crystallization

$$Fa = Fb = F \tag{4.5}$$

Therefore, the combined bending momentum, Ma + Mc, is expressed as F·(Ta+Tb)/2, where Ta and Tc denote the thickness for Al_2O_3 and Cr respectively, giving the equation:

$$Ma + Mc = F \cdot \frac{Ta + Tb}{2} \tag{4.6}$$

Based on the moment-curvature relation, the momentum, M, can be expressed by curvature radius, R, and flexural rigidity, Y·I, where Y is the elastic moduli and I is the second moment of area:

$$Ma = \frac{Ya \cdot Ia}{R} \quad for \text{ Aluminum } Oxide\ layer \tag{4.7}$$

$$Mc = \frac{Yc \cdot Ic}{R} \quad for\ Cr\ layer \tag{4.8}$$

Therefore, equation (4.6) can be rewritten to be:

$$\frac{Ya \cdot Ia + Yc \cdot Ic}{R} = F \cdot \frac{Ta + Tb}{2} \tag{4.9}$$

During the bending process, the longitudinal lengths of the two layers are changed differently in response to irradiation induced shrinking, internal force induced deformation, and curvature. However, the contact surface of the two layers should experience the same amount of dimension change, giving an equation showing the relationship:

$$Sa - \frac{Fa}{Ya \cdot Ta} - \frac{Ta}{2R} = Sc + \frac{Fc}{Yc \cdot Tc} + \frac{Tc}{2R} \tag{4.10}$$

Combining this with equation (4.5) and (4.9), equation (4.10) can be rewrote as:

$$Sa - Sc = 2(Ya \cdot Ia + Yc \cdot Ic)\frac{\frac{1}{Yc \cdot Tc} + \frac{1}{Ya \cdot Ta}}{(Ta + Tc) \cdot R} + \frac{Ta + Tc}{2R} \tag{4.11}$$

To simplify the equation, let m=Ta/Tc, n=Ea/Ec, and h=Ta+Tc. In addition, based on the definition of second moment of area, Ia and Ic can be expressed as $Ta^3/12$ and $Tc^3/12$ respectively. The curvature radius R is expressed as:

$$R = h \cdot \frac{3 \cdot (1+m)^2 + (1 + m \cdot n)\left[m^2 + \frac{1}{m \cdot n}\right]}{6 \times (Sa - Sc) \cdot (1+m)^2} \tag{4.12}$$

As the Cr layer does not experience volume change under electron irradiation, Sc is equal to zero and the final expression for R is:

$$R = h \cdot \frac{3 \times (1+m)^2 + (1 + m \cdot n)\left[m^2 + \frac{1}{m \cdot n}\right]}{6 \cdot Sa \cdot (1+m)^2} \tag{4.13}$$

$$Sa = \frac{Qa \cdot E \cdot Ta}{Ta + Tc} \tag{4.14}$$

As Sa is known as equation (4.14) and h=Ta+Tc, the radius of curvature can be expressed as:

$$R = h^2 \frac{3 \cdot (1+m)^2 + (1 + m \cdot n)\left[m^2 + \frac{1}{m \cdot n}\right]}{6 \cdot Q_a \cdot E \cdot T_a \cdot (1+m)^2} \tag{4.15}$$

4.1.6 Bidirectional Self-Assembly

The e-beam triggered self-assembly process is not limited to unidirectional curving or folding. By modifying the material layout, the area generating stress in the thin film can be engineered. If the relative positions of the Cr and Al_2O_3 are flipped, the stress will be induced in the bottom layer instead of the top layer, transforming the upward curving into downward curving (Figure 4.10a). Both the upward (Figure 4.10b) and downward (Figure 4.10c) curved tubes with different diameters (477, 381, and 286 nm) are realized by tuning the material layout. When two different material layouts are cemented next to each other, both upward and downward curving are achieved in the same structure thereby forming bidirectional curving (Figure 4.10a). Based on the design of the conjunct area, bidirectional curved tubes with different radii have been realized (Figure 4.10d).

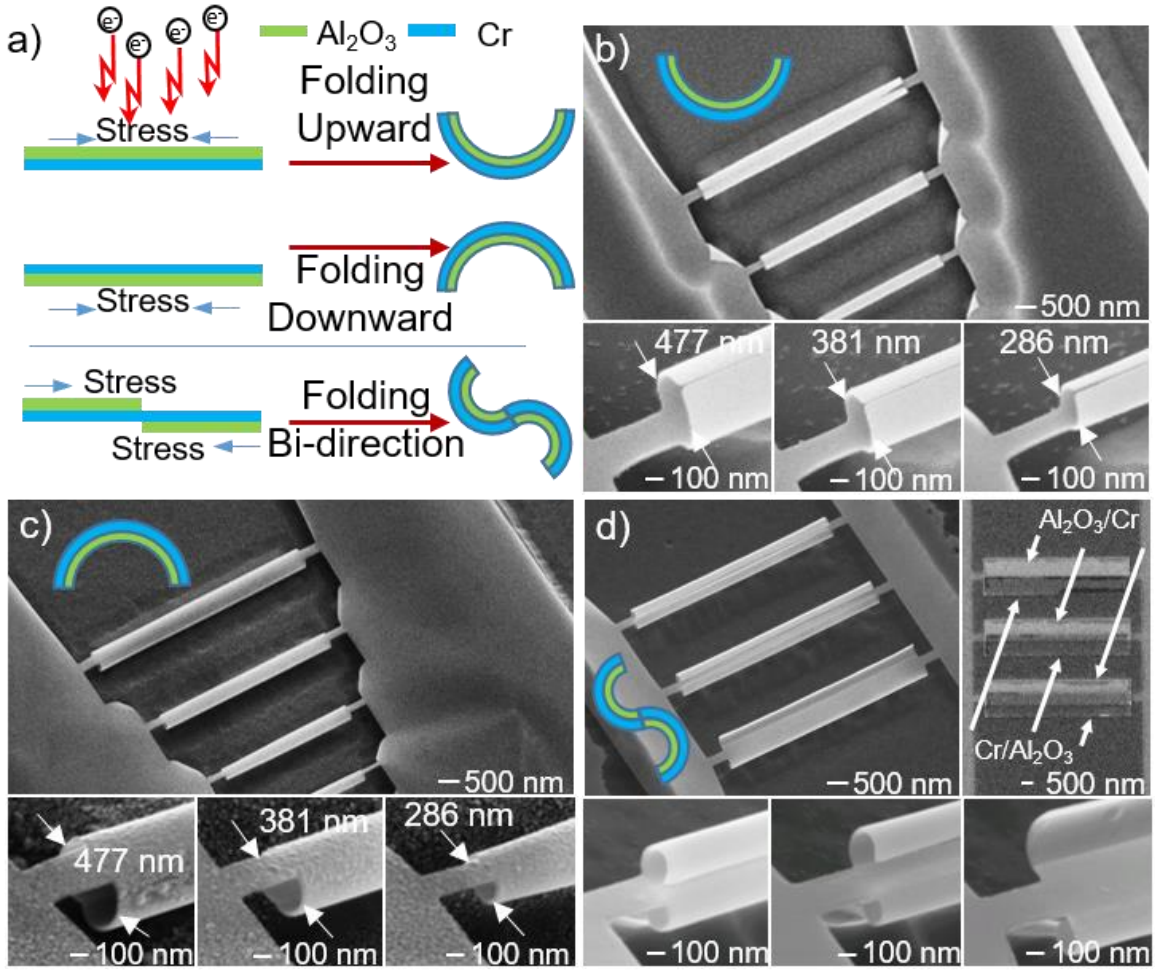

Figure 4.10 Multi-directional assembly of 3D complex nanostructures. a) Schematics and b-d) SEM images showing the bidirectional curving of tube structures. Various sizes of the tube structures are realized with b) upward, c) downward, and d) combined directional curving.

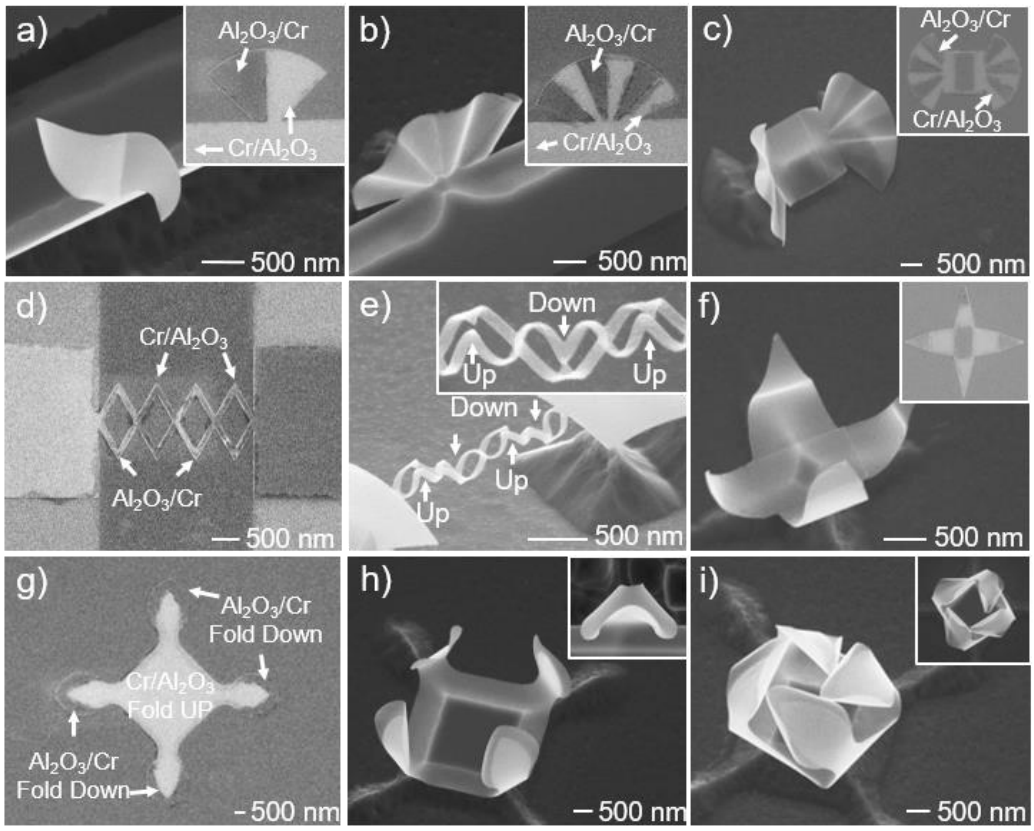

Figure 4.11 Multi-directional assembly of complex nano-architectures.

With more degrees of freedom, multi-directional assembly can be achieved. By cementing together three different material layouts (Figure 4.11a inset), curving structures with three distinct curving directions have been assembled with an upward curving base area and bidirectionally folding sector structures (Figure 4.11a). By integrating more sections of different layouts in the same pattern of Figure 4.11a, an oriental fan is demonstrated on the Si substrate (Figure 4.11b). To further demonstrate the capabilities of this approach, an origami butterfly, chain, and crane have been assembled based on the same strategy (Figure 4.11c-f). This powerful nanoscale self-assembly process enables

various functions human hands can do such as folding, curving, stretching, and weaving, showing the possibility to fully mimic origami and kirigami. As a demonstration, a flower ring, which consists of various folding or curving sections, has been assembled by precisely controlling the irradiation area, location, and sequence (Figure 4.11g-i).

4.1.7 Programmable Assembly and Applications

This e-beam induced, sequential, programmable self-assembly methodology opens up various application possibilities due to precise control of the irradiation-pattern, -sequence, and – energy exposed to the nanostructures. The combined functions of controllable, localized irradiation and real-time imaging make it possible to trigger localized folding or curving. Through modifying the irradiation pattern on a released bilayer system (10 nm Cr and 10 nm Al_2O_3) (Figure 4.12a,e), a rectangular film has been assembled into three completely different forms with two curved edges (Figure 4.12b,f), four curved corners (Figure 4.12c,g), and a combination of a curved edge and corners (Figure 4.12d,h). The diverse outcomes achieved from the same starting 2D structures demonstrate the ability to overcome the geometric limits of 2D patterns. Also, it shows the possibility to realize mechanical functions by modifying the motion of thin films. A suspended bilayer system (10 nm Cr and 10 nm Al2O3) with a hole and a cantilever is defined on a Si substrate to demonstrate a locking behavior as a nano-machine (Figure 4.12i,m). When the overall structure is exposed to electron irradiation, universal stress is induced in the thin films. As a result, the cantilever and corners fold up prior to the rest of the structure, which results in these portions contacting the main portion of the structure prematurely thereby impeding further folding (Figure 4.12j,n). When the irradiation area is well programmed to move

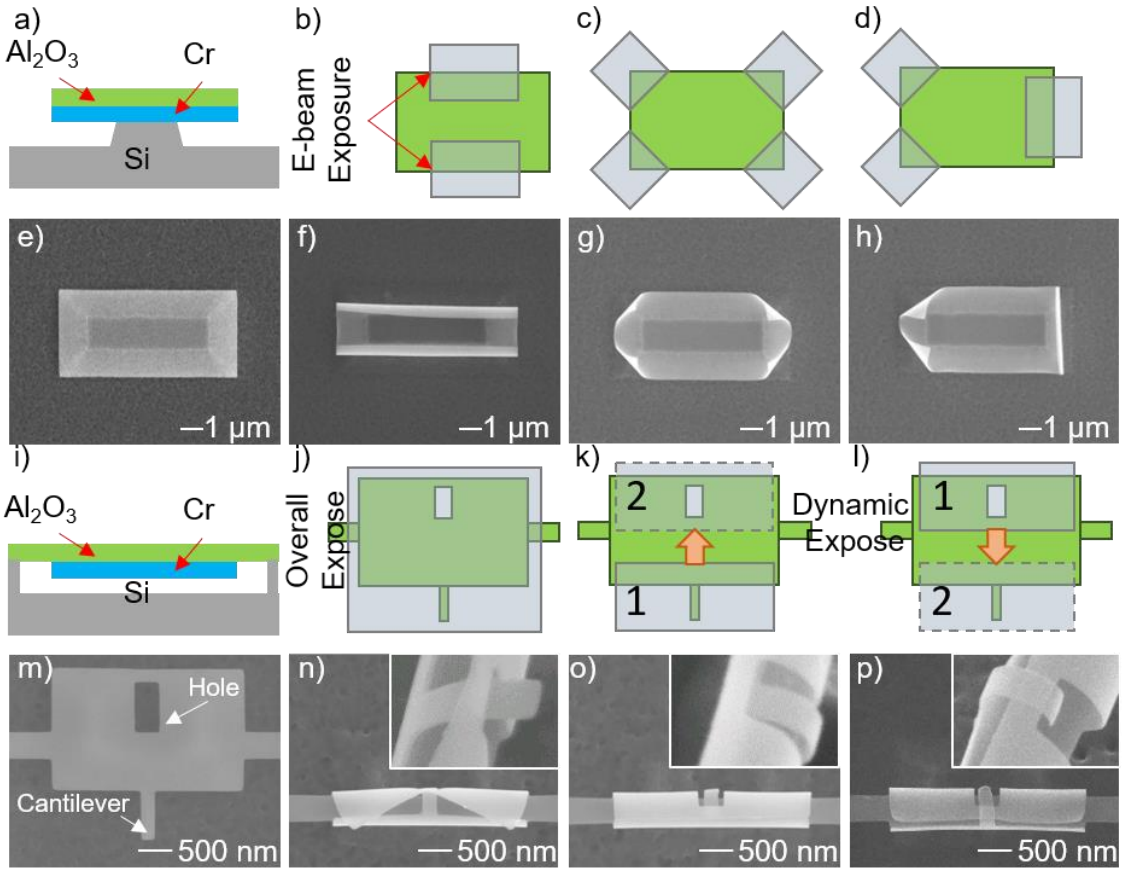

Figure 4.12 Schematic and SEM images showing the programmable assembly and potential applications realized by e-beam induced self-assembly. a-h) Different assembly outcomes are achieved on a rectangular sheet with b,f) curved edges, c,g) curved corners, or d,h) combination of both behaviors via localized irradiation. i-p) The programmed irradiation triggers k,o) internal and l,p) external locking behaviors.

from the cantilever to the hole (irradiate pattern 1 first and then move to pattern 2 in Figure 4.12k), the cantilever is designated to fold before the area around the hole. This irradiation sequence produces a tube structure with the cantilever penetrated through the hole as an internal locking mechanism (Figure 4.12o) If the irradiation sequence is reversed (Figure

4.12l), the beam hooks through the hole from the outside of the tube, locking externally (Figure 4.12p). It should be noted this sequential, programmable assembly process enables tunable outcomes for the realization of various 3D nanostructures functionalized for specific purposes even though the 2D patterns are the same before self-assembly. The desired sequence of irradiation brings an additional dimension into 3D structure design, allowing a researcher to further modify the 3D architecture after 2D pattern design.

The movement of the thin film induced by localized e-beam irradiation can be further used as an actuator to power nano-machines or as a nanoscale test platform. A nanoscale stress test platform that consists of anchors, two tubular actuators, and a nanospring (10 nm Cr and 10 nm Al_2O_3) as a functional component of has been fabricated (Figure 4.13a-c). While electron irradiation is delivered to the actuator patterns, the patterns curl up to be a tubular structures and stretch the 2D nets which become a tensioned nanospring (Figure 4.13c). With further design and calibration, this test platform may be applied to nanoscale stress tests for various applications such as flexible material or kirigami structures. In addition, surface patterning with secondary materials can be incorporated into the 3D structures to achieve advanced 3D functional nanomaterials and devices. As a proof of concept, chiral structures have been realized inside a nanotube by integrating patterns (gold stripes) on top of a 10 nm Al2O3 rectangular thin film (before e-beam irradiation: Figure 4.13d and inset in 4.13e, after e-beam irradiation: Figure 4.13e). In addition, because of the localized stress generation with the desired energy supplied at each location, assembly processes with various functionalities can be integrated next to each other, showing the potential to build comprehensive devices. This ability is

demonstrated with the creation of a flower shape (lucky clover) and tubes with different radii of curvature all on the same substrate (Figure 4.13f.g).

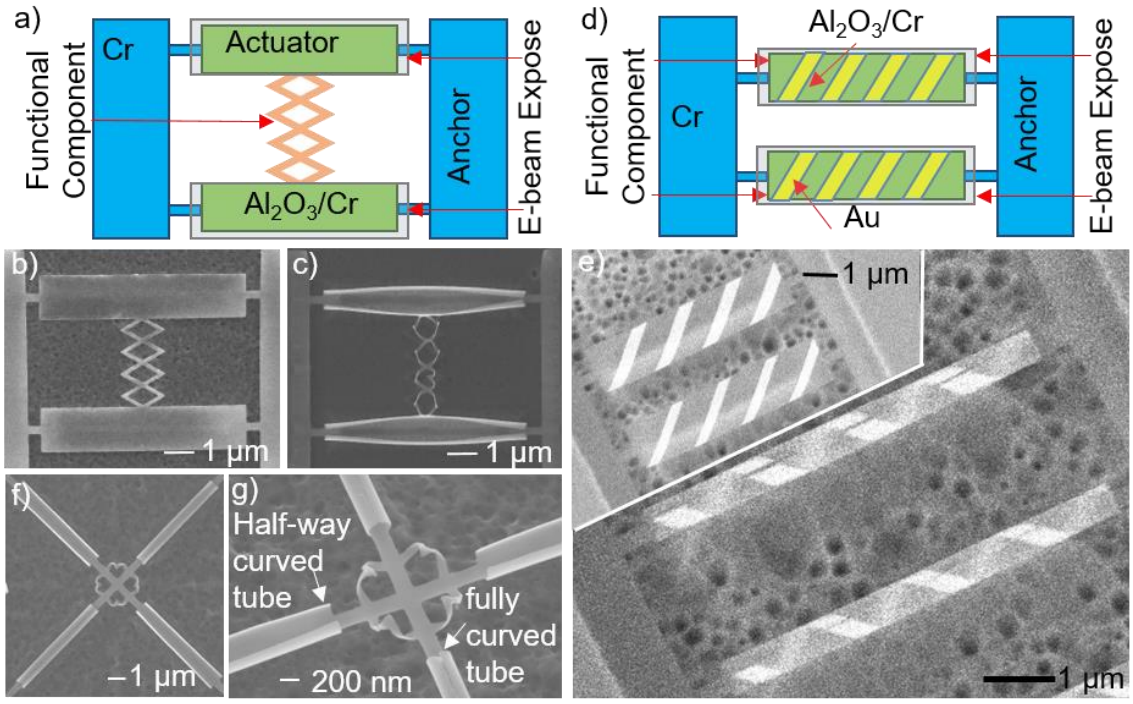

Figure 4.13 a-c) Nano stress-test platform and d,e) nano chiral materials have been realized via integrating functional components with the curving structures. f,g) A system integrated with various structures and assembly behavior is achieved.

4.1.8 Quick Summary

In this section, I developed a sequential, programmable self-assembly methodology triggered by electron irradiation. By combining the design of 2D patterns, application of localized stress generation, and execution of 3D assembly steps in a particular, desired order, it is possible to achieve the various functions of human hands including multi-directional folding, curving, stretching, weaving, and sequential assembling, thereby

enabling origami and kirigami to be mimicked on the nanoscale level to allow the realization of tunable 3D structures. Various complex 3D nanostructures and prototype devices are demonstrated based on this method, showing the possibilities for pushing self-assembly to a new level for applications in nanoscale 3D devices, machines, and robotics.

4.2 Electron Irradiation Triggered Reversible Self-Assembly

4.2.1 Importance of Reversible Motion

Energetic irradiation (*i.e.* ion or electron) triggered in situ monitored self-assembly has undergone great growth due to its capability for precisely tailoring the deformation of two-dimensional (2D) [79,83,111,123,145,198,199] or one-dimensional (1D) [200, 201] micro and nanostructure to achieve higher dimensional complex architectures. Owing to a wealth of physical interaction between energetic irradiation and materials, stress generation and imaging can be simultaneously achieved under an ion or electron beam, leading to in situ monitored self-assembly. In addition, the tunability of the ion or electron beam enable precise delivery of ions or electrons to specific spot with required dose. The combined advantages equipped this assembly with controllability and programmability. Compared to previous developed self-assembly techniques, such as metal assisted etching, RIE, epitaxial thin film strain, it demonstrates architecture with much more complexity at a higher yield.

However, one major fundamental challenge remains as far as how to achieve reversible self-assembly in nanoscale. Reversible motion is an important function for self-assembly, which can triggers advanced application in various field, such as nanomachine

[202] and reconfigurable optical devices [174]. Although, researchers proposed the theoretical possibility to achieve bidirectional folding by tuning the implantation range of an ion beam, it has not been demonstrated experimentally due to the significant defect induced by ion beam. In addition, there is no strategy for using energetic irradiation to achieve reversible assembly yet, which limits the development of this useful technique.

In this Section, I cover the strategy to achieve reversible self-assembly using electron irradiation triggered polymer degradation. By tuning the voltage of the electron beam, the degradation area in the polymer can be precisely controlled, which enable the control of folding direction. Further, two strategies for reversible self-assembly are covered.

4.2.2 Concept of Electron Irradiation Triggered Polymer Film Self-Assembly

Electron irradiation triggered polymer degradation is a well-known process. PMMA experiences significant shrinkage under the electron irradiation due to the outgassing [203, 204]. As a result of the electron irradiation, the side chain in PMMA is first removed by electron bombardment [203]. Next, the principle chain scission will be triggered [204]. The chain scission causes emission of decomposition gases, such as CO_2 and CH_4 (Figure 4.14a)[203], leading to reduce thin film volume. The absorbed energy is the determinant factor for the PMMA shrinkage. The area in the PMMA thin film that absorbed more energy from electron irradiation always has more dramatic shrinkage.

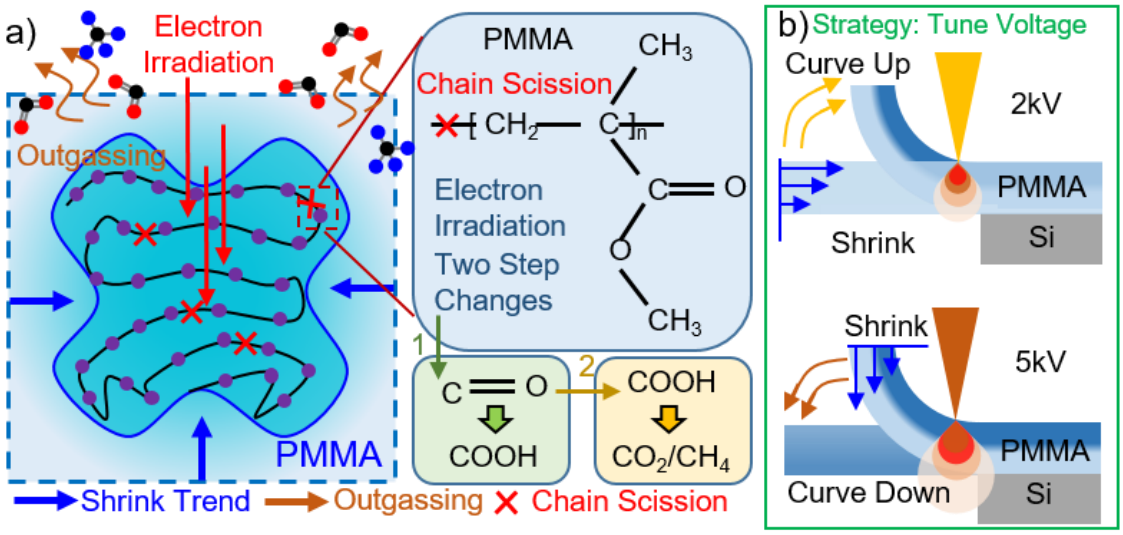

Figure 4.14 Conceptual schematics showing electron irradiation triggered PMMA change and two strategies of reversible self-assembly. a) Electron irradiation induces shrinkage of PMMA as a result of the chain scission and outgassing. b) By tuning the electron beam voltage, the shrinkage location can be precisely controlled, leading to reversible self-folding.

The positive correlation between the absorbed irradiation energy and shrinkage makes it possible to create a gradient of volume change in the thin film by tuning the electron irradiation profile. For example, a low voltage electron beam triggers more significant shrinkage at the top surface of the thin film, leading to upward folding (Figure 4.14b top). A higher beam voltage causes deeper electron implantation range, which causes higher energy absorption near the bottom surface of the PMMA thin film. As a result, significant shrinkage is triggered at the bottom surface of the thin film, leading to downward folding (Figure 4.14b bottom).

4.2.3 Demonstration of Reversible Self-Assembly

To achieve the reversible assembly process, a 2D 100nm thick PMMA butterfly structure is defined on a Si substrate through an electron beam lithography process. Next, the sample is placed in a RIE chamber to etch away the Si substrate. Once released, electron irradiation is used to trigger the folding and unfolding process. With a 2kV electron beam, the highest energy absorption area is located around 20 nm away from the top surface, leading to

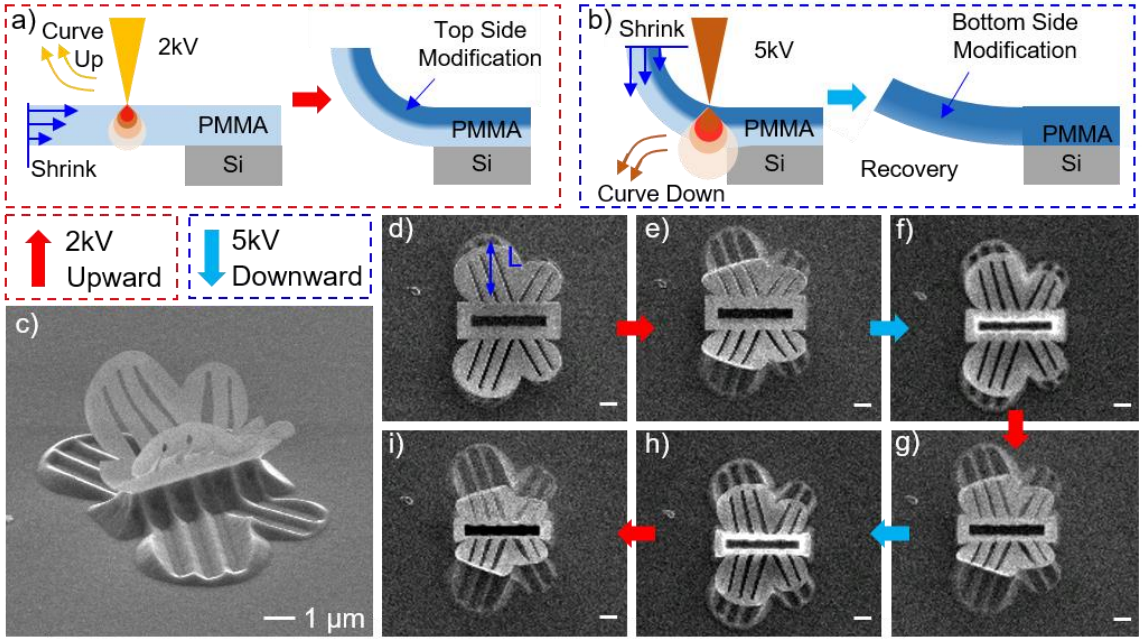

Figure 4.15, Demonstration of reversible self-assembly of a butterfly structure. a-b) Schematics showing the a) folding and b) unfolding process. c-g) SEM images showing the reversible folding process of a PMMA butter fly.

upward folding (Figure 4.15a,e). Next, the electron beam voltage is switched to 5kV, which has a highest energy absorption area at 60 nm in the thin film. As the highest energy absorption point is closer to the bottom surface, more significant shrinkage is triggered at

bottom half of the thin film, leading to downward folding (Figure 4.15b,f). By repeatedly switching the beam voltage from low to high, reversible folding process can be achieved in the PMMA butterfly structures (Figure 4.15d-g).

4.2.4 Quick Summary

In this section, I developed a reversible self-assembly methodology using electron irradiation triggered polymer degradation. Under the electron irradiation, PMMA experiences significant shrinkage. By precisely control the electron beam voltage, the location of the highest shrinkage point in the thin film can be programmed. By repeatedly switching the electron beam voltage from low to high, a reversible self-folding process has been demonstrated in a PMMA butterfly structures.

Chapter5

Self-Assembled Plasmonic Cylindrical Nanosensor

In this chapter, I demonstrate a self-assembled plasmonic cylindrical nanosensor. The present issue of plasmonic sensing is stated. Next, the concept and the fabrication process of this novel nanosensor is described in detail. The light and fluidic confinement achieved in this plasmonic cylindrical nanosensor is characterized. This chapter also covers the sensing behavior of this nanosensor for detecting hemoglobin.

5.1 Overview of Plasmonic Sensing

Plasmonic sensing, which originates from the surface plasmons' response to its proximate molecules induced refractive index change, has arisen to be a powerful technique for detecting and identifying chemical and biological components [11, 17-19, 205-210]. Moreover, nanostructured metallic surface can more tightly confine electromagnetic (EM) waves and form localized surface plasmon (LSP), which dramatically enhance the light-matter interaction, leading to strong localized field enhancement [15]. This enhanced field can further benefit plasmonic sensing techniques, leading to surface-enhanced Raman Scattering (SERS) [14, 16, 19, 205-207] and surface-enhanced infrared absorption (SEIRA) [12, 208-212]. As the sensing behavior strongly depends on the size and shape of the nanostructures [205], tremendous efforts have been put into the innovation of advanced fabrication techniques for achieving well-defined

nanoscale plasmonic structures, including electron beam lithography [15, 209, 213-215], nanosphere lithography [16, 204, 216, 222], template stripping [11, 14, 211, 217], electrochemical growth [205], and DNA self-assembly [218, 219].

However, most of these structures are demonstrated on 2D surfaces with an enhanced EM field only near the surface [220, 221], which requires additional effort to place the target molecules near the "hotspot" such as incubation in solution [14, 15, 16] and integration with microfluidic systems [12]. As the enhanced EM wave decays exponentially from the surface to the surrounding media [220, 221], the effective plasmonic sensing areas of metallic structures are restricted within in few nanometers away from the surfaces. Thus, a significant dimension mismatch exists between the nanoscale sensing distance and the microscale and even macroscale target sample volume, which results in extremely low efficiency for molecule immobilization or attachment. For example, the solution incubation requires 12 to 24 hours to attach the target molecules near the plasmonic hotspots for sensing [14, 15, 16]. As for integrating plasmonic structures into microfluidic channels, the target sample should be flowed into the devices continuously during the sensing process [12]. In addition, only the molecules near the bottom of micro-channels are taken into account for the result. The long preparation time and sample waste caused by the dimension mismatch impairs the advantage of plasmonic sensing. Therefore, it is necessary to create an efficient interaction between the target sample solution and plasmonic hotspot.

Nanofluidics stands out to be a strong candidate due to its capability to control and manipulate nanoscale fluid [228], which is in the similar range of the effective sensing

region for plamsonic sensors. Recently, cylindrical plamsonic structures have been invented to implement plasmonic sensors with nanofluidic devices, achieving field and substance confinement simultaneously [206]. However, this fabrication technique is based on ion beam milling triggered secondary electron lithography, which can only achieve hollow cylindrical shape plasmonic structures [206, 208, 212]. It is not possible to integrate most advanced plasmonic structures with better sensing behavior, such as nano-gap and nano-tip, resulting in difficulties for further exploiting the advantages of plasmonics. Therefore, there is an urgent need to develop a method that bridge the most advanced plasmonic structures with fluid channels.

Here, I present a manufacturing method based on electron beam triggered self-folding process with the combination of surface patterns (5 nm gold: Au) on aluminum oxide (Al_2O_3)-based cylindrical nanostructures, which enables direct formation of a plasmonic gap at the touching edge of the self-curved nano-cylinder. The nano-gap contributes to subwavelength field localization and enhancement, serving as a plasmonic "hotspot" for biomolecule sensing. In addition, the 3D configuration of the nano-cylinders enable fluid confinement in nanoscale dimension, which makes it possible to bring chemical and biological substance close to the effective sensing regions of plasmonic structures. By bridge nanoplamsonics with nanofluidics, a more efficient interaction between the confined EM field and target molecule is achieved, contributing to higher sensitivity. The overall sensing behavior of this 3D nano-cylinder with plamsonic gaps is characterized based on the detection of hemoglobin. Compared to 2D Au ribbon, higher

sensitivity with an enhancement factor of 10 has been observed on 3D structures. Moreover, the Raman mapping confirms that the plamonic gaps are the dominant hotspot for sensing.

5.2 Concept for Self-Assembly of Nanocylindrical Plamsonic Sensors

The three-dimensional (3D) cylindrical plasmonic sensor are fabricated through an electron irradiation induced self-assembly process (Figure 5.1). The 2D pattern before assembly consists of two components: an actuation bilayer of 1 nm thick Cr and 5 nm thick Al_2O_3, and a metallic pattern of 5 nm Au (Figure 5.1, b, c). After being released from the silicon (Si) substrate, the 2D patterns are irradiated by electron streams. The electron irradiation (5 kV) enables the transformation of amorphous Al_2O_3 into crystal Al_2O_3, which is associated with significant volume reduction. As the Cr layer is rigid, the volume change induces tensile stress in Al_2O_3 layer and compression stress in Cr layer, allowing the bilayer to curve up (Figure 5.1a). Once the two edges of the actuation bilayer touch, the curving process self-stops and forms a nano cylinder (Figure 5.1d). The Au nanoribbon also curve up together with the actuation bilayer. In addition, the self-stopping property allows the formation of a nanoscale plasmonic gap at the edge of the Au ribbon (Figure 5.1 d,e). A clear nanogap is observed in the self-assembled 3D nanocylinder using backscattered electron (BSE) image (Figure 5.1e). The detailed fabrication process are described in the Section 5.2.1. This 3D nanocylinder with plasmonic nanogap allows us to simultaneously achieve field and solution confinement for molecular sensing with higher sensitivity and faster speed. Figure 5.1f shows the idea configuration for using this 3D nanocylinder for detecting hemoglobin (Hb). The nano-cylinder serves as a nanofluidic channel to confine

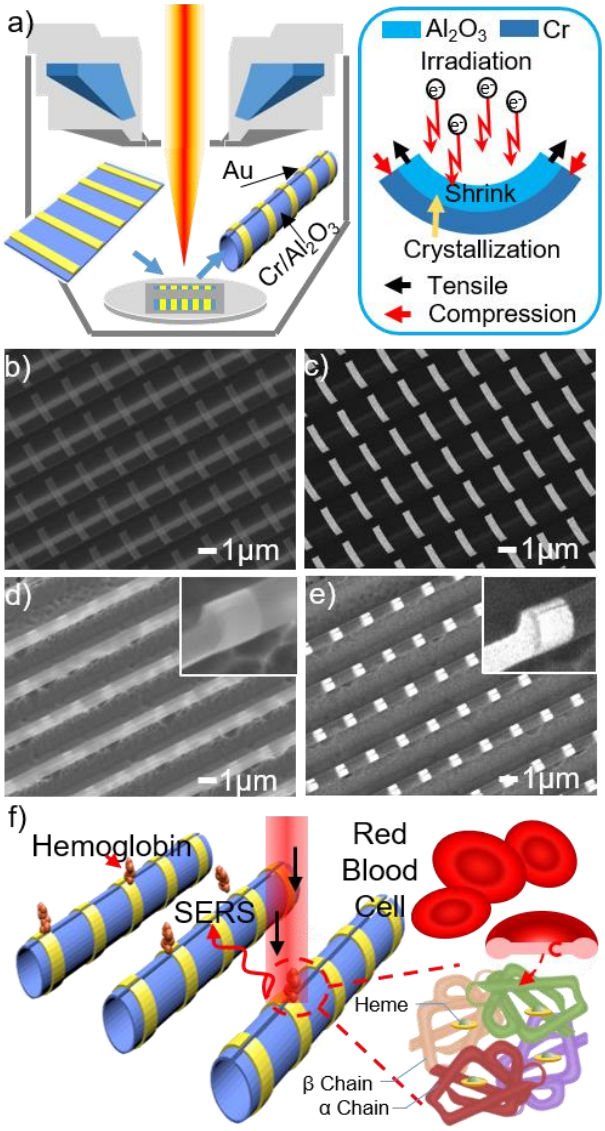

Figure 5.1, Conceptual schematics and SEM images showing the self-folding of nano-cylinder with a plasmonic nanogap for bimolecular sensing. a) System setup and mechanism of electron irradiation induced self-assembly. b) SEM and c) BSE images of the two-dimensional pattern before folding. d) SEM and e) BSE images of the self-assembled 3D nano-cylinder with a diameter of ~ 500 nm. A nano-gap is formed at the touching edges in the center of the nano-cylinder. f) Schematics showing the capability of using self-assembled nano-cylinders with a plasmonic gap for detecting hemoglobin.

the solution based target molecule near the plasmonic nanogap. The nanogap is a "hotspot" with highly confined electromagnetic field, which is expected to achieve the highestRaman enhancement [14, 15, 16]. The integration of plasmonic nanogap with nanofluidic channel enable rapid and accurate placement of target molecule at the nanoplasmonic "hotspot" for rapid sensitive detention.

5.2.1 Sample Design and Fabrication

The 2D patterns were defined on Si substrate through two steps of standard electron beam lithography (EBL) process for Cr/Al_2O_3 actuation bilayers and Au metallic structures respectively. To fabricate the actuation bilayer, an e-beam resist, polymethyl methacrylate (PMMA) A3, was spun on top of a Si wafer at 3000 rpm. Then, EBL system (Vistec EBPG 5000+) is was used to pattern the 1.5 μm × 30 μm ribbons with a beam setup of 1 nA and 1000 $\mu C/cm^2$. After developing in MIBK/IPA = 1:3 for 60 s, 1 nm Cr and 5 nm Al_2O_3 are deposited using an e-beam evaporator (RME-E2000). A lift-off process was carried out to finally remove the undesired material in the acetone bath and form the actuation bilayers (Figure 5.2 a, e, i). The 5 nm thick gold ribbons with a width of 500 nm and a length of 1.5 μm were formed on top of the actuation bilayer *via* a similar EBL process (Figure 5.2 b, f, j).

To release the 2D patterns from the Si substrate, the samples were loaded into a reactive ion etching (RIE) system (STS 320) to etch away the Si underneath the 2D pattern (Figure 5.2 c, g, k). Carbon tetrafluoride (CF_4) and oxygen (O_2) were flowed into the reaction chamber at 12 sccm and 1 sccm respectively to react with Si. The power, pressure, and reaction time were kept at 20 W, 100 mtorr, and 15 minutes. In addition, the sample

were facing down to the chamber substrate during RIE process to minimize the ion irradiation induced defect. The suspended 2D patterns were curved into 3D nano cylinder using the scanning electron microscope (SEM) inside a FEI Helios G4 UX dual-beam (FIB/SEM) system. The e-beam voltage was set at 5 kV and the beam currents were ranged among 0.8 nA, 1.6 nA, 6.4 nA to 26 nA based on the size of the array and the desired folding speed.

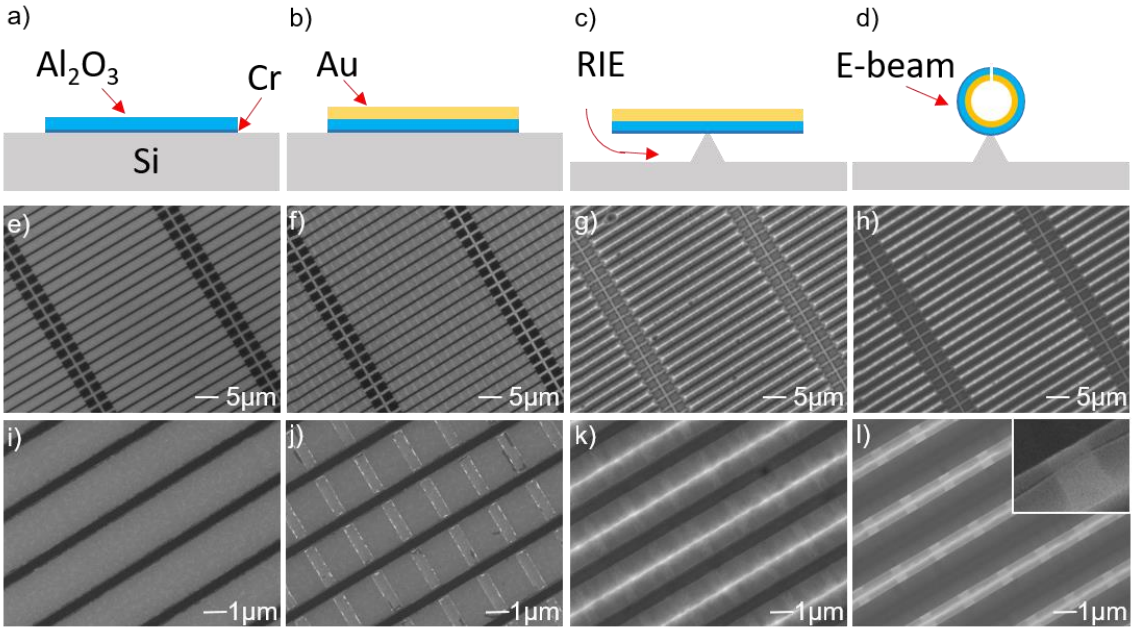

Figure 5.2, Fabrication process of nano-cylinder with a plasmonic gap. a, e, i) 1 nm thick Cr and 5 nm thick Al2O3 layer is form onto of high resistivity Si substrate as the actuation layer. b, f, j) 5 nm Au is patterned on top of the Cr/Al2O3 bilayers as optical components. c, g, k) reactive ion etching is conducted to etch away the Si and release the 2D patterns. d, h, l), Electron irradiation is used to crystalize the amorphous Al2O3 and trigger volume reduction, which will generate stress to fold the 2D ribbons out of plane to be 3D nano-cylinder. The gold pattern will form a nanoscale plasmonic gap at the touching edges of the nano-cylinder.

5.2.2 Control of the 3D Structures

The shapes of the metallic structures play important roles in determining its plasmonic behaviors [217]. Various plasmonic structures, including nano-holes [12], nano-gaps [14], nano-tips [217], and nano-particles [18], have been explored and showed different plasmonic behaviors, especially field enhancement. Therefore, it is critical for plasmonic structure fabrication techniques to build various shapes. We investigated the versatility of the e-beam folding techniques and demonstrated four different 3D plamsonics structure *via* tuning the gold pattern of the 2D designs (Figure 5.3). The functional components of the 3D cylindrical plamonic sensor are based on the nano-gaps formed between the touching edges of the Au ribbon. By simply changing the Au ribbon into rhombus (Figure 5.3 a), the short edges evolve into points, achieving plamsonic nano-tips inside a nano-cylinder after self-assembly (Figure 5.3 b, c, d). Further, both the Au plasmonic structures and the supporting structures of nano-cylinders can be modified by adding a gap into the Au pattern (Figure 5.3 e-l). During self-assemble, the Au patterns works as rigid materials and induce additional resistance for curing. Both the Au ribbons and rhombus are continues layers along the curving direction, which induce relative equivalent resistance. Therefore, the deformation of the 2D pattern are in a curving format, creating nano-cylinders. The additional gaps in the Au pattern break the relative force equivalence along the curving direction. The gaps are more preferable locations for the deformation,curving up prior to the rest of the structures. As a result, the curving process is transformed into folding process. Triangular and rectangular parallel plate plasmonic structures are demonstrated using this strategy (Figure 5.3 f-h and j-l). In addition, the parallel pate structure can evolve into prism by creating more gaps in the 2D Au

patterns(Figure 5.3 m). 3D triangular prisms are fabricated by patterning two gaps in the Au patterns (Figure 5.3 n-p). Further modification of the Au pattern can lead to more complex 3D plasmonic structure, which should have potential for further exploring nano-plamsonics.

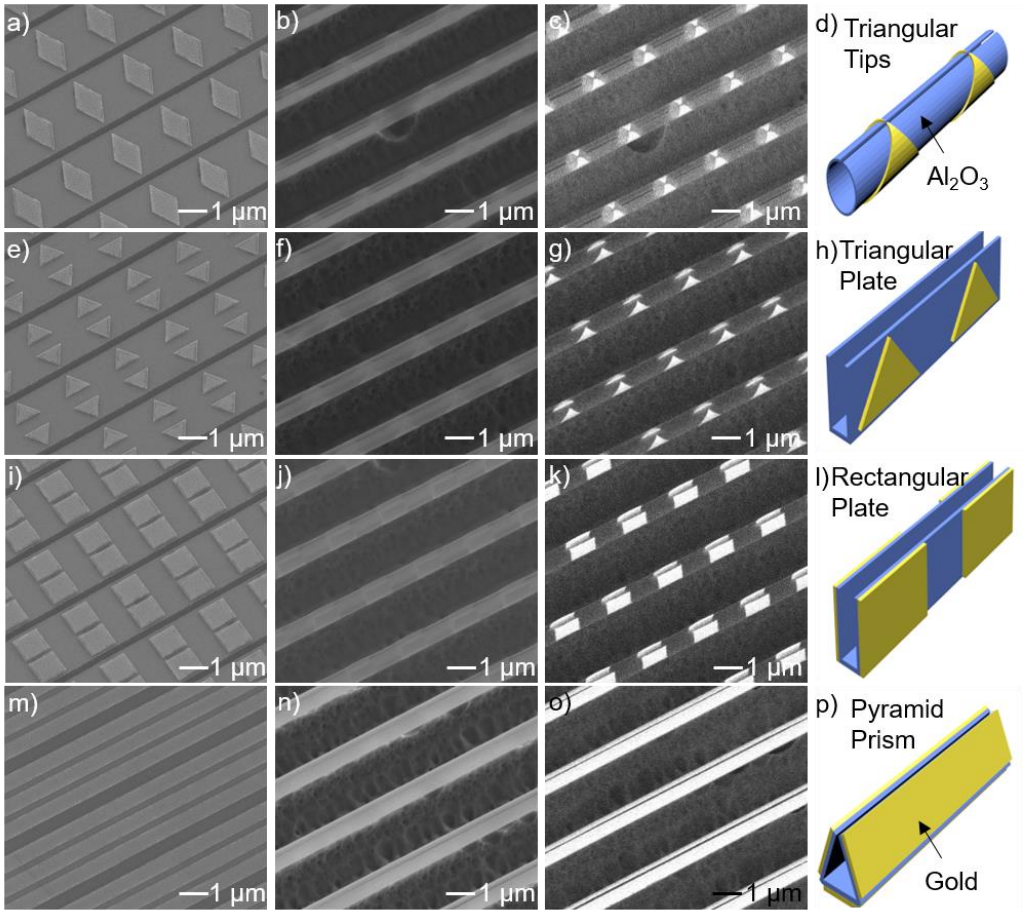

Figure 5.3 SEM, BSE, and conceptual schematics of different types of 3D plasmonic structures. The 2D designs of Au pattern determines the structure of both the plasmonic components and Al_2O_3 supporting components. a-d) triangular gold tips formed in a nano-cylinder, e-h) triangular parallel plate, i-l) rectangular parallel plates, and m-p) pyramid prism are demonstrated.

5.3 Characterization of Fluid Confinement

To understand the fluid flow and particle confinement inside the nano-cylinders, a dark field microscope and a fluorescent microscope were used for characterization. A sample that consists of 2D patterns, half-way curved nano-cylinders and fully curved nano-cylinders was fabricated by aforementioned fabrication process (Figure 5.4a). The dark field measurement, which enables the visualization of fluid flow *via* color change, was carried out first to verify whether the liquid can fill into the nano-cylinder,. A drop of isopropyl alcohol (IPA) is dropped on top of the 3D nano-cylinder arrays (Figure 5.4b). Because of evaporation, the size of IPA drop reduces, which makes the IPA flow away from the 3D nano-cylinders (Figure 5.4c). Then, the IPA inside the nano-cylinder starts to evaporate. A clear boundary change of the fluid during evaporation is monitored under the dark field microscope (Figure 5.4d), confirming that the fluid can be filled and confined inside the tube despite finally evaporated (Figure 5.4e). Further, a fluorescent measurement is conducted to evaluate the particle confinement behavior of the 3D nano-cylinder. The sample was dipped into a 2.5 mg/mL fluorescein conjugated ovalbumin for 1 hour. Ovalbumin is a widely used protein molecule that consists of 385 amino acids [223]. The relative molecular mass is 42.7 kDa [223], which corresponds to a minimum radius of ~2 nm. This value is similar to the common protein molecules [224], making ovalbumin a good representative example for molecule confinement test. In addition, the dimension is much smaller than the diameter of the nano-cylinder, ~500 nm, allowing the florescent dye conjugated ovalbumin flow into the chamber. Next, a 5 minutes water dip and gentle air gun dry out were utilized to clean up the surface attached molecules. The florescent

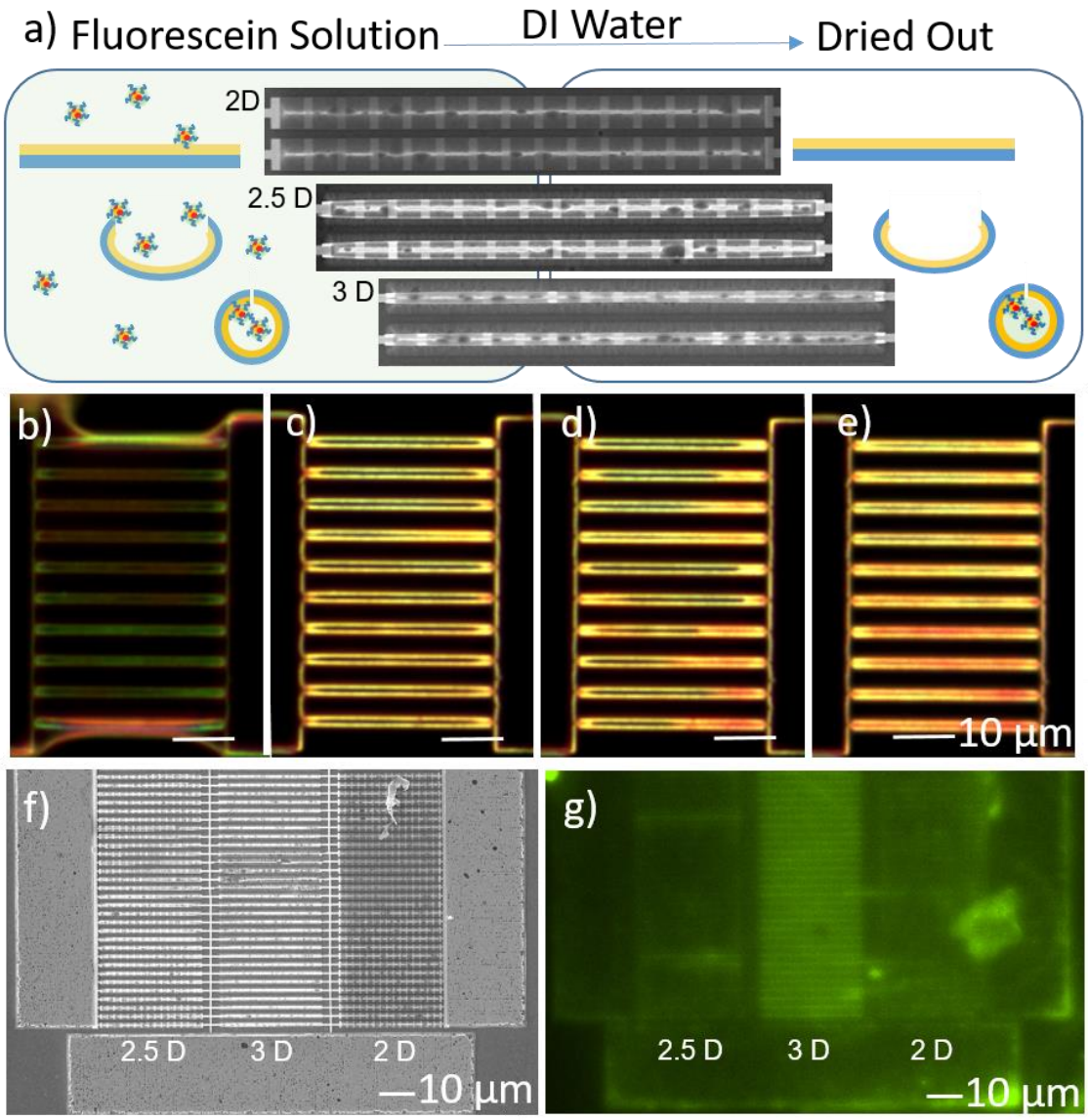

Figure 5.4 Characterization of fluid confinement on 2D ribbon, 2.5 D half-way folded nano-cylinder, and 3D nano-cylinders using fluorescent microscope. a) Schematic showing the sample preparation for fluorescent measurement. b-e) Dark field optical microscope image confirming that fluid can flow in and out of the nano-cylinder. c-e) The movement of the fluid can be clearly observed inside the nano-cylinder during the drying process. f) SEM of the samples before measurement. g) Florescent image of the sample after treatment, showing enhanced fluid confinement in 3D nano-cylinders.

measurement was carried out on the washed sample using a fluorescence microscope. The detailed measurement setup and process is described in the Method. The measurement result shows a clear difference between the area of 3D nano-cylinders and the area of 2D ribbon and 2.5D half-way curved nano-cylinders (Figure 5.4 f, g). Much brighter fluorescence is observed on the 3D nano-cylinders, which shows fair amount of molecules is still in the nano-cylinder. This observation demonstrates that the nanoscale cylindrical structure with a nano-gap not only allows the molecules to flow into it but also confines the molecule inside it. Compared to 2D patterns, the better confinement makes it a passive trap to place the target molecules close to the surface patterned plasmonic structures tightly, contributing to better sensing behaviors.

5.4 Characterization of Sensing Behavior

The overall sensing behavior of the nano-cylinders with plasmonic gaps is characterized based on surface enhanced Raman spectroscopy (SERS) for detecting hemoglobin (Hb) molecule. Hb is an important blood constituent protein, which is associated with various diseases. For example, abnormal Hb can cause sickle cell disease (SCD), which leads to cumulative organ damage, acute pain, and reduced survival [225]. More than 14 million people suffer from SCD worldwide with about 85% being in the resource-limited regions of sub-Saharan Africa where about half of the infants with SCD die before reaching the age of five. In addition, Hb has clear fingerprints range from 1000 to 1700 cm^{-1}, which have been well-characterized by SERS [226]. Moreover, Hb molecule is nearly spherical with a diameter of around 5 nm [227], which makes it able to be flowed

into the nano-clyinders. Because of the above properties, Hb was selected as the representative example for the characterization of 3D nano-cylinder sensing behaviors.

For a quantitative comparison, both 2D ribbon sample and 3D assembled nano-cylinder sample were dipped into a 2.5 mg/mL Hb solution and later were dried out by air gun. The detailed system setup and process for SERS measurement is provided in Method. The collected Raman spectra show the prominent Hb fingerprints, such as 1127 cm^{-1} and 1583 cm^{-1}, on both the 2D ribbon and 3D nano-cylinders with plasmonic gaps (Figure 5.5 a). The peak of 1127 cm^{-1} belongs to the valine mode and the peak of 1583 cm^{-1} represents the phenylalanine mode. However, these two modes are significantly enhanced at the 3D plasmonic structures. A enhancement factor (EF) of ~ 10 is observed based on the ratio of Raman peak intensity at the plamonic gaps of 3D nano-cylinder (I_{3D}) over the peak intensity at 2D Au ribbons (I_{2D}). The enhancement are attributed to three factors:1), The nano-gaps formed during self-assembly are "hotspots" for SERS, which can confine the incident light near their surface, generating a enhanced electromagnetic field. The enhanced field directly contributes to higher EF with a relation of $EF \propto |E|^2$ [209], resulting in higher sensitivity. 2) The 3D cylindrical structure enable the fluid confinement inside its 3D nanoscale channel, which brings more target molecules close to the plasmonic sensing structures, further enhancing the sensitivity. 3) in addition, the suspended configuration of the 3D nanocylinder minimize the interaction between the sensing components with the Si substrate, leading to reduced energy loss through the substrate. The minimized energy loss also contributes to higher sensitivity.

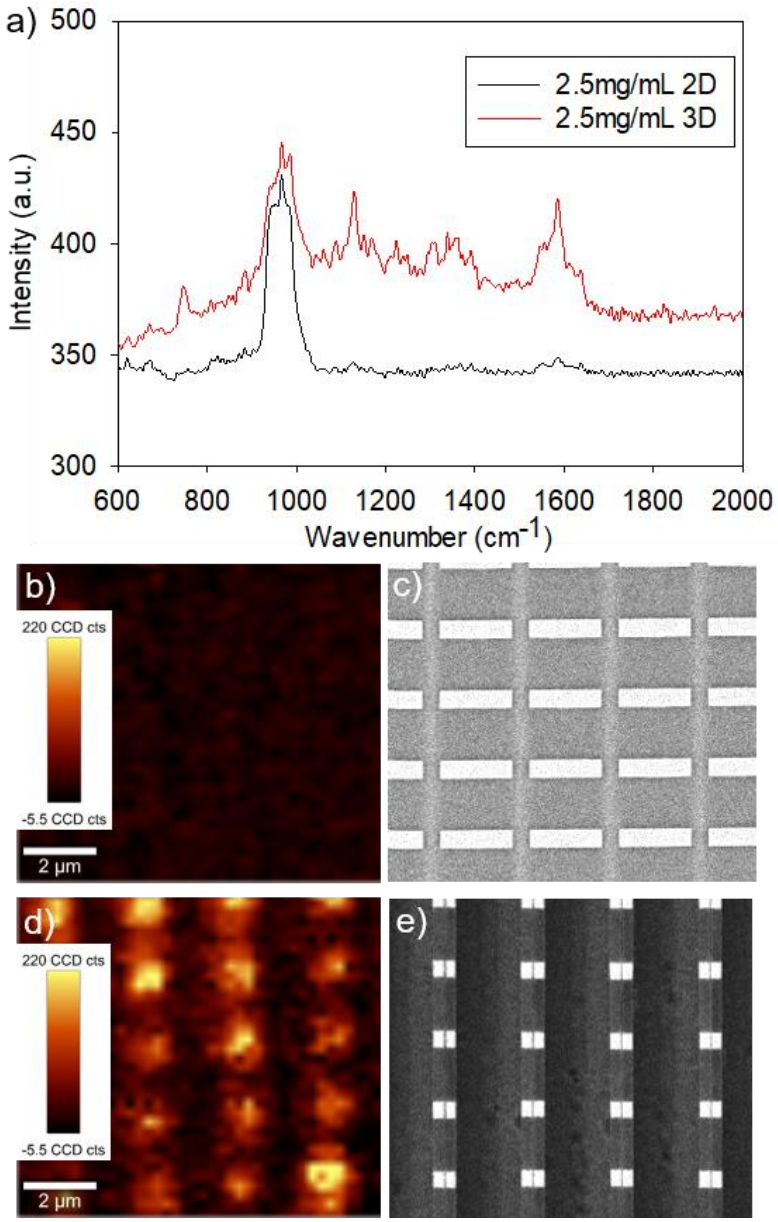

Figure 5.5 Raman analysis of hemoglobin. a) Raman spectra of hemoglobin from 2D ribbons before folding and 3D nano-cylinder with plasmonic gap. b) Raman Imaging collected on c) 2D ribbon sample based on the peak at 1600 cm-1. d) Raman Imaging collected on e) 3D nano-cylinder sample based on the peak at 1600 cm-1. Strong hotspot are observed around the plasmonic nanogap.

Further, to investigate the spatial performance of SERS, the laser was scanned over both the 2D and 3D sample areaw and Raman spectra were collected as a function of positions. Raman maps were generated based on the peak intensities of 1583 cm^{-1} that collected at each pixel (Figure 5.5 b, d). Clearly, the Raman peak intensities of the 3D cylindrical structure are much higher than that of 2D ribbons throughout the whole measurement area (Figure 5.5 b,d). Especially, the highest intensities are observed at the plamsonic nano-gaps, which are aligned well with the gaps shown in the SEM image (Figure 5.5 d, e). This coherence confirms that the nano-gaps are the hotspots, which are the main contributors for the high sensitivity. Moreover, the Raman mapping of the hotspots spread across the sample demonstrates the uniformity and reliability of the 3D nano-cylinder with plasmonic gaps for working as molecular sensors.

5.5 Quick Summary

In this chapter, I demonstrate a method to bridge nano-plasmonics with nano-fluidics using e-beam triggered self-assembly. Through self-assembly, the 2D ribbons with surface patterned Au structures curved up into nano-cylindrical channels and automatically formed Au plasmonic hotspots. The versatility of the fabrication techniques demonstrated by tuning the 2D design of Au patterns, achieving various shapes of plamsonic structures and channels. The integration of palsmonic nano-structures into a nanoscale channel makes it possible to achieve field enhancement and fluid confinement simultaneously. Further, the fluid confinement has been examined by fluorescent measurement, which confirms the capability of the biomolecules to flow into the channel and be confined within it. Finally,

the overall sensing behavior of the 3D nano-cylinder with plamsonic nano-gaps are characterized using SERS for the detection of hemoglobin. All of the prominent fingerprints are resolved in the spectra collected based on both the 2D and 3D nanostructures. Compared to the 2D patterns, higher sensitivity is observed on the 3D nano-cylinders, especially at the plasmonic nano-gaps, due to the combined advantage of field and fluid confinement.

Chapter6

Self-Assembled Graphene Nanocylinder for Plasmonic Optofluidic Sensors

In this chapter, I introduce the status and limitations of graphene plasmons achieved on 2D patterns. Driven by the advantages of 3D graphene plasmons, a self-assembly process for building 3D graphene based nanostructures is developed and presented in this chapter. The fabrications and Raman measurement is covered to characterize the morphology and quality of 3D graphene based structures. A comparison of 3D graphene plasmon to 2D graphene plasmon based on Comsol Multiphysics simulation is provided.

6.1 Graphene Plasmon

6.1.1 Introduction to Graphene Plasmon

The strong near-field enhancement of the incident light by the graphene plasmons exhibits potential for achieving optical detection mechanisms with higher sensitivity through stronger light-matter interaction [163, 166, 229-232]. Recently, several plasmonic sensing devices based on graphene nanostructures have been developed for detecting various targets such as chemical compounds [166, 233, 234], biomaterials [165], and gases [167]. Compared to conventional noble metal plasmonic sensing techniques, wide

frequency range [234,235-237] and high sensitivity [165] have been observed in graphene-based sensing technology.

6.1.2 Limitation of 2D Graphene

The plasmonic near-field enhancement of planar graphene undergoes severe exponential decay in the vertical direction away from the surface of the graphene [238], resulting in a relatively small spatial overlap between the specimens and the volume of high field confinement. Moreover, in the case of insulating substrates such as SiO_2 and h-BN, the planar 2D graphene plasmons couple strongly with the substrate surface polar phonons [239]. Due to the rapid spatial decay of plasmon enhanced electric field, the sensitivity is primarily limited by the diffusion of the targeted analytes to the graphene surface; thus, the configuration fails to achieve sensitivity in femto and atto molar ranges [240].

6.1.3 The advantages of 3D Graphene

To overcome the field intensity being limited to the graphene surface, transforming the two-dimensional (2D) planar graphene into three-dimensional (3D) nanostructures has been introduced as a promising solution [19, 69, 240-242]. When 2D planar graphene is transformed into 3D nanostructures, the plasmons exhibit new hybridized resonant modes that cannot be excited in the planar nanostructures [69]. The addition of extra dimensionality to the hybridized plasmon resonance modes results in a near-field enhancement which extends across the entire surface of these 3D structures as well as within their spatial volume [69]. As the sensitivity is directly related to the field intensity in the vicinity of the analyte, the strong volumetric electric field confinement in

these 3D nanostructures can result in high sensitivity detection of proteins and other biological specimens.

The plasmonic field extending over longer distances in 3D graphene-based nanostructures is also necessary to preserve molecular properties. When cells and biological molecules are tethered to planar 2D sensors, some biological functions and cellular conformational properties are lost due to geometric constraints [243]. Furthermore, the sensors need to allow for seamless integration with microfluidic channels and diverse materials for easy real-time monitoring of targeted specimens and incorporation into lab-on-chip devices, which can be achieved more readily with 3D nanostructures versus 2D ones. Among all the different types of 3D nanostructures, 3D hollow graphene nanocylinders offer the highest prospects due to the unique properties imparted by their morphology such as the large surface area to volume ratio. When biological specimens are encapsulated in cylinder-based lab-on-chip devices, functions such as mitosis are preserved [244], thereby making 3D nanocylinder-based sensors especially attractive. Impedance sensors based on rolled-up 3D sensors have shown to offer 4 orders of magnitude enhancement in the sensing capabilities for targeted H1N1 DNA specimens [245]. The unique properties of 3D nanocylinders, along with the ease of integration with microfluidic channels, has prompted research into their application for biological and chemical sensors [246, 247] and single cell analysis [248,249]. The incorporation of graphene along with noble metals in 3D geometries has recently been shown to achieve sub-molecular-level sensitivity of photocatalytic degradation process via optoplasmonic whispering-gallery-mode (WGM) resonance in the 3D cavities [250].

In this Chapter, we propose cylindrical graphene nanostructures and investigate

the effect of 3D geometry on the plasmonic properties of graphene, where a strong electric field spreads over large volumes inside the 3D nanostructures (Figure 6.1), for the realization of highly sensitive biomolecular sensors. The 3D graphene-based (cylindrical) sensors surpass the small surface-limited active areas existing in 2D graphene sensors and are significantly less susceptible to substrate influence as compared to 2D configurations (Figure 6.1d-f). A large array of graphene-based cylindrical structures is realized using a self-assembly process that offers halfway and fully curved cylindrical graphene structures suspended from a substrate by controlling the shape and dimension of the 2D structures before self-assembly (self-curving).

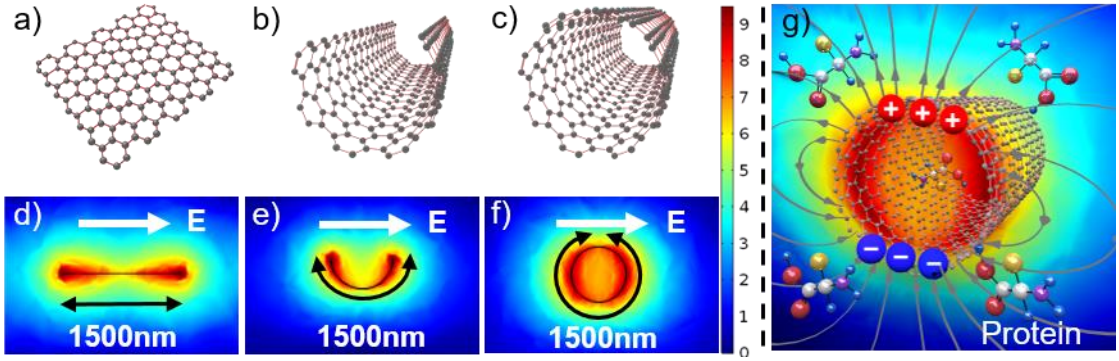

Figure 6.1 Schematic illustration of the transformation of a) 2D graphene ribbon, b) half-way curved graphene cylinder, and c) 3D graphene cylinders. d-f) Change in the electric field distribution as a result of curving of graphene structures. g) Schematic illustration showing the bio-sensing mechanism based on graphene nanocylinders. The color bar shows the value of the mapped electric-field enhancement in the graphene structures in natural log scale.

6.2 Realization of 3D Graphene-based Nanocylindrical Structures

6.2.1 Concept for Assembly of 3D Graphene Nanocylinders

The concepts involved in the self-curving of 3D graphene-based nanocylinders are illustrated in Figure 2. An array (30 × 100) of 2D graphene-based ribbons [3 nm thick aluminum oxide (Al_2O_3)/single layer CVD graphene/3 nm thick Al_2O_3/5nm tin (Sn)], each with dimensions of 1.5 μm × 15 μm, is first fabricated on a high resistivity silicon (Si) substrate. In the sandwiched structure, the two layers of Al_2O_3 work as frames supporting the graphene as well as protection layers, shielding the graphene from being damaged by the etching process during self-curving. The Sn layer is the actuation layer, generating surface tension forces for self-curving during the plasma triggered self-assembly process in a reactive ion etching (RIE) system (Figure 6.2a-c,). Note that the sample is immersed in nitric acid for 30min after assembly to selectively etch away the Sn layer. Then, it is transferred into IPA (isopropyl alcohol) and is gently dried out in a critical point dryer to minimize the effect of capillary force (Figure 6.2d). The RIE process releases the ribbons from the substrate while simultaneously inducing thermal energy because the Si etching reaction is exothermic [53]. As a result, the Sn grains melt and coalesce, which induces surface tension forces in the thin films [53,111], curving the 2D graphene-based ribbons out of plane to form partially (Figure 6.2b,f,j,n) and, with further self-assembly time, completely curved graphene-based nanocylinders (Figure 6.2c,g,k,o). A yield of self-curving has been achieved for 30 × 100 arrays (Figure 6.2e,f,g) and the yield is not affected by the number of arrays since the self-curving is a parallel process. Even after wet etching

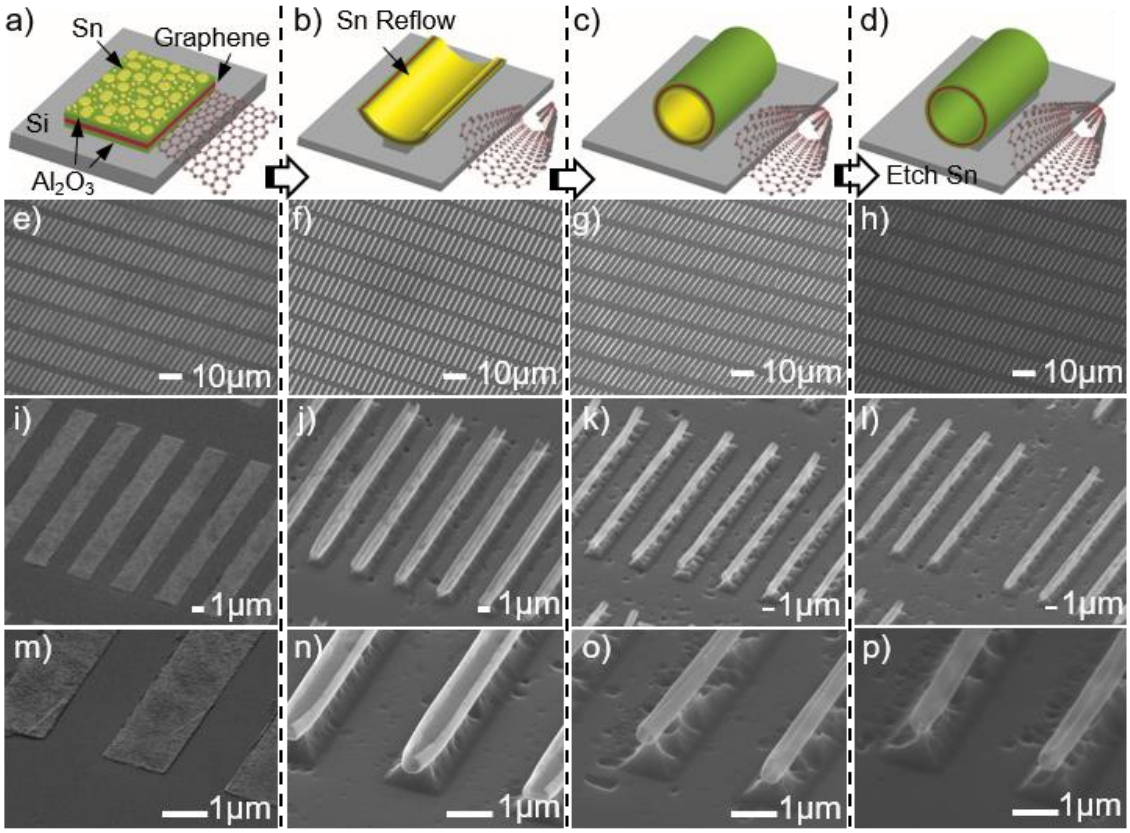

Figure 6.2. a-d) Conceptual schematics, e-p) SEM images, and q-u) Raman analysis of graphene-based ribbon, partially curved nanocylinder, and 3D nanocylinder triggered by reactive ion etching. a) The 2D graphene-based ribbon (Al2O3/ Graphene/ Al2O3/ Sn) is formed on a Si substrate. b, c) Reactive ion etching is used to release the 2D ribbon while simultaneously generating a surface tension force to curve the structure into b) partially and c) completely curved nanocylinders. d) After self-curving, the Sn layer is removed by nitric acid. The sample is carefully dried out by critical point dryer. e-p), The high yield of the self-curving process enables the assembly of an array (30 × 100) of nanocylinders, showing the ability to achieve large scale fabrication.

of Sn, most of the samples maintain their original cylindrical shapes (Figure 6.2h,f,p). Only the nanocylinders that fully released from the substrate during RIE are washed away (Figure 2f). The detailed fabrication process for the 3D graphene-based nanocylinders is described in the Section 6.2.2.

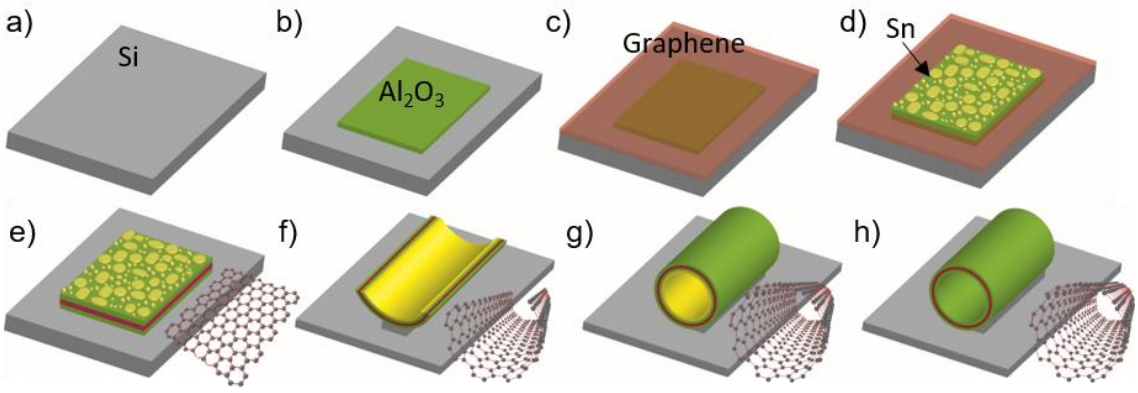

Figure 6.3 Conceptual schematics of the fabrication process of graphene-based ribbon, half-way folded nanocylinder, and 3D nanocylinder triggered by reactive ion etching. a-d) Schematics showing the fabrication of 2D ribbon contains 3 nm Al_2O_3/monolayer graphene/3 nm Al_2O_3/5nm Sn. e), The undesired Graphene is removed by oxygen plasma etching. f-g) After being treated in a reactive ion etching system, Sn film will melt and experience metal reflow due to the heat generation in etching process, which induce surface tension force to fold the 2D ribbons out of plane to be 3D half-way and completely curved nanocylinder. h) The Sn layer is removed by nitric acid and the nanocylinder is dried out by critical point dryer. The diameter of the nanocylinder is around 500 nm after self-assembly.

6.2.2 Sample Design and Fabrication

To fabricate the 3D graphene-based nanocylinders, 2D sandwiched graphene ribbon (3 nm thick Al_2O_3/single layer graphene/3 nm thick Al_2O_3/5 nm thick Sn) was first fabricated (Figure 6.3a-e). Polymethyl Methacrylate (PMMA) A3 was spun at 3000 RPM on top of the high resistivity Si substrate (560 – 840 Ω·cm) as the electron beam (E-beam) resist. An array of 2D ribbons, with ribbon dimensions of 1.5 μm × 15 μm, was then defined on the PMMA by an EBL system (Vistec EBPG5000+). After developing in MIBK (methyl isobutyl ketone): IPA (isopropyl alcohol) with the ratio of 1:3 for 1 minute, 3 nm thick Al_2O_3 was deposited by an electron beam evaporator (RME-E2000) to form the bottom protection layer (Figure 6.3b). A lift-off process was carried out in acetone to remove the undesired material. Next, a single layer of chemical vapor deposited (CVD) graphene was transferred on top of the patterned Al_2O_3 ribbon through a wet transfer process (Figure 6.3c). The mobility of the CVD graphene grown on the copper (Cu) foil is around 2700 cm2/V·s. After graphene transfer, N2403 was spun on top of the structure at 5000 RPM as the negative E-beam resist, which can protect graphene from electron irradiation for the rest of the EBL process. Then, a secondary array of 2D ribbons with the same ribbon dimensions (1.5 μm × 15 μm) was defined on the N2403 resist, which was aligned precisely to the bottom protection layer. MF-319 was used as the developer, which dissolved the unexposed resist in 1 minute. Then, 3 nm Al_2O_3 and 5 nm Sn layers were deposited by an electron beam evaporator to form the top protection layer and the sacrificial layer for inducing surface tension force, respectively (Figure 6.3d). Subsequently, the unwanted graphene areas, which were not protected by Sn and Al_2O_3, were removed by an oxygen plasma treatment in a reactive ion etching (RIE) system (STS 320) (Figure 6.3e). After

fabrication of 2D sandwiched graphene ribbons, RIE with CF_4/O_2 was used to achieve self-assembly of 3D nanocylinders (Figure 6.3f,g). During this process, both the chemical reaction between the fluorine atoms and the Si substrate and the physical ion bombardment on the Si substrate can contribute to etching the Si underneath the graphene sandwiched structures (Figure 6.3f,g). Finally, the graphene sandwiched structures were released from the substrate. Simultaneously, both the physical and chemical reactions generate thermal energy, which melts the Sn, triggering grain coalescence. As a result of grain coalescence, surface tension force was induced in the film, curving the 2D structure out-of-plane to form the 3D nanocylinders (Figure 6.3g). After self-assembly, the Sn layer could be etched way by immersing into a nitric acid for 30 minutes. To minimize the effect of the capillary force, the sample is transferred into IPA bath and gently dried out in a critical point dryer (CPdryer 915B) (Figure 6.3h).

6.2.3 Characterization of Graphene Quality and Tube Uniformity

A key objective of a successful self-curving process is the protection of the graphene. To verify the achievement of this goal, the properties of graphene before and after self-assembly are characterized by Raman spectroscopy (Figure 6.4a-e). In single layer graphene, the most prominent peaks are the G band (~1580 cm^{-1}) and 2D band (~2690 cm^{-1}) [162]. In the Raman spectra collected from the 2D graphene ribbons and the partially and completely curved graphene nanocylinders, both dominant peaks of graphene, G and 2D bands, are observed, proving that no critical damage is induced in the graphene (Figure 6.4e). After self-assembly, the D band (~1350 cm^{-1}) peak, representing defect and lattice disorder, appears and is stronger for samples with longer self-assembly times (Figure 6.4e).

In the 3D partially and completely curved graphene nanocylinders, the defects could be attributed to the increased density of edge defects and lattice disorder caused by stress or wrinkles induced during self-assembly. After self-curving, the edges of the ribbons curve towards the middle of the cylinder and cause a higher density of edge defects and lattice structural stress, leading to higher D band. To further quantify the defect level, the ratio of the D band intensity (I_D) and G band intensity (I_G), I_D/I_G, is calculated, which is around 1 (representing low defect regime [162]) for completely curved graphene nanocylinders. In addition, the I_D/I_G ratio of about 1 is comparable with a lithographically prepared graphene ribbon [252], which means the properties of graphene are not severely affected by the self-assembly process. Moreover, Raman images plotted based on G band are collected from samples consisting of entirely 2D graphene ribbons (Figure 6.2i), partially curved graphene nanocylinders (Figure 6.2j), and completed curved graphene nanocylinders (Figure 6.2k) to evaluate the overall graphene status throughout the structures (Figure 6.2m-o). For the 2D graphene ribbons (Figure 6.2i), the Raman mapping image shows ribbon structures with the same dimensions of 1.5 μm × 15 μm (Figure 6.4a), indicating the high quality of the fabricated 2D graphene ribbons. After partially curved, the structures in the Raman image (Figure 6.4b) have the same reduced width as the curved nanocylinders shown in the corresponding scanning electron microscopy (SEM) image (Figure 6.2j). When the graphene nanoribbons are completely curved (Figure 6.2k), a continuous clear Raman image with dimensions of around 477 nm × 15 μm is still observed (Figure 6.4c), demonstrating the physical properties of graphene are preserved during the self-assembly because of the graphene being sandwiched between two different 3 nm thick

layers of Al_2O_3. In addition, the effect of Sn etching on the graphene property is characterized by Raman image (Figure 6.4d) and Raman Spectrum (Figure 6.4e). The Raman image shows continuous shape that is similar to the nanocylinders after Sn etching (Figure 6.2l). Though the I_D/I_G ratio is slightly increased to 1.2, it still remains in the low defect regime. Both these two characterization results confirm the high quality of graphene after Sn removal process.

Further, the uniformity of the nanocylinders within the array is evaluated based on a previously developed method [251]. The diameter of seventy nanocylinders is measured and be plotted into a histogram (Figure. 6.4f). After applying Gaussian curve fitting, the full-width at half-maximum (FWHM) is used as the data to evaluate uniformity. Based on the measurement, FWHM is 16.6% for the array of the nanocylinders, which shows relative high uniformity.

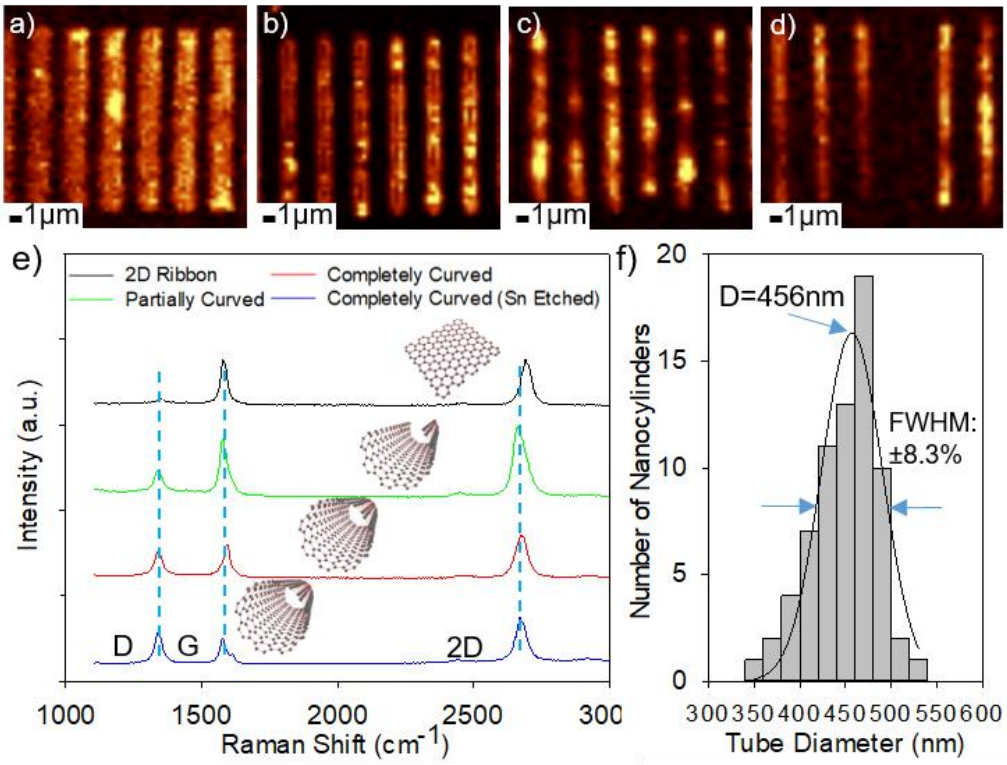

Figure 6.4 a-d) The property of graphene is characterized by Raman imaging based on G band (1590 cm-1) of a) the 2D graphene ribbon, b) partially curved cylinder, c) completely curved cylinder, d) completely curved cylinder after etching showing the same shape as the SEM image in Figure 6.2 (i-l). e) Raman spectrum shows that the two dominant peaks of graphene, G band (~1590 cm-1), and 2D band (~2680 cm-1), are preserved during self-curving, confirming the quality of the intrinsic graphene properties. f) Analysis of uniformity in cylinder diameters between different cylindrical structures on the same sample, the data is based on sampling the diameter for 70 nanocylinders.

6.2.4 Control of the Tube Shape

The shape of the self-assembled graphene-based nanostructure is further controlled via tuning the design of the 2D graphene structures. By patterning the 2D graphene ribbon with dimensions of 1.5 μm × 5 mm, graphene-based nanocylinders with a diameter of 477 nm and a high aspect ratio (ratio of the length to the diameter) of around 10,000 are achieved (Figure 6.5a-c). Even though the length of the self-assembled nanocylinders is in millimeter scale, the two edges closely touch each other throughout the entire length of the structure (Figure 6.5b,c), forming a uniform nanocylinder. To quantify the uniformity of the 5 mm long nanocylinders, Sixty of 1 μm long sections along the nanocylinders are taken as the sampling spot. The diameter of these sections is measured and be plotted into a histogram, which is then fitted by Gaussian curve (Figure 6.5d). The FWHM is used to evaluate the uniformity of the nanocylinder structure. FWHM of this long nanocylinder is 12%, which is 6% lower than the previous work [251]. This improvement can be attributed to the well-defined width of the 2D ribbon and the self-stopping mechanism induced by the touching of two edges. Moreover, this self-curving process is feasible for fabricating 3D graphene nanocylinders with various other dimensions. Excluding the limitations of the size of graphene sheets and the abilities of the electron beam lithography (EBL) process, there is no limit to the length of the 3D graphene nanocylinders. By increasing the length of the 2D design, 3D graphene nanocylinders with significantly higher aspect ratios can be further achieved. Furthermore, instead of mismatch of crystallographic direction [253], a new strategy for fabricating twisted graphene-based nanocylinders is demonstrated for the reflow induced self-curving process, which is designing 2D ribbons with beveled edges (Figure 6.5e inset). As the etching rate is isotropic

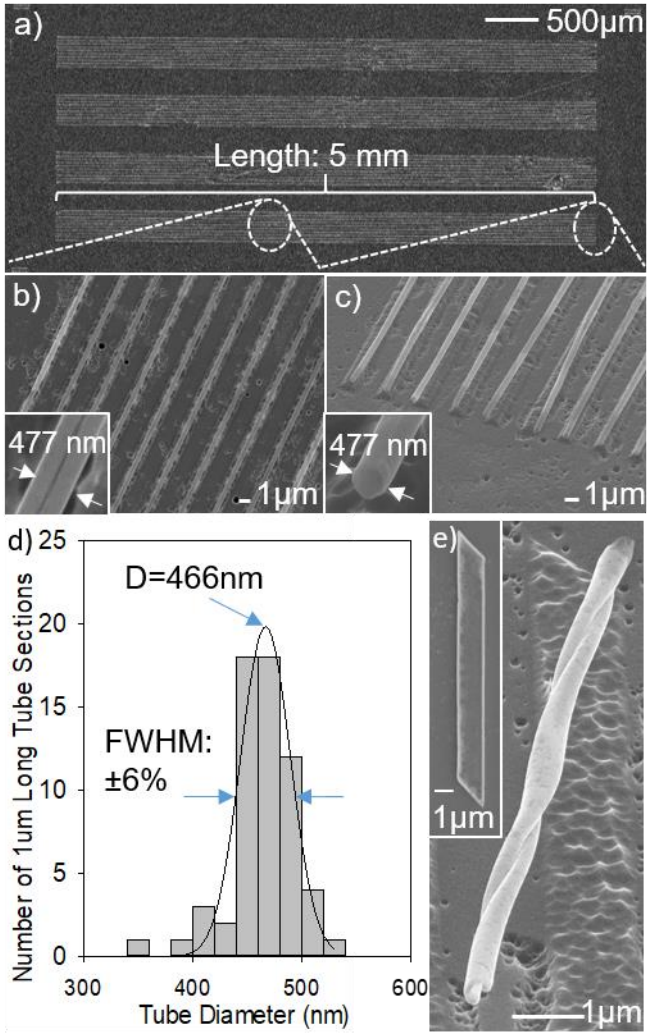

Figure 6.5 Self-assembly of graphene-based a-d) long and d) twisted nanocylinders. a) SEM image of the overview of the 5 mm long graphene-based nanocylinders with a diameter of 500 nm. b, c) SEM images showing the zoomed-in image of the middle and end of the long nanocylinder, demonstrating uniform self-assembly throughout the structure. d) Analysis of the uniformity of the 5 mm long nanocylinders showing a diameter (D) of 466 nm along the length of cylinder and a FWHM of 6%. e) SEM image of the graphene-based twisted nanocylinder before and after self-assembly. The narrow ends of the ribbon will be released prior to the release of the rest of the structure, folding first. Upon further etching, the folding trend is preserved to achieve the twisted structure.

along the outline of the 2D ribbons, the sharp corner is released and starts folding earlier. Thus, a diagonal folding trend is initiated from the sharp corner, which determines the folding direction of the whole structure. With further etching, the remainder of the graphene-based ribbon is released and folds up along the initial folding direction, resulting in a twisted graphene-based nanocylinder (Figure 6.5e). The asymmetrical twisted graphene cylinders are particularly attractive for chiral plasmonic optofluidic sensors that can provide more detailed information about chiral biological molecules such as proteins and amino acids than conventional achiral spectroscopy-based sensing techniques using planar graphene [218]. Note that, as most of the long and twisted nanocylinders are completely released from the substrate, Sn etching process is not applied to these samples. However, with additional components of holding area or structure, it should be able to maintain its structure after wet etching process.

6.3 Simulation of Plasmonic Behavior of Graphene Tube

The addition of an extra spatial degree of freedom to the 2D plasmonic graphene ribbons, drastically changes the localized surface plasmon resonances (LSPRs) in these structures, and consequently affects the associated near-field enhancement. The field enhancement at the resonance frequency directly controls the sensing capabilities of plasmonic sensors. Comsol Multiphysics was used to model the electromagnetic response of the 2D and 3D graphene structures. Graphene was modeled as a two-dimensional layer with surface conductivity as given by the Kubo formula. The fermi level of graphene was selected as 0.4 eV and the relaxation time was selected as 0.35 ps, these values were selected as reasonable approximation based on previous works with CVD graphene with

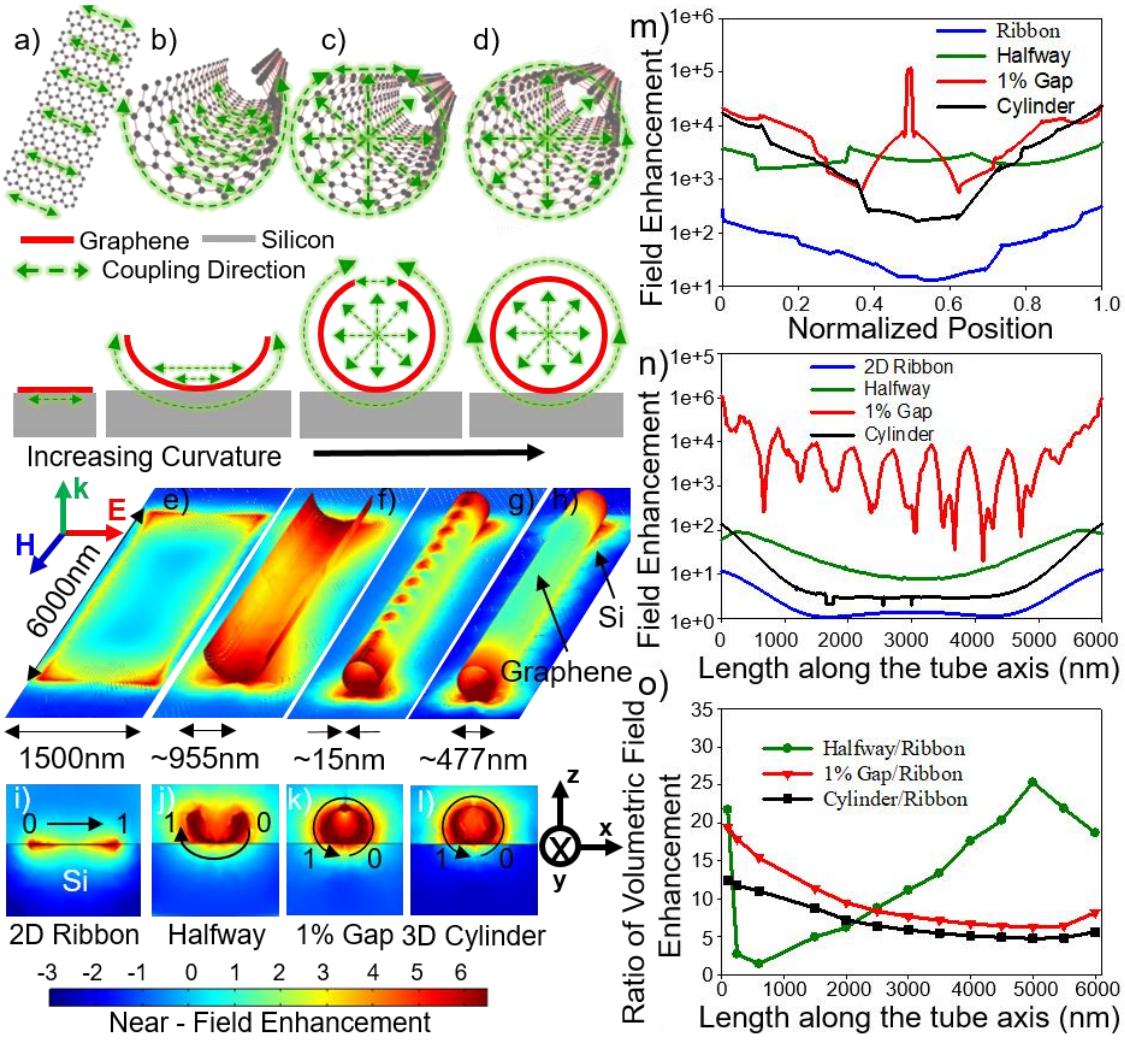

Figure 6.6. Schematics, and simulation results of the field enhancement in the graphene-based 2D ribbon, half-way curved cylinder, 1% gap cylinder, and completely curved nanocylinder at the frequencies of their geometric resonance. (a-d) 3D and cross-sectional schematics illustrating the coupling directions in 2D ribbons and 3D partially and completely curved cylinders. (e-h) The near-field enhancement plotted on the surface of a a) 2D ribbon, b, c) partially curved cylinders, and d) completely curved cylinders. i-l) The cross-section images show the field enhancement in the ZX plane when an imaginary cut plane is placed at the edge of the structures at 6000 nm. m) The field enhancement in ZX

plane along the circumference at the ends of the structures (see the black arrow in e-h)). n) The field enhancements at the center of the gap in the halfway and 1% gap curved cylinders, at the surface of the completely curved cylinder along an imaginary edge, and on the surface of the ribbon. The corresponding values of field enhancement are plotted for the entire length of the structure along structural edges overlapping with cut plane as shown by the black arrow in Supporting Information Figure S5e-h. A strong propagating mode is seen along the edge of the cylindrical structure with 1% gap. o) The volumetric field enhancements along the length of the 3D structures are analyzed based on their ratio to the volumetric field in a 2D graphene ribbon. Volumetric enhancement is calculated by volume integrals of the field inside the 3D structures and for an imaginary rectangular box of thickness 119 nm placed on the 2D ribbon with lengths increasing from 100 nm to 6 μm. For all the cases m-o), the 3D cylindrical structures show stronger field enhancement compared to the 2D ribbon. The primary geometric resonant frequencies for the ribbon, halfway, 1% gap, and completely curved nanocylinders in e-o were found to be 3.6, 7.7, 14.3, and 12.6 THz, respectively.

1000 cm^2/V-s mobility, 0.25-0.50 ps relaxation time and fermi levels of 0.3-0.5 eV [235, 254]. The frequencies of the LSPRs were determined from the transmission spectra of graphene structures (Figure 6.7a), and the resulting field enhancement at the resonant frequency were analyzed (Figure 6.6, Figure 6.7). As already shown in Figure 6.1d-f, the strong field enhancement at the edges of the 2D ribbon, is significantly modified in the case of curved 3D structures due to the increased field coupling between the opposite edges of the structures. For a 2D graphene ribbon with an incident plane wave, the strongest

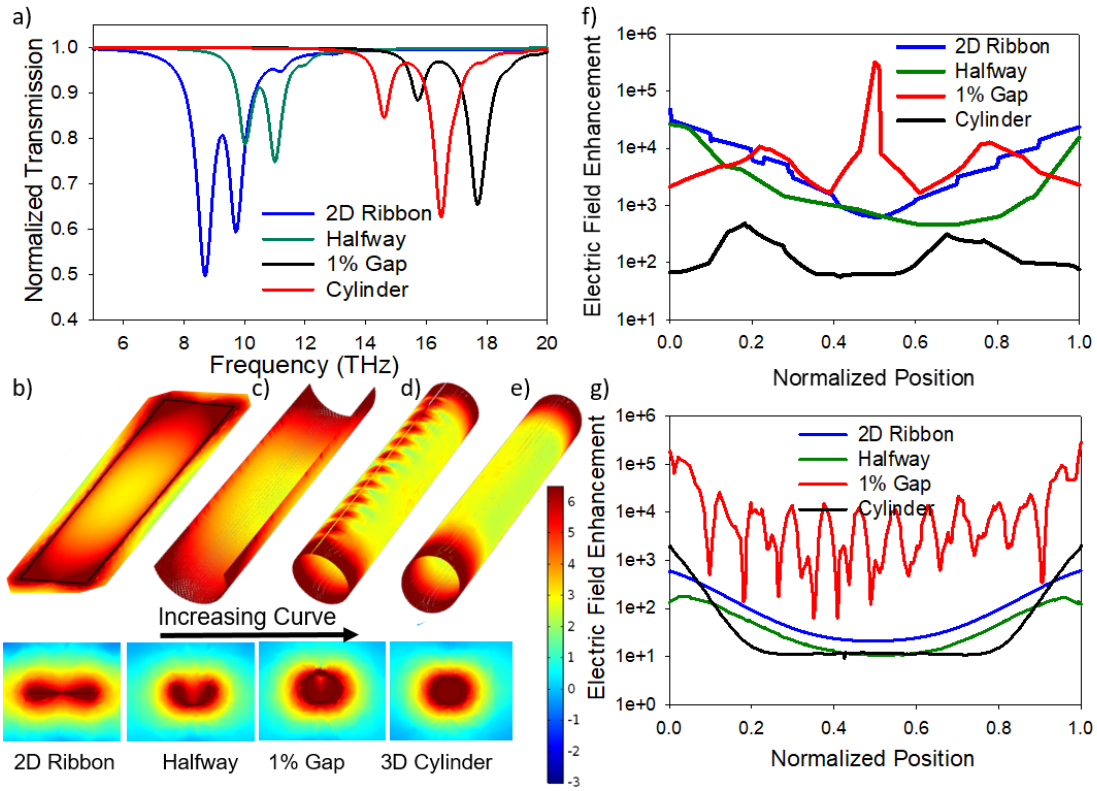

Figure 6.7. Simulation results of 2D and 3D graphene structures in vacuum. a) The normalized transmission through the structures. The self-assembly process causes a frequency shift in the resonance peak. b) Field enhancement plotted on the surface and cross-sectional planes for b) 2D ribbon, c) half-way curved cylinder, d) 1% gap cylinder, and e) completely curved 3D cylinder are simulated, showing the effect of geometry on field distribution and enhancement in graphene. f) Comparison of the field enhancement along the cross-sectional edge of the structures shown in c. g) Comparison of the field enhancement plotted at the center and along the length of the 2D ribbon and the 3D partially and completely curved structures. The normalized position is taken across the length and width of the structures similar to Figure 6.6.

fields exists at the edges of the 2D ribbon and decays exponentially across the surface of the ribbon (Figure 6.1d). Based on the polarization of incident E-field, the only coupling in 2D ribbons exists across the lateral edges (width) of the nanoribbon (Figure 6.6a); but, due to the large distance between the opposing corners of the ribbon, the field at the two corners cannot interact. As the curvature is increased to form partially curved cylinders, an additional coupling exists between opposing surfaces at the bottom of the cylinder due to the decreased gap between them (Figure 6.6b,c). Finally, at maximum curvature, two forms of field couplings are induced in 3D graphene cylinders (Figure 6.6d). Firstly, similar to 2D ribbons the plasmons along the entire circular edge (circumference) couple to neighboring points along the edge. Secondly, the small diameter of the cylinder allows the plasmon-generated field to couple across the opening to those points lying radially, horizontally, and vertically across the circumference. The simultaneous edge and radial coupling along the entire circumference forms a uniformly coupled mesh across the opening and causes the uniform cross-sectional field at the openings of the cylinder (Figure 6.1f). The effect of plasmon hybridization in 3D graphene nanocylinders is further accentuated when substrate effects are taken into account. Simulations were carried out for 2D and 3D graphene structures in vacuum (refractive index = 1) and a silicon (Si)-like 1.5 μm thick substrate (refractive index = 3.48). A strong degradation and localization of the plasmon near-field enhancement occurs due to the presence of the substrate, limiting the enhanced field to the corners of the ribbon only (Figure 6.6e,i), as opposed to 2D graphene in the vacuum where a uniformly decaying field can be seen across the surface of the ribbon (Figure 6.7b).

When 2D ribbons are curved, the spatial overlap of graphene with the

underlying substrates decreases, leading to a corresponding decrease in the substrate influence on the field enhancement. As a result, the partially (50% curved shown in Figure 6.6f,j and 99% curved shown in Figure 6.6g,k) and completely curved nanocylinder (Figure 6.6h,l) structures retain a stronger near-field enhancement spreading over a larger area, similar to freestanding graphene structures in vacuum (Figure 6.7c,d,e). For the 2D ribbon, the field enhancement at the edges ($\sim 3 \times 10^2$) is two orders of magnitude lower than the enhancement for a graphene ribbon in vacuum (Figure 6.7f,g), which further decays by an order of magnitude when moving to the center of the ribbon (Figure 6.6m blue line, with normalized position taken across the ribbon width as shown in Figure 6.6i). On the other hand, for the halfway curved nanocylinder, a line-type substrate contact (Figure 6.6f,j) leads to minimal spatial overlap, as opposed to 100% surface-area contact in 2D ribbons. The lower overlap with the substrate, stronger field coupling between the points on the circumference of the cylinder as well as radial field coupling across the nanoscale openings of the cylinder leads to an enhancement ($\sim 5.5 \times 10^3$) that is two orders of magnitude stronger than in 2D ribbon and remains constant across the width of the partially curved nanocylinder (Figure 4m green line, with normalized position taken along the semi-circular circumference as shown in Figure 6.6j). Similarly, the completely curved nanocylinder (Figure 4h) undergoes an even stronger ($\sim 2.3 \times 10^4$) enhancement, which is nearly two orders of magnitude stronger than for a nanocylinder in vacuum (Figure 6.7f,g), through additional localized enhancement occurring between the curved graphene and substrate alongside twice as much radial coupling along the circumference at the opening of the nanocylinder. The simultaneous localization and radial couplings give rise to a virtual cross-sectional area of strong field enhancement at the opening of the completely curved

nanocylinder (Figure 6.6l). The 3D plasmon couplings at the openings of the completely curved nanocylinders induce a total integrated edge enhancement of 1149, which is 13 times higher than the total field enhancement of 87 at the edge of the 2D ribbon. Moreover, the field enhancement induced in the 3D nanocylinder can be further modified via controlling the gap in the nanocylinder.

As shown in Figure 6.5b,c even for the completely curved nanocylinder structures, a sub-10 nm gap may exist between the two curved edges joining together which introduces the possibility of edge effects along the length of the structure. Simulations for the 99% curved nanocylinders (Figure 6.6g,k) reveal strong interactions between the two edges separated by a distance of only 15 nm that further enhances the coupled field at the center of the gap by an order of magnitude (Figure 6.6m, red line). It should be noted that inside the 15 nm gap of the 99% curved nanocylinder, the field enhancement is 300 times stronger than the maximum enhancement obtained even at the edge of the 2D ribbons (Figure 6.6m). The geometrically confined field in the partially curved nanocylinders exists along the entire length of the nanocylinders (Figure 6.6g).This leads to a field enhancement 4 orders of magnitude (Figure 6.6n, red line) stronger when compared to that at the center of the 2D ribbon (Figure 6.6n, blue line). Oscillations in the field strength, seen in Figure 6.6n (red line), indicate the highly confined propagating mode existing within the gap of the 99% curved nanocylinder. The strongly confined, high enhancement, propagating edge modes are particularly attractive for the development of graphene-based optoelectronic devices including plasmonic waveguides to achieve exceptional propagation lengths and figure of merit [255-257]. The completely curved nanocylinder does not show propagating modes, thus, supporting the conclusion that modes observed in the partially curved

nanocylinders are purely edge modes. However, at the center of the completely curved nanocylinders, even in the absence of the edge modes, the 3D coupling enables field enhancement that is an order of magnitude stronger than at the center of 2D ribbons. The strong uniform field enhancement at the openings of the nanocylinders induced by radial and edge couplings (Figure 6.6j-l) can also be termed as volumetric enhancement, which is computed as an integral of the field enhancement at the cross-section of the openings. The total volumetric enhancement for the uniform field in a halfway curved nanocylinder is 20 times higher than the volumetric field in 2D ribbons over the full length (6 μm) of the structures (Figure 6.6o, green line).

6.4 Vertical Aligned Graphene Tube for Optical Chirality

6.4.1 Introduction to Optical Chirality

Chirality is a geometric property of an object that does not have mirror symmetry [258]. Chiral geometries can result in various unique optical properties. For instance, circular dichroism, which refers to the differential absorption of left-handed polarized (LCP) and right-handed polarized (RCP) light, can be observed when linearly polarized light travel through a chiral structures. These unique optical properties have advances in various fields. One promising application lays in the study of biology and chemistry, where chirality widely exists. For example, molecules with different spatial configurations have distinctly different physiological responses to LCP and RCP signals.

Because of the unique properties and promising applications, artificial chiral structures have attracted great attention recently. Significant development has been

achieved in both theory and experiment. Au and Ag based nanostructures have been demonstrated to achieve optical chirality in visible spectral interval [259, 260]. However, it still remains challenging to achieve optical chirality in mid-infrared intervals, which brings great limitations for biological applications. This is because most of the vibrational modes of chiral biomolecules are located in mid-infrared intervals. Therefore, there is desperate need for realizing optical chirality in mid-infrared regime, which can contributes to enormous applications in biosensing and bioimaging. Graphene arise to be a strong candidate due to its unique plamson resonance regime. One graphene nanodisk array has demonstrated plasmonic circular dichroism in mid-infrared intervals, which can be potentially used for various biological applications [261].

6.4.2 Limitation of 2D Patterns for Chirality

Although mid-infrared plasmonic circular dichroism has been demonstrated in 2D graphene nanodisks, it typically requires strict oblique incidence, and the chiral responses are relatively weak. This limitation is because that optical chirality is based on the cross-coupling of electronic and magnetic dipoles in parallel directions [262]. In the case of normal incidence, the induced magnetic dipoles in 2D structures are along the incident direction and, thus, perpendicular to the direction of electric dipoles, which makes them uncoupled and results in the lack of chirality [79]. Therefore, 3D graphene vertical helices are desirable platforms for boosting the advantages of graphene chiral properties in mid-infrared intervals. Inspired by this theory, I have been working on fabricating 3D vertical graphene tubes (vertically aligned chiral nanostructures), in which we can define graphene helical patterns.

6.4.3 Attempt for Self-Assembly of Vertically Alligned Graphene Tubes

To achieve a vertical aligned tube, it requires two steps assembly (Figure 6.8a). First, the released ribbon should be folded into a tube structure as indicated by white arrow in Figure 6.8a. Next, the tube should be lifted up and rotate 90 degree (blue arrow in Figure 6.8a), forming the vertical tube (Figure 6.8b,c). This complicated assembly process can hardly be achieved without the assistance of real-time imaging. Therefore, I decided to use electron irradiation triggered assembly process as described in Chapter 4. 2D patterns that consist of 1 nm Cr, 3 nm Al_2O_3, 1 monolayer graphene, and 3 nm Al_2O_3 are defined through standard ebeam lithography and graphene wet transfer process. After being released by RIE process, the suspended 2D patterns (Figure 6.8a) are exposed under electron beam. The electron irradiation triggers crystallization of Al_2O_3, generating localized stress for self-assembly. By carefully tuning the irradiation area, the two-step assembly process can be achieved successfully, forming vertical tubes (Figure 6.8 b, c).

However, the long time exposure of the electron beam induces vast amount of defects and destroy the graphene. Based on the Raman Spectrum (Figure 6.9), none of the three graphene dominate peaks, D band at 1340 cm^{-1}, G band at 1580 cm^{-1}, and 2D band at 2680 cm^{-1}, can be observed on the assembled graphene vertical tube. This significant damage is caused by the long time electron irradiation. Further work on dose optimization may provide a method to solve this problem and preserve graphene properties.

Another potential strategy to achieve vertical aligned graphene tube without damage is to separate the two folding processes. The ribbon could be partially released first, which should still have small portion connected to the substrate. An invisible heating based

self-assembly process should be used first to trigger the self-assembly of tube (Figure 6.8a, white arrow). This folding process will self-stop when the two edges of the ribbon touch, forming a horizontally aligned tube on the substrate. Next, an additional RIE process should be carried out to fully release the tube structure. Then, the irradiation based in situ monitored process should be triggered to lift the tube up to be vertically aligned. The irradiation area can be confined to the end of the tube structure rather than the whole structures, minimizing the irradiation induced damage.

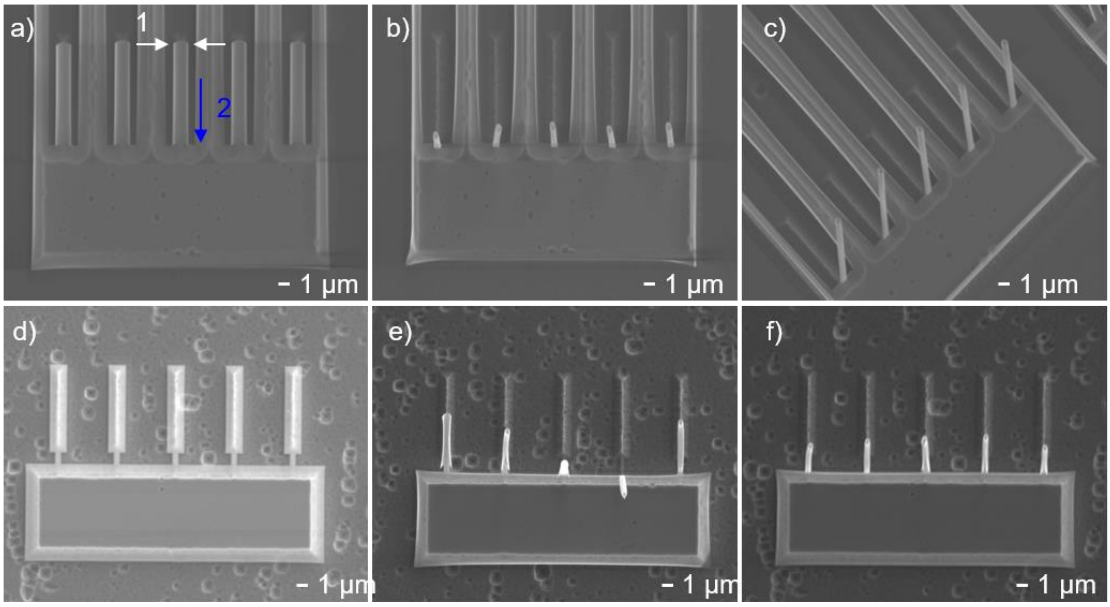

Figure 6.8 Self-assembly of vertical aligned tube. a-c) Vertical tube without graphene (1 nm Cr, 3 nm Al2O3). a) SEM of the 2D pattern before assembly. b), SEM image showing the vertical tube after assembly, and c) Tilted SEM image for the vertical tube. d-f) Vertical aligned Graphene Tube (1 nm Cr, 3 nm Al_2O_3, 1 monolayer graphene, and 3 nm Al_2O_3).

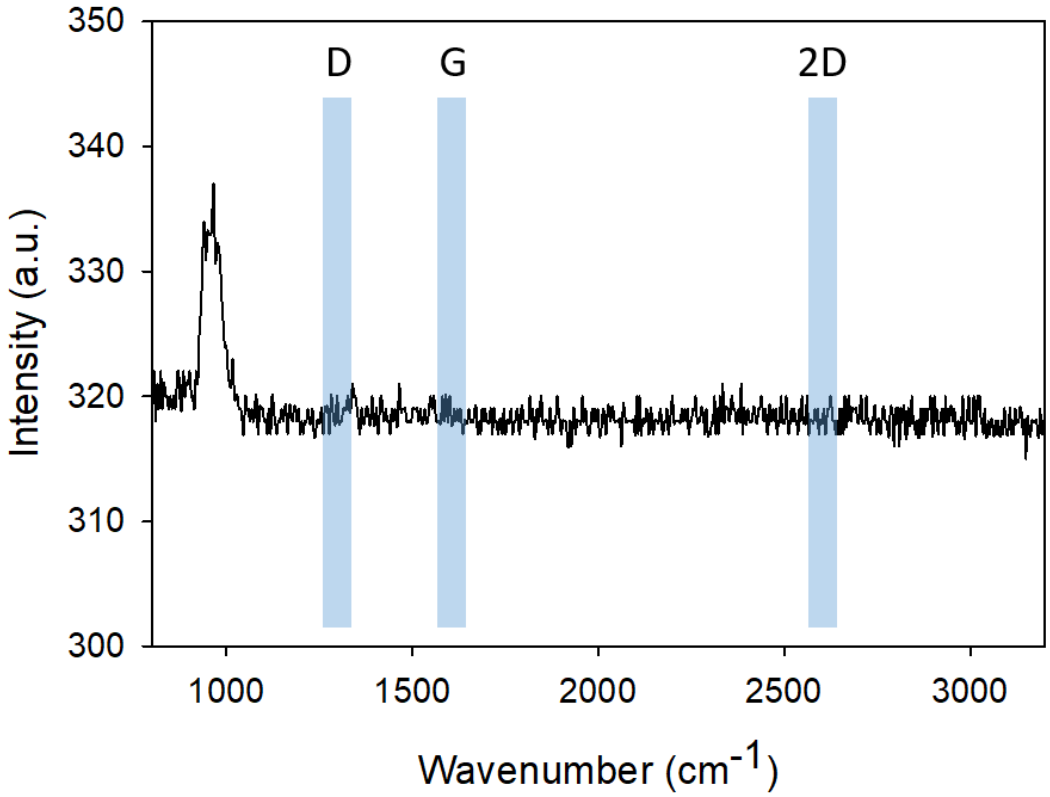

Figure 6.9 Raman spectrum of the graphene propreties on the assembled vertical aligned graphene tube.

6.5 Quick Summary

In this Chapter, I introduced a method for fabricating 3D graphene-based nanocylinders using a plasma triggered self-assembly process without sacrificing the unique physical properties of the 2D material. By designing the desired width, length, and shape of the graphene nanoribbons, graphene nanocylinders with an aspect ratio of 10,000 and twisted nanocylinders have been realized. The self-assembly process incorporates the physical properties of pristine graphene into the 3D architecture, which induces novel optical properties stemming from uniquely out-of-plane coupled plasmon modes that

cannot be observed in 2D structures defined on planar substrate. The radial coupling of plasmons induces a uniform circular cross-sectional area of extreme near-field enhancement at the openings of the 3D nanocylinders. The edge-edge coupling and edge-substrate coupling with minimal spatial contact between the graphene and the substrate in the partially curved graphene nanocylinders induce a propagating edge mode throughout the length of the cylinders with an electric field that is 4 orders of magnitude stronger than in the 2D ribbons.

Chapter7

Conclusion

In this thesis, novel energetic irradiation (plasma, ion, and electron) triggered in situ monitored self-assembly processes are presented. This approach demonstrates precise motion control of structures in nanoscale, making it possible to achieve intricate 3D nanostructures with advance physical and chemical properties. The interactions between the irradiation and responsive materials, such as Sn, Al_2O_3, and polymer, are investigated. The responsive materials experience significant phase change, such as grain coalescence, crystallization, and reflow, under the energetic irradiation, which generate localized stress for self-assembly. The deeper understanding of the driving force of self-assembly contributes to better control of this dynamic process to achieve well-defined 3D nanostructures with desired configurations. Especially, the ion and electron beam are demonstrated to have the ability to simultaneously induce localized stress and provide real time imaging, making it possible to achieve in situ monitored self-assembly. The visualization of nanoscale assembly together with the controllable ion or electron beam significantly increase the yield up to almost 100%. Further, assisted by the design of 2D patterns or material layouts, sequential and reversible assembly are demonstrated in nanoscale. During these processes, electron irradiation works as “hands” to manipulate motion of nanostructures with desired order. By assigning each single assembly step in a particular order, localized motion can be selectively triggered with perfect timing, making

a component accurately integrate into the complex 3D structure without disturbing other parts of the assembly process. Moreover, by changing the voltage of electron beam, the focal plane can be precisely tuned from the top to bottom surface of a thin film. The repeat change of irradiation focal plane cause the movement of stimuli and finally lead to reversible self-assembly. The programmable sequential and reversible self-assembly open the possibility to various applications such as nanomachine and advanced optical devices.

The advantages of 3D nanostructures have been explored in two applications: gap-based Au plasmonic cylindrical nanosensors and graphene nanocylindrical plasmonic optofluidic sensors. In the gap-based Au plasmonic cylindrical nanosensors, the automatically formed Au nanogap during self-assembly is used as the plasmonic hotspot for sensing. It is able to efficiently confine the light near the gap and create an area with higher electromagnetic field. Further, the cylinderical structure can work as a nanofluidic channel which can passively confine the biomolecules near the gap. The combined advantages of light and fluid confinement have been demonstrated to achieve higher sensitivity for detecting hemoglobin. In the graphene nanocylindrical plasmonic optofluidic sensors, the 2D graphene structure is folded into a 3D nanoclyinder, forming a 3D nanocavity. The 3D formats enable unique graphene plamon hybridization, leading to volumetric light confinement. Simulation results demonstrate that 3D graphene nanocylinder can achieve an electric field that is 4 orders of magnitude stronger than in the 2D ribbons.

The continuous study of in situ monitored self-assembly gives us more opportunities to control the motion of matters in small scale, which could trigger innovation

of advanced 3D fabrication techniques. With further understanding of the irradiation-atom interaction, it is possible to program the movement of single atoms, allowing highly precise 3D fabrication with single atoms resolution. In addition, these self-assembled intricate architectures will be beneficial for exploring the advanced properties in nano-optics, nano-electronics, and nano-mechanics.

Bibliography

[1] Beech, R. (2009). The Practical Illustrated Encyclopaedia of Origami. Lorenz Books.

[2] Shafer, J. (2001). Origami to Astonish and Amuse. St. Martin's Griffin.

[3] Fox, M. (2005, April 2). Akira Yoshizawa, 94, Modern Origami Master. New York Times.

[4] Harbin, R. (1974) Origami: A Step-by-Step Guide, Hamlyn, London.

[5] Lang, R. J. (2003). Origami Design Secrets. Dover Publications.

[6] Feynman, Richard, R. (2018). There's plenty of room at the bottom: An invitation to enter a new field of physics. Handbook of Nanoscience, Engineering, and Technology , pp. 26-35.

[7] Jacak, L., Hawrylak, P., & Wojs, A. (2013). Quantum Dots. Springer Science & Business Media.

[8] An, K., & Hyeon, T. (2009). Synthesis and biomedical applications of hollow nanostructures. Nano Today, 4(4), 359-373.

[9] Eckford, A. W. (2007). Nanoscale communication with brownian motion. Paper presented at the 2007 41st Annual Conference on Information Sciences and Systems, pp. 160-165.

[10] Petryayeva, E., & Krull, U. J. (2011). Localized surface plasmon resonance: Nanostructures, bioassays and biosensing—A review. Analytica Chimica Acta, 706(1), 8-24.

[11] Nagpal, P., Lindquist, N. C., Oh, S. H., & Norris, D. J. (2009). Ultrasmooth patterned metals for plasmonics and metamaterials. Science (New York, N.Y.), 325(5940), 594-597. doi:10.1126/science.1174655 [doi]

[12] Vázquez-Guardado, A., Barkam, S., Peppler, M., Biswas, A., Dennis, W., Das, S., et al. (2018). Enzyme-free plasmonic biosensor for direct detection of neurotransmitter dopamine from whole blood. Nano Letters, 19(1), 449-454.

[13] Huck, C., Neubrech, F., Vogt, J., Toma, A., Gerbert, D., Katzmann, J., et al. (2014). Surface-enhanced infrared spectroscopy using nanometer-sized gaps. Acs Nano, 8(5), 4908-4914.

[14] Im, H., Bantz, K. C., Lindquist, N. C., Haynes, C. L., & Oh, S. (2010). Vertically oriented sub-10-nm plasmonic nanogap arrays. Nano Letters, 10(6), 2231-2236.

[15] Chen, C., Mohr, D. A., Choi, H., Yoo, D., Li, M., & Oh, S. (2018). Waveguide-integrated compact plasmonic resonators for on-chip mid-infrared laser spectroscopy. Nano Letters, 18(12), 7601-7608.

[16] Im, H., Bantz, K. C., Lee, S. H., Johnson, T. W., Haynes, C. L., & Oh, S. (2013). Self‐assembled plasmonic nanoring cavity arrays for SERS and LSPR biosensing. Advanced Materials, 25(19), 2678-2685.

[17] Lal, S., Link, S., & Halas, N. J. (2007). Nano-optics from sensing to waveguiding. Nature Photonics, 1(11), 641.

[18] Tinguely, J., Sow, I., Leiner, C., Grand, J., Hohenau, A., Felidj, N., et al. (2011). Gold nanoparticles for plasmonic biosensing: The role of metal crystallinity and nanoscale roughness. Bionanoscience, 1(4), 128-135.

[19] Leem, J., Wang, M. C., Kang, P., & Nam, S. (2015). Mechanically self-assembled, three-dimensional graphene–gold hybrid nanostructures for advanced nanoplasmonic sensors. Nano Letters, 15(11), 7684-7690.

[20] Zhao, Y., Saleh, A. A., Van De Haar, Marie Anne, Baum, B., Briggs, J. A., Lay, A., et al. (2017). Nanoscopic control and quantification of enantioselective optical forces. Nature Nanotechnology, 12(11), 1055.

[21] Gracias, D. H., Tien, J., Breen, T. L., Hsu, C., & Whitesides, G. M. (2000). Forming electrical networks in three dimensions by self-assembly. Science (New York, N.Y.), 289(5482), 1170-1172. doi:8753 [pii]

[22] Martinez, R. V., Fish, C. R., Chen, X., & Whitesides, G. M. (2012). Elastomeric origami: Programmable paper ‐ elastomer composites as pneumatic actuators. Advanced Functional Materials, 22(7), 1376-1384.

[23] Lu, Y., & Kim, C. (2006). Microhand for biological applications. Applied Physics Letters, 89(16), 164101.

[24] Kusuda, S., Sawano, S., & Konishi, S. (2007). Fluid-resistive bending sensor having perfect compatibility with flexible pneumatic balloon actuator. Paper presented at the 2007 IEEE 20th International Conference on Micro Electro Mechanical Systems (MEMS), pp. 615-618.

[25] Liu, Y., Takafuji, M., Ihara, H., Zhu, M., Yang, M., Gu, K., et al. (2012). Programmable responsive shaping behavior induced by visible multi-dimensional gradients of magnetic nanoparticles. Soft Matter, 8(12), 3295-3299.

[26] Boncheva, M., Andreev, S. A., Mahadevan, L., Winkleman, A., Reichman, D. R., Prentiss, M. G., et al. (2005). Magnetic self-assembly of three-dimensional surfaces from planar sheets. Proceedings of the National Academy of Sciences, 102(11), 3924-3929.

[27] In, H. J., Lee, H., Nichol, A. J., Kim, S., & Barbastathis, G. (2008). Carbon nanotube–based magnetic actuation of origami membranes. Journal of Vacuum Science & Technology B: Microelectronics and Nanometer Structures Processing, Measurement, and Phenomena, 26(6), 2509-2512.

[28] Iwase, E., & Shimoyama, I. (2005). Multistep sequential batch assembly of three-dimensional ferromagnetic microstructures with elastic hinges. Journal of Microelectromechanical Systems, 14(6), 1265-1271.

[29] Lee, H., Xia, C., & Fang, N. X. (2010). First jump of microgel; actuation speed enhancement by elastic instability. Soft Matter, 6(18), 4342-4345.

[30] Ma, Y., Zhang, Y., Wu, B., Sun, W., Li, Z., & Sun, J. (2011). Polyelectrolyte multilayer films for building energetic walking devices. Angewandte Chemie International Edition, 50(28), 6254-6257.

[31] Ma, C., Li, T., Zhao, Q., Yang, X., Wu, J., Luo, Y., et al. (2014). Supramolecular lego assembly towards Three‐Dimensional Multi‐Responsive hydrogels. Advanced Materials, 26(32), 5665-5669.

[32] Brannon-Peppas, L., & Peppas, N. A. (1991). Equilibrium swelling behavior of pH-sensitive hydrogels. Chemical Engineering Science, 46(3), 715-722.

[33] Luo, J., Huang, R., He, J., Fu, Y. Q., Flewitt, A., Spearing, S., et al. (2006). Modelling and fabrication of low operation temperature microcages with a polymer/metal/DLC trilayer structure. Sensors and Actuators A: Physical, 132(1), 346-353.

[34] Luo, J., He, J., Fu, Y. Q., Flewitt, A., Spearing, S., Fleck, N., et al. (2005). Fabrication and characterization of diamond-like carbon/Ni bimorph normally closed microcages. Journal of Micromechanics and Microengineering, 15(8), 1406.

[35] Malachowski, K., Breger, J., Kwag, H. R., Wang, M. O., Fisher, J. P., Selaru, F. M., et al. (2014). Stimuli‐responsive theragrippers for chemomechanical controlled release. Angewandte Chemie International Edition, 53(31), 8045-8049.

[36] Leong, T. G., Lester, P. A., Koh, T. L., Call, E. K., & Gracias, D. H. (2007). Surface tension-driven self-folding polyhedra. Langmuir, 23(17), 8747-8751.

[37] Cho, J., Azam, A., & Gracias, D. H. (2010). Three dimensional nanofabrication using surface forces. Langmuir, 26(21), 16534-16539.

[38] Zhang, L., Liang, H., Jacob, J., & Naumov, P. (2015). Photogated humidity-driven motility. Nature Communications, 6, 7429.

[39] Ikeda, T., Nakano, M., Yu, Y., Tsutsumi, O., & Kanazawa, A. (2003). Anisotropic bending and unbending behavior of azobenzene liquid‐crystalline gels by light exposure. Advanced Materials, 15(3), 201-205.

[40] Lendlein, A., & Langer, R. (2002). Biodegradable, elastic shape-memory polymers for potential biomedical applications. Science (New York, N.Y.), 296(5573), 1673-1676. doi:10.1126/science.1066102

[41] Bassik, N., Stern, G. M., & Gracias, D. H. (2009). Microassembly based on hands free origami with bidirectional curvature. Applied Physics Letters, 95(9), 091901.

[42] Leong, T. G., Benson, B. R., Call, E. K., & Gracias, D. H. (2008). Thin film stress driven self‐folding of microstructured containers. Small, 4(10), 1605-1609.

[43] Leong, T. G., Randall, C. L., Benson, B. R., Zarafshar, A. M., & Gracias, D. H. (2008). Self-loading lithographically structured microcontainers: 3D patterned, mobile microwells. Lab on a Chip, 8(10), 1621-1624.

[44] Ebefors, T., Kälvesten, E., & Stemme, G. (1998). Dynamic actuation of polyimide V-groove joints by electrical heating. Sensors and Actuators A: Physical, 67(1-3), 199-204.

[45] Feinberg, A. W., Feigel, A., Shevkoplyas, S. S., Sheehy, S., Whitesides, G. M., & Parker, K. K. (2007). Muscular thin films for building actuators and powering devices. Science (New York, N.Y.), 317(5843), 1366-1370. doi:317/5843/1366

[46] Xi, J., Schmidt, J. J., & Montemagno, C. D. (2005). Self-assembled microdevices driven by muscle. Nature Materials, 4(2), 180-184.

[47] Kuribayashi, K., Onoe, H., & Takeuchi, S. (2009). Assembly of 3d microstructures powered by cells. Paper presented at the Thirteenth International Conference on Miniaturized Systems for Chemistry and Life Sciences, pp. 1321-1323.

[48] Sandhu, A. (2006). Who invented nano? Nature Nanotechnology, 1(2), 87.

[49] Binnig, G., & Rohrer, H. (1983). Scanning tunneling microscopy. Surface Science, 126(1-3), 236-244.

[50] Cho, J., James, T., & Gracias, D. H. (2010). Curving nanostructures using extrinsic stress. Advanced Materials, 22(21), 2320-2324.

[51] Gracias, D. H., & Cho, J. (2012). Self-Assembly of Lithographically Patterned Polyhedral Nanostructures and Formation of Curving Nanostructures

[52] Cho, J., Datta, D., Park, S., Shenoy, V. B., & Gracias, D. H. (2010). Plastic deformation drives wrinkling, saddling, and wedging of annular bilayer nanostructures. Nano Letters, 10(12), 5098-5102.

[53] Dai, C., Joung, D., & Cho, J. (2017). Plasma triggered grain coalescence for self-assembly of 3D nanostructures. Nano-Micro Letters, 9(3), 27.

[54] Tyagi, P., Bassik, N., Leong, T. G., Cho, J., Benson, B. R., & Gracias, D. H. (2009). Self-assembly based on chromium/copper bilayers. Journal of Microelectromechanical Systems, 18(4), 784-791.

[55] Rykaczewski, K., Hildreth, O. J., Wong, C. P., Fedorov, A. G., & Scott, J. H. J. (2011). Guided three-dimensional catalyst folding during metal-assisted chemical etching of silicon. Nano Letters, 11(6), 2369-2374.

[56] Li, X. (2008). Strain induced semiconductor nanotubes: From formation process to device applications. Journal of Physics D: Applied Physics, 41(19), 193001.

[57] Chun, I. S., Challa, A., Derickson, B., Hsia, K. J., & Li, X. (2010). Geometry effect on the strain-induced self-rolling of semiconductor membranes. Nano Letters, 10(10), 3927-3932.

[58] Barcelos, I. D., Moura, L. G., Lacerda, R. G., & Malachias, A. (2014). Observation of strain-free rolled-up CVD graphene single layers: Toward unstrained heterostructures. Nano Letters, 14(7), 3919-3924.

[59] Chen, Z., Huang, G., Trase, I., Han, X., & Mei, Y. (2016). Mechanical self-assembly of a strain-engineered flexible layer: Wrinkling, rolling, and twisting. Physical Review Applied, 5(1), 017001.

[60] Mei, Y., Kiravittaya, S., Benyoucef, M., Thurmer, D. J., Zander, T., Deneke, C., et al. (2007). Optical properties of a wrinkled nanomembrane with embedded quantum well. Nano Letters, 7(6), 1676-1679.

[61] Prinz, V. Y. (2003). A new concept in fabricating building blocks for nanoelectronic and nanomechanic devices. Microelectronic Engineering, 69(2-4), 466-475.

[62] Douglas, S. M., Dietz, H., Liedl, T., Högberg, B., Graf, F., & Shih, W. M. (2009). Self-assembly of DNA into nanoscale three-dimensional shapes. Nature, 459(7245), 414-418.

[63] He, Y., Ye, T., Su, M., Zhang, C., Ribbe, A. E., Jiang, W., et al. (2008). Hierarchical self-assembly of DNA into symmetric supramolecular polyhedra. Nature, 452(7184), 198-201.

[64] Andersen, E. S., Dong, M., Nielsen, M. M., Jahn, K., Subramani, R., Mamdouh, W., et al. (2009). Self-assembly of a nanoscale DNA box with a controllable lid. Nature, 459(7243), 73-76.

[65] Han, D., Pal, S., Nangreave, J., Deng, Z., Liu, Y., & Yan, H. (2011). DNA origami with complex curvatures in three-dimensional space. Science (New York, N.Y.), 332(6027), 342-346. doi:10.1126/science.1202998

[66] Zhang, T., Hartl, C., Frank, K., Heuer‐Jungemann, A., Fischer, S., Nickels, P. C., et al. (2018). 3D DNA origami crystals. Advanced Materials, 30(28), 1800273.

[67] Shen, X., Song, C., Wang, J., Shi, D., Wang, Z., Liu, N., et al. (2012). Rolling up gold nanoparticle-dressed DNA origami into three-dimensional plasmonic chiral nanostructures. Journal of the American Chemical Society, 134(1), 146-149.

[68] Shen, X., Asenjo-Garcia, A., Liu, Q., Jiang, Q., García de Abajo, F Javier, Liu, N., et al. (2013). Three-dimensional plasmonic chiral tetramers assembled by DNA origami. Nano Letters, 13(5), 2128-2133.

[69] Joung, D., Nemilentsau, A., Agarwal, K., Dai, C., Liu, C., Su, Q., et al. (2017). Self-assembled three-dimensional graphene-based polyhedrons inducing volumetric light confinement. Nano Letters, 17(3), 1987-1994.

[70] Karnaushenko, D., Karnaushenko, D. D., Makarov, D., Baunack, S., Schäfer, R., & Schmidt, O. G. (2015). Self‐Assembled On‐Chip‐Integrated giant Magneto‐Impedance sensorics. Advanced Materials, 27(42), 6582-6589.

[71] Leong, T. G., Randall, C. L., Benson, B. R., Bassik, N., Stern, G. M., & Gracias, D. H. (2009). Tetherless thermobiochemically actuated microgrippers. Proceedings of the National Academy of Sciences of the United States of America, 106(3), 703-708. doi:10.1073/pnas.0807698106

[72] Lee, W., Jung, W., Rhee, D., Hu, J., Lee, Y. L., Jacobson, C., et al. (2018). Monolithic polymer nanoridges with programmable wetting transitions. Advanced Materials, 30(32), 1706657.

[73] Lee, W., Jung, W., Nagel, S. R., & Odom, T. W. (2016). Stretchable superhydrophobicity from monolithic, three-dimensional hierarchical wrinkles. Nano Letters, 16(6), 3774-3779.

[74] Lee, W., Engel, C. J., Huntington, M. D., Hu, J., & Odom, T. W. (2015). Controlled three-dimensional hierarchical structuring by memory-based, sequential wrinkling. Nano Letters, 15(8), 5624-5629.

[75] Rhee, D., Lee, W., & Odom, T. W. (2017). Crack‐Free, soft wrinkles enable switchable anisotropic wetting. Angewandte Chemie, 129(23), 6623-6627.

[76] Chu, K., Xiao, R., & Wang, E. N. (2010). Uni-directional liquid spreading on asymmetric nanostructured surfaces. Nature Materials, 9(5), 413-417.

[77] Cho, J., Keung, M. D., Verellen, N., Lagae, L., Moshchalkov, V. V., Van Dorpe, P., et al. (2011). Nanoscale origami for 3D optics. Small, 7(14), 1943-1948.

[78] Chen, C., Ishikawa, A., Tang, Y., Shiao, M., Tsai, D. P., & Tanaka, T. (2015). Uniaxial‐isotropic metamaterials by Three‐Dimensional Split‐Ring resonators. Advanced Optical Materials, 3(1), 44-48.

[79] Liu, Z., Du, H., Li, J., Lu, L., Li, Z., & Fang, N. X. (2018). Nano-kirigami with giant optical chirality. Science Advances, 4(7), eaat4436.

[80] Moritake, Y., & Tanaka, T. (2018). Bi-anisotropic fano resonance in three-dimensional metamaterials. Scientific Reports, 8(1), 1-8

[81] Liu, Z., Du, S., Cui, A., Li, Z., Fan, Y., Chen, S., et al. (2017). High‐Quality‐Factor Mid‐Infrared toroidal excitation in folded 3D metamaterials. Advanced Materials, 29(17), 1606298.

[82] Mao, Y., Pan, Y., Zhang, W., Zhu, R., Xu, J., & Wu, W. (2016). Multi-direction-tunable three-dimensional meta-atoms for reversible switching between midwave and long-wave infrared regimes. Nano Letters, 16(11), 7025-7029.

[83] Mao, Y., Zheng, Y., Li, C., Guo, L., Pan, Y., Zhu, R., et al. (2017). Programmable bidirectional folding of metallic thin films for 3D chiral optical antennas. Advanced Materials, 29(19), 1606482.

[84] Agarwal, K., Dai, C., Joung, D., & Cho, J. (2018). Nano-architecture driven plasmonic field enhancement in 3D graphene structures. ACS Nano, 13(2), 1050-1059.

[85] Endo, M., & Sugiyama, H. (2018). DNA origami nanomachines. Molecules, 23(7), 1766.

[86] Song, C., Wang, Z., & Ding, B. (2013). Smart nanomachines based on DNA self‐assembly. Small, 9(14), 2382-2392.

[87] Xu, B., Zhang, B., Wang, L., Huang, G., & Mei, Y. (2018). Tubular micro/nanomachines: From the basics to recent advances. Advanced Functional Materials, 28(25), 1705872.

[88] Zhang, L., Abbott, J. J., Dong, L., Peyer, K. E., Kratochvil, B. E., Zhang, H., et al. (2009). Characterizing the swimming properties of artificial bacterial flagella. Nano Letters, 9(10), 3663-3667.

[89] Pak, O. S., Gao, W., Wang, J., & Lauga, E. (2011). High-speed propulsion of flexible nanowire motors: Theory and experiments. Soft Matter, 7(18), 8169-8181.

[90] Dong, Z., Schumann, M. F., Hokkanen, M. J., Chang, B., Welle, A., Zhou, Q., et al. (2018). Superoleophobic slippery Lubricant‐Infused surfaces: Combining two extremes in the same surface. Advanced Materials, 30(45), 1803890.

[91] Wu, Y., Feng, J., Gao, H., Feng, X., & Jiang, L. (2019). Superwettability‐Based interfacial chemical reactions. Advanced Materials, 31(8), 1800718.

[92] Howell, C., Grinthal, A., Sunny, S., Aizenberg, M., & Aizenberg, J. (2018). Designing liquid‐infused surfaces for medical applications: A review. Advanced Materials, 30(50), 1802724.

[93] Chaim, R. (2012). Grain coalescence by grain rotation in nano-ceramics. Scripta Materialia, 66(5), 269-271.

[94] Majumder, S., Jain, M., Martinez, A., Katiyar, R., Van Keuls, F., & Miranda, F. (2001). Sol–gel derived grain oriented barium strontium titanate thin films for phase shifter applications. Journal of Applied Physics, 90(2), 896-903.

[95] Dimos, D., & Mueller, C. (1998). Perovskite thin films for high-frequency capacitor applications. Annual Review of Materials Science, 28(1), 397-419.

[96] Garnett, E. C., Cai, W., Cha, J. J., Mahmood, F., Connor, S. T., Christoforo, M. G., et al. (2012). Self-limited plasmonic welding of silver nanowire junctions. Nature Materials, 11(3), 241-249.

[97] Kim, S. J., & Jang, D. (2005). Laser-induced nanowelding of gold nanoparticles. Applied Physics Letters, 86(3), 033112.

[98] Son, M., Jeong, S., & Jang, D. (2014). Laser-induced nanowelding of linearly assembled and silica-coated gold nanorods to fabricate au@ SiO2 core–shell nanowires. The Journal of Physical Chemistry C, 118(11), 5961-5967.

[99] Kwag, H. R., Cho, J., Park, S., Park, J., & Gracias, D. H. (2016). Self-folding nanostructures with imprint patterned surfaces (SNIPS). Faraday Discussions, 191, 61-71.

[100] Gracias, D. (2013). Three dimensional self-assembly at the nanoscale. Paper presented at the Independent Component Analyses, Compressive Sampling, Wavelets, Neural Net, Biosystems, and Nanoengineering XI, , 8750. pp. 87500O.

[101] Martz, J. C., Hess, D. W., & Petersen, E. E. (1992). A generalized model of heat effects in surface reactions. I. model development. Journal of Applied Physics, 72(8), 3282-3288.

[102] Carter, G., Nobes, M., & Katardjiev, I. (1988). Fundamental irradiation processes relevant to plasma-surface technology. Vacuum, 38(6), 479-486.

[103] Contolini, R., & d'Asaro, L. (1986). High rate masked etching of GaAs by magnetron ion etching. Journal of Vacuum Science & Technology B: Microelectronics Processing and Phenomena, 4(3), 706-713.

[104] Krogh, O., Wicker, T., & Chapman, B. (1986). The role of gas phase reactions, electron impact, and collisional energy transfer processes relevant to plasma etching of polysilicon with H2 and Cl2. Journal of Vacuum Science & Technology B: Microelectronics Processing and Phenomena, 4(6), 1292-1300.

[105] Martz, J., Hess, D., & Anderson, W. (1990). Tantalum etching in fluorocarbon/oxygen rf glow discharges. Journal of Applied Physics, 67(8), 3609-3617.

[106] Durandet, A., Joubert, O., Pelletier, J., & Pichot, M. (1990). Effects of ion bombardment and chemical reaction on wafer temperature during plasma etching. Journal of Applied Physics, 67(8), 3862-3866.

[107] Joubert, O., Paniez, P., Pelletier, J., & Pons, M. (1991). Etching of polymers by oxygen plasmas: Influence of viscoelastic properties. Applied Physics Letters, 58(9), 959-961.

[108] Martz, J. C., Hess, D. W., & Petersen, E. E. (1992). A generalized model of heat effects in surface reactions. II. application to plasma etching reactions. Journal of Applied Physics, 72(8), 3289-3293.

[109] Magunov, A. (2000). Determining the heat of a surface plasmochemical reaction by scanning calorimetry. Instruments and Experimental Techniques, 43(5), 706-712.

[110] Legtenberg, R., Jansen, H., De Boer, M., & Elwenspoek, M. (1995). Anisotropic reactive ion etching of silicon using SF 6/O 2/CHF 3 gas mixtures. Journal of the Electrochemical Society, 142(6), 2020.

[111] Dai, C., & Cho, J. (2016). In situ monitored self-assembly of three-dimensional polyhedral nanostructures. Nano Letters, 16(6), 3655-3660.

[112] Park, Y. M., Ko, D., Yi, K., Petrov, I., & Kim, Y. (2007). Measurement and estimation of temperature rise in TEM sample during ion milling. Ultramicroscopy, 107(8), 663-668.

[113] Shukla, N., Tripathi, S. K., Banerjee, A., Ramana, A. S. V., Rajput, N. S., & Kulkarni, V. N. (2009). Study of temperature rise during focused ga ion beam irradiation using nanothermo-probe. Applied Surface Science, 256(2), 475-479.

[114] Flamm, D. L., Donnelly, V. M., & Mucha, J. A. (1981). The reaction of fluorine atoms with silicon. Journal of Applied Physics, 52(5), 3633-3639.

[115] Mauer, J., Logan, J., Zielinski, L., & Schwartz, G. (1978). Mechanism of silicon etching by a CF4 plasma. Journal of Vacuum Science and Technology, 15(5), 1734-1738.

[116] Tzeng, Y., & Lin, T. (1987). Dry etching of silicon materials in SF 6 based plasmas roles of and gas additives. Journal of the Electrochemical Society, 134(9), 2304-2309.

[117] Tzeng, Y., & Lin, T. H. (1986). Plasma etching with tetrafluoromethane and nitrous oxide: The role of oxygen in the etching of silicon materials. Journal of the Electrochemical Society, 133(7), 1443-1448.

[118] Mogab, C., Adams, A., & Flamm, D. (1978). Plasma etching of si and SiO2—the effect of oxygen additions to CF4 plasmas. Journal of Applied Physics, 49(7), 3796-3803.

[119] Wakida, T., & Tokino, S. (1996). Surface modification of fibre and polymeric materials by discharge treatment and its application to textile processing.

[120] Cho, J., & Gracias, D. H. (2009). Self-assembly of lithographically patterned nanoparticles. Nano Letters, 9(12), 4049-4052.

[121] Cho, J., Hu, S., & Gracias, D. (2008). Self-assembly of orthogonal three-axis sensors. Applied Physics Letters, 93(4), 043505.

[122] Xu, S., Yan, Z., Jang, K. I., Huang, W., Fu, H., Kim, J., et al. (2015). Materials science. assembly of micro/nanomaterials into complex, three-dimensional architectures by compressive buckling. Science (New York, N.Y.), 347(6218), 154-159. doi:10.1126/science.1260960 [doi]

[123] Chalapat, K., Chekurov, N., Jiang, H., Li, J., Parviz, B., & Paraoanu, G. (2013). Self‐Organized origami structures via Ion‐Induced plastic strain. Advanced Materials, 25(1), 91-95.

[124] Chalapat, K., Chekurov, N., Li, J., & Paraoanu, G. (2012). Ion-beam assisted self-assembly of metallic nanostructures. Nuclear Instruments and Methods in Physics Research Section B: Beam Interactions with Materials and Atoms, 272, 202-205.

[125] Eigenfeld, N. T., Gray, J. M., Brown, J. J., Skidmore, G. D., George, S. M., & Bright, V. M. (2014). Ultra‐thin 3D Nano‐Devices from atomic layer deposition on polyimide. Advanced Materials, 26(23), 3962-3967.

[126] Giannuzzi, L. A., & Stevie, F. A. (1999). A review of focused ion beam milling techniques for TEM specimen preparation. Micron, 30(3), 197-204.

[127] Gour, N., & Verma, S. (2009). Bending of peptide nanotubes by focused electron and ion beams. Soft Matter, 5(9), 1789-1791.

[128] Tripathi, S. K., Shukla, N., Dhamodaran, S., & Kulkarni, V. N. (2008). Controlled manipulation of carbon nanopillars and cantilevers by focused ion beam. Nanotechnology, 19(20), 205302.

[129] Borschel, C., Niepelt, R., Geburt, S., Gutsche, C., Regolin, I., Prost, W., et al. (2009). Alignment of semiconductor nanowires using ion beams. Small, 5(22), 2576-2580.

[130] Rajput, N. S., Banerjee, A., & Verma, H. (2011). Electron-and ion-beam-induced maneuvering of nanostructures: Phenomenon and applications. Nanotechnology, 22(48), 485302.

[131] Yoshida, T., Nagao, M., & Kanemaru, S. (2010). Characteristics of ion-induced bending phenomenon. Japanese Journal of Applied Physics, 49(5R), 056501.

[132] Joung, D., Agarwal, K., Park, H., Liu, C., Oh, S., & Cho, J. (2016). Self‐Assembled multifunctional 3D microdevices. Advanced Electronic Materials, 2(6), 1500459.

[133] Huang, X., & Brittain, W. J. (2001). Synthesis and characterization of PMMA nanocomposites by suspension and emulsion polymerization. Macromolecules, 34(10), 3255-3260.

[134] Chao, C., & Guo, L. J. (2004). Reduction of surface scattering loss in polymer microrings using thermal-reflow technique. IEEE Photonics Technology Letters, 16(6), 1498-1500.

[135] Chae, J. J., Lee, S. H., & Suh, K. Y. (2011). Fabrication of multiscale gradient polymer patterns by direct molding and spatially controlled reflow. Advanced Functional Materials, 21(6), 1147-1153.

[136] Yang, H., Chao, C., Lin, C., & Shen, S. (2003). Micro-ball lens array modeling and fabrication using thermal reflow in two polymer layers. Journal of Micromechanics and Microengineering, 14(2), 277..

[137] Yang, H., Chao, C., Wei, M., & Lin, C. (2004). High fill-factor microlens array mold insert fabrication using a thermal reflow process. Journal of Micromechanics and Microengineering, 14(8), 1197.

[138] Popovic, Z. D., Sprague, R. A., & Connell, G. N. (1988). Technique for monolithic fabrication of microlens arrays. Applied Optics, 27(7), 1281-1284.

[139] Rocha, R., Carmo, J., Gomes, J., Belsley, M., & Correia, J. (2012). Microlenses array made with AZ4562 photoresist for stereoscopic acquisition. Procedia Engineering, 47, 619-622.

[140] Schift, H., Spreu, C., Schleunitz, A., & Lee, J. (2011). Shape control of polymer reflow structures fabricated by nanoimprint lithography. Microelectronic Engineering, 88(1), 87-92.

[141] Liu, C., Schauff, J., Joung, D., & Cho, J. (2017). Remotely controlled microscale 3D Self‐Assembly using microwave energy. Advanced Materials Technologies, 2(8), 1700035.

[142] Agarwal, K., Liu, C., Joung, D., Park, H., Oh, S., & Cho, J. (2017). Three-dimensional anisotropic metamaterials as triaxial optical inclinometers. Scientific Reports, 7(1), 1-12.

[143] Xia, Z. C., & Hutchinson, J. W. (2000). Crack patterns in thin films. Journal of the Mechanics and Physics of Solids, 48(6-7), 1107-1131.

[144] Daniel, R. M., Dines, M., & Petach, H. H. (1996). The denaturation and degradation of stable enzymes at high temperatures. Biochemical Journal, 317(1), 1-11.

[145] Dai, C., Agarwal, K., & Cho, J. (2018). Ion-induced localized nanoscale polymer reflow for three-dimensional self-assembly. ACS Nano, 12(10), 10251-10261.

[146] Kochumalayil, J., Meiser, A., Soldera, F., & Possart, W. (2009). Focused ion beam irradiation—morphological and chemical evolution in PMMA. Surface and Interface Analysis: An International Journal Devoted to the Development and Application of Techniques for the Analysis of Surfaces, Interfaces and Thin Films, 41(5), 412-420.

[147] Calcagno, L., Compagnini, G., & Foti, G. (1992). Structural modification of polymer films by ion irradiation. Nuclear Instruments and Methods in Physics Research Section B: Beam Interactions with Materials and Atoms, 65(1-4), IN7-422.

[148] Novoselov, K. S., Fal, V., Colombo, L., Gellert, P., Schwab, M., & Kim, K. (2012). A roadmap for graphene. Nature, 490(7419), 192-200.

[149] Geim, A. K., & Novoselov, K. S. (2010). The rise of graphene. Nanoscience and technology: A collection of reviews from nature journals (pp. 11-19) World Scientific.

[150] Geim, A. K. (2009). Graphene: Status and prospects. Science (New York, N.Y.), 324(5934), 1530-1534. doi:10.1126/science.1158877

[151] Novoselov, K. S., Jiang, D., Schedin, F., Booth, T. J., Khotkevich, V. V., Morozov, S. V., et al. (2005). Two-dimensional atomic crystals. Proceedings of the National Academy of Sciences of the United States of America, 102(30), 10451-10453. doi:0502848102

[152] Soto Lamata, I., Alonso-González, P., Hillenbrand, R., & Nikitin, A. Y. (2015). Plasmons in cylindrical 2D materials as a platform for nanophotonic circuits. ACS Photonics, 2(2), 280-286.

[153] Chang, C., & Ortix, C. (2017). Theoretical prediction of a giant anisotropic magnetoresistance in carbon nanoscrolls. Nano Letters, 17(5), 3076-3080.

[154] Lanza, M., Bayerl, A., Gao, T., Porti, M., Nafria, M., Jing, G., et al. (2013). Graphene ‐ Coated atomic force microscope tips for reliable nanoscale electrical characterization. Advanced Materials, 25(10), 1440-1444.

[155] Winters, S., Hallam, T., Nolan, H., & Duesberg, G. S. (2012). Production of 3D ‐ shaped graphene via transfer printing. Physica Status Solidi (b), 249(12), 2515-2518.

[156]. Reserbat-Plantey, A., Kalita, D., Han, Z., Ferlazzo, L., Autier-Laurent, S., Komatsu, K., et al. (2014). Strain superlattices and macroscale suspension of graphene induced by corrugated substrates. Nano Letters, 14(9), 5044-5051.

[157] Shim, W., Brown, K. A., Zhou, X., Rasin, B., Liao, X., & Mirkin, C. A. (2012). Multifunctional cantilever-free scanning probe arrays coated with multilayer graphene. Proceedings of the National Academy of Sciences of the United States of America, 109(45), 18312-18317. doi:10.1073/pnas.1216183109 [doi]

[158] Choi, J., Kim, H. J., Wang, M. C., Leem, J., King, W. P., & Nam, S. (2015). Three-dimensional integration of graphene via swelling, shrinking, and adaptation. Nano Letters, 15(7), 4525-4531.

[159] Deng, T., Yoon, C., Jin, Q., Li, M., Liu, Z., & Gracias, D. H. (2015). Self-folding graphene-polymer bilayers. Applied Physics Letters, 106(20), 203108.

[160] Childres, I., Jauregui, L. A., Tian, J., & Chen, Y. P. (2011). Effect of oxygen plasma etching on graphene studied using raman spectroscopy and electronic transport measurements. New Journal of Physics, 13(2), 025008.

[161] . Childres, I., Jauregui, L. A., Foxe, M., Tian, J., Jalilian, R., Jovanovic, I., et al. (2010). Effect of electron-beam irradiation on graphene field effect devices. Applied Physics Letters, 97(17), 173109.

[162] Childres, I., Jauregui, L. A., Park, W., Cao, H., & Chen, Y. P. (2013). Raman spectroscopy of graphene and related materials. New Developments in Photon and Materials Research, 1, 1-20.

[163] Koppens, F. H., Chang, D. E., & Garcia de Abajo, F Javier. (2011). Graphene plasmonics: A platform for strong light–matter interactions. Nano Letters, 11(8), 3370-3377.

[164] Luo, X., Qiu, T., Lu, W., & Ni, Z. (2013). Plasmons in graphene: Recent progress and applications. Materials Science and Engineering: R: Reports, 74(11), 351-376.

[165] Rodrigo, D., Limaj, O., Janner, D., Etezadi, D., Garcia de Abajo, F. J., Pruneri, V., et al. (2015). APPLIED PHYSICS. mid-infrared plasmonic biosensing with graphene. Science (New York, N.Y.), 349(6244), 165-168. doi:10.1126/science.aab2051

[166] Li, Y., Yan, H., Farmer, D. B., Meng, X., Zhu, W., Osgood, R. M., et al. (2014). Graphene plasmon enhanced vibrational sensing of surface-adsorbed layers. Nano Letters, 14(3), 1573-1577.

[167] Farmer, D. B., Avouris, P., Li, Y., Heinz, T. F., & Han, S. (2016). Ultrasensitive plasmonic detection of molecules with graphene. Acs Photonics, 3(4), 553-557.

[168] Sheehan, P. E., & Whitman, L. J. (2005). Detection limits for nanoscale biosensors. Nano Letters, 5(4), 803-807.

[169] Blees, M. K., Barnard, A. W., Rose, P. A., Roberts, S. P., McGill, K. L., Huang, P. Y., et al. (2015). Graphene kirigami. Nature, 524(7564), 204-207.

[170] Gladman, A. S., Matsumoto, E. A., Nuzzo, R. G., Mahadevan, L., & Lewis, J. A. (2016). Biomimetic 4D printing. Nature Materials, 15(4), 413-418.

[171] Tang, Y., Lin, G., Yang, S., Yi, Y. K., Kamien, R. D., & Yin, J. (2017). Programmable Kiri-Kirigami metamaterials. Advanced Materials, 29(10), 1604262.

[172] Shyu, T. C., Damasceno, P. F., Dodd, P. M., Lamoureux, A., Xu, L., Shlian, M., et al. (2015). A kirigami approach to engineering elasticity in nanocomposites through patterned defects. Nature Materials, 14(8), 785-789.

[173] Tian, Z., Xu, B., Hsu, B., Stan, L., Yang, Z., & Mei, Y. (2018). Reconfigurable vanadium dioxide nanomembranes and microtubes with controllable phase transition temperatures. Nano Letters, 18(5), 3017-3023.

[174] Wang, X., Dong, K., Choe, H. S., Liu, H., Lou, S., Tom, K. B., et al. (2018). Multifunctional microelectro-opto-mechanical platform based on phase-transition materials. Nano Letters, 18(3), 1637-1643.

[175] Xu, B., Tian, Z., Wang, J., Han, H., Lee, T., & Mei, Y. (2018). Stimuli-responsive and on-chip nanomembrane micro-rolls for enhanced macroscopic visual hydrogen detection. Science Advances, 4(4), eaap8203.

[176] Xu, W., Qin, Z., Chen, C., Kwag, H. R., Ma, Q., Sarkar, A., et al. (2017). Ultrathin thermoresponsive self-folding 3D graphene. Science Advances, 3(10), e1701084.

[177] Agarwal, K., Liu, C., Joung, D., Park, H., Jeong, J., Kim, D., et al. (2017). Three-dimensionally coupled THz octagrams as isotropic metamaterials. ACS Photonics, 4(10), 2436-2445.

[178] Joung, D., Gu, T., & Cho, J. (2016). Tunable optical transparency in self-assembled three-dimensional polyhedral graphene oxide. ACS Nano, 10(10), 9586-9594.

[179] Grimm, D., Bof Bufon, C. C., Deneke, C., Atkinson, P., Thurmer, D. J., Schäffel, F., et al. (2013). Rolled-up nanomembranes as compact 3D architectures for field effect transistors and fluidic sensing applications. Nano Letters, 13(1), 213-218.

[180] Karnaushenko, D., Karnaushenko, D. D., Makarov, D., Baunack, S., Schäfer, R., & Schmidt, O. G. (2015). Self‐Assembled On‐Chip‐Integrated giant Magneto‐Impedance sensorics. Advanced Materials, 27(42), 6582-6589.

[181] Huang, W., Zhou, J., Froeter, P. J., Walsh, K., Liu, S., Kraman, M. D., et al. (2018). Three-dimensional radio-frequency transformers based on a self-rolled-up membrane platform. Nature Electronics, 1(5), 305-313.

[182] Torikai, K., Furlan de Oliveira, R., Starnini de Camargo, Davi H, & Bof Bufon, C. C. (2018). Low-voltage, flexible, and self-encapsulated ultracompact organic thin-film transistors based on nanomembranes. Nano Letters, 18(9), 5552-5561.

[183] Magdanz, V., Medina‐Sánchez, M., Schwarz, L., Xu, H., Elgeti, J., & Schmidt, O. G. (2017). Spermatozoa as functional components of robotic microswimmers. Advanced Materials, 29(24), 1606301.

[184] Magdanz, V., Guix, M., Hebenstreit, F., & Schmidt, O. G. (2016). Dynamic polymeric microtubes for the remote‐controlled capture, guidance, and release of sperm cells. Advanced Materials, 28(21), 4084-4089.

[185] Malachowski, K., Breger, J., Kwag, H. R., Wang, M. O., Fisher, J. P., Selaru, F. M., et al. (2014). Stimuli‐responsive theragrippers for chemomechanical controlled release. Angewandte Chemie International Edition, 53(31), 8045-8049.

[186] Wu, C., Li, F., Pao, C., & Srolovitz, D. J. (2017). Folding sheets with ion beams. Nano Letters, 17(1), 249-254.

[187] Tian, Z., Huang, W., Xu, B., Li, X., & Mei, Y. (2018). Anisotropic rolling and controlled chirality of nanocrystalline diamond nanomembranes toward biomimetic helical frameworks. Nano Letters, 18(6), 3688-3694.

[188] Abdullah, A. M., Li, X., Braun, P. V., Rogers, J. A., & Hsia, K. J. (2018). Self‐Folded Gripper‐Like architectures from Stimuli‐Responsive bilayers. Advanced Materials, 30(31), 1801669.

[189] Mao, Y., Yu, K., Isakov, M. S., Wu, J., Dunn, M. L., & Qi, H. J. (2015). Sequential self-folding structures by 3D printed digital shape memory polymers. Scientific Reports, 5, 13616.

[190] Liu, Y., Shaw, B., Dickey, M. D., & Genzer, J. (2017). Sequential self-folding of polymer sheets. Science Advances, 3(3), e1602417.

[191] Hawkes, E., An, B., Benbernou, N. M., Tanaka, H., Kim, S., Demaine, E. D., et al. (2010). Programmable matter by folding. Proceedings of the National Academy of Sciences of the United States of America, 107(28), 12441-12445. doi:10.1073/pnas.0914069107

[192] Laflin, K. E., Morris, C. J., Muqeem, T., & Gracias, D. H. (2012). Laser triggered sequential folding of microstructures. Applied Physics Letters, 101(13), 131901.

[193] Si, K. J., Sikdar, D., Chen, Y., Eftekhari, F., Xu, Z., Tang, Y., et al. (2014). Giant plasmene nanosheets, nanoribbons, and origami. ACS Nano, 8(11), 11086-11093.

[194] Murray, J., Song, K., Huebner, W., & O'Keefe, M. (2012). Electron beam induced crystallization of sputter deposited amorphous alumina thin films. Materials Letters, 74, 12-15.

[195] Nakamura, R., Ishimaru, M., Yasuda, H., & Nakajima, H. (2013). Atomic rearrangements in amorphous Al2O3 under electron-beam irradiation. Journal of Applied Physics, 113(6), 064312.

[196] Stevens Kalceff, M., Thorogood, G., & Short, K. (1999). Charge trapping and defect segregation in quartz. Journal of Applied Physics, 86(1), 205-208.

[197] Timoshenko, S. (1925). Analysis of bi-metal thermostats. Josa, 11(3), 233-255.

[198] Liu, J., Xu, J., Ni, Y., Fan, F., Zhang, C., & Yu, S. (2012). A family of carbon-based nanocomposite tubular structures created by in situ electron beam irradiation. ACS Nano, 6(5), 4500-4507.

[199] Jiang, Z., He, J., Deshmukh, S. A., Kanjanaboos, P., Kamath, G., Wang, Y., et al. (2015). Subnanometre ligand-shell asymmetry leads to janus-like nanoparticle membranes. Nature Materials, 14(9), 912-917.

[200] Seminara, A., Pokroy, B., Kang, S. H., Brenner, M. P., & Aizenberg, J. (2011). Mechanism of nanostructure movement under an electron beam and its application in patterning. Physical Review B, 83(23), 235438.

[201] Rajput, N. S., Le Marrec, F., El Marssi, M., & Jouiad, M. (2018). Fabrication and manipulation of nanopillars using electron induced excitation. Journal of Applied Physics, 124(7), 074301.

[202] Hines, L., Petersen, K., Lum, G. Z., & Sitti, M. (2017). Soft actuators for small ‐ scale robotics. Advanced Materials, 29(13), 1603483.

[203] Yasuda, M., Furukawa, Y., Kawata, H., & Hirai, Y. (2015). Multiscale simulation of resist pattern shrinkage during scanning electron microscope observations. Journal of

Vacuum Science & Technology B, Nanotechnology and Microelectronics: Materials, Processing, Measurement, and Phenomena, 33(6), 06FH02.

[204] Azuma, T., Chiba, K., Abe, H., Motoki, H., & Sasaki, N. (2004). Mechanism of ArF resist-pattern shrinkage in critical-dimension scanning electron microscopy measurement. Journal of Vacuum Science & Technology B: Microelectronics and Nanometer Structures Processing, Measurement, and Phenomena, 22(1), 226-230.

[205] Jung, K., Hahn, J., In, S., Bae, Y., Lee, H., Pikhitsa, P. V., et al. (2014). Hotspot‐engineered 3D multipetal flower assemblies for surface‐enhanced raman spectroscopy. Advanced Materials, 26(34), 5924-5929.

[206] De Angelis, F., Malerba, M., Patrini, M., Miele, E., Das, G., Toma, A., et al. (2013). 3D hollow nanostructures as building blocks for multifunctional plasmonics. Nano Letters, 13(8), 3553-3558.

[207] Lin, E., Fang, J., Park, S., Johnson, F. W., & Jacobs, H. O. (2013). Effective localized collection and identification of airborne species through electrodynamic precipitation and SERS-based detection. Nature Communications, 4(1), 1-8.

[208] Dipalo, M., Messina, G. C., Amin, H., La Rocca, R., Shalabaeva, V., Simi, A., et al. (2015). 3D plasmonic nanoantennas integrated with MEA biosensors. Nanoscale, 7(8), 3703-3711.

[209] Huck, C., Neubrech, F., Vogt, J., Toma, A., Gerbert, D., Katzmann, J., et al. (2014). Surface-enhanced infrared spectroscopy using nanometer-sized gaps. Acs Nano, 8(5), 4908-4914.

[210] Miyazaki, C. M., Shimizu, F. M., & Ferreira, M. (2017). Surface plasmon resonance (SPR) for sensors and biosensors. Nanocharacterization techniques (pp. 183-200) Elsevier.

[211] Chen, X., Ciracì, C., Smith, D. R., & Oh, S. (2015). Nanogap-enhanced infrared spectroscopy with template-stripped wafer-scale arrays of buried plasmonic cavities. Nano Letters, 15(1), 107-113.

[212] Malerba, M., Alabastri, A., Miele, E., Zilio, P., Patrini, M., Bajoni, D., et al. (2015). 3D vertical nanostructures for enhanced infrared plasmonics. Scientific Reports, 5, 16436.

[213] Jubb, A. M., Jiao, Y., Eres, G., Retterer, S. T., & Gu, B. (2016). Elevated gold ellipse nanoantenna dimers as sensitive and tunable surface enhanced raman spectroscopy substrates. Nanoscale, 8(10), 5641-5648.

[214] Hatab, N. A., Hsueh, C., Gaddis, A. L., Retterer, S. T., Li, J., Eres, G., et al. (2010). Free-standing optical gold bowtie nanoantenna with variable gap size for enhanced raman spectroscopy. Nano Letters, 10(12), 4952-4955.

[215] Lin, S., Hatab, N. A., Gu, B., Chao, B., Li, J., & Hsueh, C. (2016). Free-standing gold elliptical nanoantenna with tunable wavelength in near-infrared region for enhanced raman spectroscopy. Applied Physics A, 122(7), 674.

[216] Lin, E., Fang, J., Park, S., Stauden, T., Pezoldt, J., & Jacobs, H. O. (2013). Effective collection and detection of airborne species using SERS‐Based detection and localized electrodynamic precipitation. Advanced Materials, 25(26), 3554-3559.

[217] Yoo, D., Johnson, T. W., Cherukulappurath, S., Norris, D. J., & Oh, S. (2015). Template-stripped tunable plasmonic devices on stretchable and rollable substrates. Acs Nano, 9(11), 10647-10654.

[218] Hentschel, M., Schäferling, M., Duan, X., Giessen, H., & Liu, N. (2017). Chiral plasmonics. Science Advances, 3(5), e1602735.

[219] Shen, X., Song, C., Wang, J., Shi, D., Wang, Z., Liu, N., et al. (2012). Rolling up gold nanoparticle-dressed DNA origami into three-dimensional plasmonic chiral nanostructures. Journal of the American Chemical Society, 134(1), 146-149.

[220] Homola, J., Yee, S. S., & Gauglitz, G. (1999). Surface plasmon resonance sensors. Sensors and Actuators B: Chemical, 54(1-2), 3-15.

[221] Barnes, W. L., Dereux, A., & Ebbesen, T. W. (2003). Surface plasmon subwavelength optics. Nature, 424(6950), 824-830.

[222] Fang, J., Park, S., Schlag, L., Stauden, T., Pezoldt, J., & Jacobs, H. O. (2014). Localized collection of airborne analytes: A transport driven approach to improve the response time of existing gas sensor designs. Advanced Functional Materials, 24(24), 3706-3714.

[223] Stein, P. E., Leslie, A. G., Finch, J. T., & Carrell, R. W. (1991). Crystal structure of uncleaved ovalbumin at 1· 95 Å resolution. Journal of Molecular Biology, 221(3), 941-959.

[224] Kozlowski, L. P. (2017). Proteome-pI: Proteome isoelectric point database. Nucleic Acids Research, 45(D1), D1112-D1116.

[225] Fraiwan, A., Hasan, M. N., An, R., Xu, J. Z., Rezac, A. J., Kocmich, N. J., et al. (2019). International Multi-Site Clinical Validation of Point-of-Care Microchip Electrophoresis Test for Hemoglobin Variant Identification,

[226] Huang, S., Pandey, R., Barman, I., Kong, J., & Dresselhaus, M. (2018). Raman enhancement of blood constituent proteins using graphene. ACS Photonics, 5(8), 2978-2982.

[227] Erickson, H. P. (2009). Size and shape of protein molecules at the nanometer level determined by sedimentation, gel filtration, and electron microscopy. Biological Procedures Online, 11(1), 32.

[228] Tegenfeldt, J. O., Prinz, C., Cao, H., Huang, R. L., Austin, R. H., Chou, S. Y., et al. (2004). Micro-and nanofluidics for DNA analysis. Analytical and Bioanalytical Chemistry, 378(7), 1678-1692.

[229] Liu, F., & Cubukcu, E. (2013). Tunable omnidirectional strong light-matter interactions mediated by graphene surface plasmons. Physical Review B, 88(11), 115439.

[230] Xu, W., Mao, N., & Zhang, J. (2013). Graphene: A platform for surface‐enhanced raman spectroscopy. Small, 9(8), 1206-1224.

[231] Yang, X., Sun, Z., Low, T., Hu, H., Guo, X., García de Abajo, F Javier, et al. (2018). Nanomaterial‐Based Plasmon‐Enhanced infrared spectroscopy. Advanced Materials, 30(20), 1704896.

[232] Low, T., & Avouris, P. (2014). Graphene plasmonics for terahertz to mid-infrared applications. ACS Nano, 8(2), 1086-1101.

[233] Marini, A., Silveiro, I., & García de Abajo, F Javier. (2015). Molecular sensing with tunable graphene plasmons. Acs Photonics, 2(7), 876-882.

[234] Hu, H., Yang, X., Zhai, F., Hu, D., Liu, R., Liu, K., et al. (2016). Far-field nanoscale infrared spectroscopy of vibrational fingerprints of molecules with graphene plasmons. Nature Communications, 7(1), 1-8.

[235] Ju, L., Geng, B., Horng, J., Girit, C., Martin, M., Hao, Z., et al. (2011). Graphene plasmonics for tunable terahertz metamaterials. Nature Nanotechnology, 6(10), 630.

[236] Fei, Z., Rodin, A., Andreev, G. O., Bao, W., McLeod, A., Wagner, M., et al. (2012). Gate-tuning of graphene plasmons revealed by infrared nano-imaging. Nature, 487(7405), 82-85.

[237] Fang, Z., Wang, Y., Schlather, A. E., Liu, Z., Ajayan, P. M., García de Abajo, F Javier, et al. (2014). Active tunable absorption enhancement with graphene nanodisk arrays. Nano Letters, 14(1), 299-304.

[238] Woessner, A., Lundeberg, M. B., Gao, Y., Principi, A., Alonso-González, P., Carrega, M., et al. (2015). Highly confined low-loss plasmons in graphene–boron nitride heterostructures. Nature Materials, 14(4), 421-425.

[239] Freitag, M., Low, T., & Avouris, P. (2013). Increased responsivity of suspended graphene photodetectors. Nano Letters, 13(4), 1644-1648.

[240] Venkatesan, B. M., Estrada, D., Banerjee, S., Jin, X., Dorgan, V. E., Bae, M., et al. (2012). Stacked graphene-Al2O3 nanopore sensors for sensitive detection of DNA and DNA–protein complexes. ACS Nano, 6(1), 441-450.

[241] Lee, S., Hahm, M. G., Vajtai, R., Hashim, D. P., Thurakitseree, T., Chipara, A. C., et al. (2012). Utilizing 3D SERS active volumes in aligned carbon nanotube scaffold substrates. Advanced Materials, 24(38), 5261-5266.

[242] Wang, P., Liang, O., Zhang, W., Schroeder, T., & Xie, Y. (2013). Ultra‐sensitive graphene‐plasmonic hybrid platform for label‐free detection. Advanced Materials, 25(35), 4918-4924.

[243] Fink, J., Carpi, N., Betz, T., Bétard, A., Chebah, M., Azioune, A., et al. (2011). External forces control mitotic spindle positioning. Nature Cell Biology, 13(7), 771-778.

[244] Xi, W., Schmidt, C. K., Sanchez, S., Gracias, D. H., Carazo-Salas, R. E., Butler, R., et al. (2016). Molecular insights into division of single human cancer cells in on-chip transparent microtubes. ACS Nano, 10(6), 5835-5846.

[245] Medina-Sánchez, M., Ibarlucea, B., Pérez, N., Karnaushenko, D. D., Weiz, S. M., Baraban, L., et al. (2016). High-performance three-dimensional tubular nanomembrane sensor for DNA detection. Nano Letters, 16(7), 4288-4296.

[246] Madani, A., Kleinert, M., Stolarek, D., Zimmermann, L., Ma, L., & Schmidt, O. G. (2015). Vertical optical ring resonators fully integrated with nanophotonic waveguides on silicon-on-insulator substrates. Optics Letters, 40(16), 3826-3829.

[247] Miao, S., Chen, D., Madani, A., Jorgensen, M. R., Bolaños Quiñones, V. A., Ma, L., et al. (2015). Optofluidic sensor: Evaporation kinetics detection of solvents dissolved with Cd3P2 colloidal quantum dots in a Rolled‐Up microtube. Advanced Optical Materials, 3(2), 187-193.

[248] Weiz, S. M., Medina‐Sánchez, M., & Schmidt, O. G. (2018). Microsystems for Single‐Cell analysis. Advanced Biosystems, 2(2), 1700193.

[249] Smith, E. J., Schulze, S., Kiravittaya, S., Mei, Y., Sanchez, S., & Schmidt, O. G. (2011). Lab-in-a-tube: Detection of individual mouse cells for analysis in flexible split-wall microtube resonator sensors. Nano Letters, 11(10), 4037-4042.

[250] Yin, Y., Pang, J., Wang, J., Lu, X., Hao, Q., Saei Ghareh Naz, E., et al. (2019). Graphene-activated optoplasmonic nanomembrane cavities for photodegradation detection. ACS Applied Materials & Interfaces, 11(17), 15891-15897.

[251] Schmidt, O., Deneke, C., Kiravittaya, S., Songmuang, R., Heidemeyer, H., Nakamura, Y., et al. (2002). Self-assembled nanoholes, lateral quantum-dot molecules, and rolled-up nanotubes. IEEE Journal of Selected Topics in Quantum Electronics, 8(5), 1025-1034.

[252] Ryu, S., Maultzsch, J., Han, M. Y., Kim, P., & Brus, L. E. (2011). Raman spectroscopy of lithographically patterned graphene nanoribbons. ACS Nano, 5(5), 4123-4130.

[253] Schmidt, O., Schmarje, N., Deneke, C., Müller, C., & Jin‐Phillipp, N. (2001). Three‐Dimensional Nano‐objects evolving from a Two‐Dimensional layer technology. Advanced Materials, 13(10), 756-759.

[254] Yan, H., Low, T., Zhu, W., Wu, Y., Freitag, M., Li, X., et al. (2013). Damping pathways of mid-infrared plasmons in graphene nanostructures. Nature Photonics, 7(5), 394.

[255] Zhang, B., Bian, Y., Ren, L., Guo, F., Tang, S., Mao, Z., et al. (2017). Hybrid dielectric-loaded nanoridge plasmonic waveguide for low-loss light transmission at the subwavelength scale. Scientific Reports, 7(1), 1-9.

[256] Fang, Y., & Sun, M. (2015). Nanoplasmonic waveguides: Towards applications in integrated nanophotonic circuits. Light: Science & Applications, 4(6), e294-e294.

[257] Berini, P. (2006). Figures of merit for surface plasmon waveguides. Optics Express, 14(26), 13030-13042.

[258] Wang, Z., Cheng, F., Winsor, T., & Liu, Y. (2016). Optical chiral metamaterials: A review of the fundamentals, fabrication methods and applications. Nanotechnology, 27(41), 412001.

[259] Ben-Moshe, A., Maoz, B. M., Govorov, A. O., & Markovich, G. (2013). Chirality and chiroptical effects in inorganic nanocrystal systems with plasmon and exciton resonances. Chemical Society Reviews, 42(16), 7028-7041.

[260] Smith, K. W., Zhao, H., Zhang, H., SÃ¡nchez-Iglesias, A., Grzelczak, M., Wang, Y., et al. (2016). Chiral and achiral nanodumbbell dimers: The effect of geometry on plasmonic properties. ACS Nano, 10(6), 6180-6188.

[261] Kong, X., Zhao, R., Wang, Z., & Govorov, A. O. (2017). Mid-infrared plasmonic circular dichroism generated by graphene nanodisk assemblies. Nano Letters, 17(8), 5099-5105.

[262] Zhang, S., Park, Y., Li, J., Lu, X., Zhang, W., & Zhang, X. (2009). Negative refractive index in chiral metamaterials. Physical Review Letters, 102(2), 023901.